Dry processing of perovskite-polymer composites for photon conversion and detection

– PhD Thesis –

VNIVERSITAT DE VALÈNCIA

Doctorate in Nanoscience and Nanotechnology

Bas A.H. Huisman

Directors:

Prof. Dr. Hendrik Jan Bolink

Dr. Michele Sessolo

November 2023

Prof. Dr. Hendrik Jan Bolink, Profesor Titular de la Universidad de Valencia en el Instituto de Ciencia Molecular (ICMol), y **Dr.Michele Sessolo**, investigador Ramón y Cajal en la Universidad de Valencia certifican que la memoria presentada por el estudiante de doctorado Bas A.H. Huisman, con el título "*Dry processing of perovskite-polymer composites for photon conversion and detection*", corresponde a su Tesis Doctoral y ha sido realizada bajo su dirección, autorizando mediante este escrito la presentación de la misma.

En Valencia, a 16 de Noviembre de 2023.

Prof. Dr. Hendrik Jan Bolink

Dr. Michele Sessolo

Index

Chapter 1

Introduction and aim of the thesis

1.1. The rise of the metal halide perovskites

The term "perovskite" was first used by Gustav Rose in 1839 when discovering the $CaTiO_3$ mineral, who named it after the Russian mineralogist Perovski.[1] In 1926 Goldschmidt used the same term for the same group of crystals in his research about the tolerance factor.[2] From that moment on, the term perovskite was adopted in science to define a particular crystal structure.

Perovskites are crystalline materials with the general chemical formula ABX_3. Due to this very general expression, a large number of compounds can be considered perovskites. Although the most studied perovskites are metal oxides, in this thesis, a specific sub-group is investigated, namely the metal halide perovskites. From now on, the name "perovskite" will be used for this sub-group. Some of the metal halide perovskites are semiconductors, most notably those containing lead and tin as the divalent B cation. While semiconducting perovskites have been known since the 19^{th} century, only in the last 10 years they have become the spotlight of international research due to their successful application as absorbers in photovoltaic devices.[3,4] They exhibit favorable optoelectronic properties, such as high optical absorption coefficient, long electron-hole diffusion lengths, tunable and direct bandgap, and narrow photoluminescence.[5,6] The possibility of adjusting the properties of the perovskite by exchanging the A, B, or X sites makes the range of possible applications extensive.

In **Figure 1.1** the efficiency chart of all research cells (not limited by a minimum area) is depicted as compiled and continuously updated by the National Renewable Energy Laboratory (NREL).[7] From this graph, it can be seen that perovskite solar cells have achieved efficiencies similar to that of silicon solar cells in just a few years of research. Besides solar cells, perovskites can also be employed as the emitter in light-emitting diodes (LEDs). Also in this area of application, efficiencies similar to that of other inorganic LEDs have been achieved.[8] While perovskite solar cells and LEDs are nowadays well-known studied applications for perovskites, the possible implementations of these semiconductors in other technologies are vast, among others in thermoelectrics, color converters, piezoelectricity, photodetectors, transistors, pressure sensors, etc.[9,10]

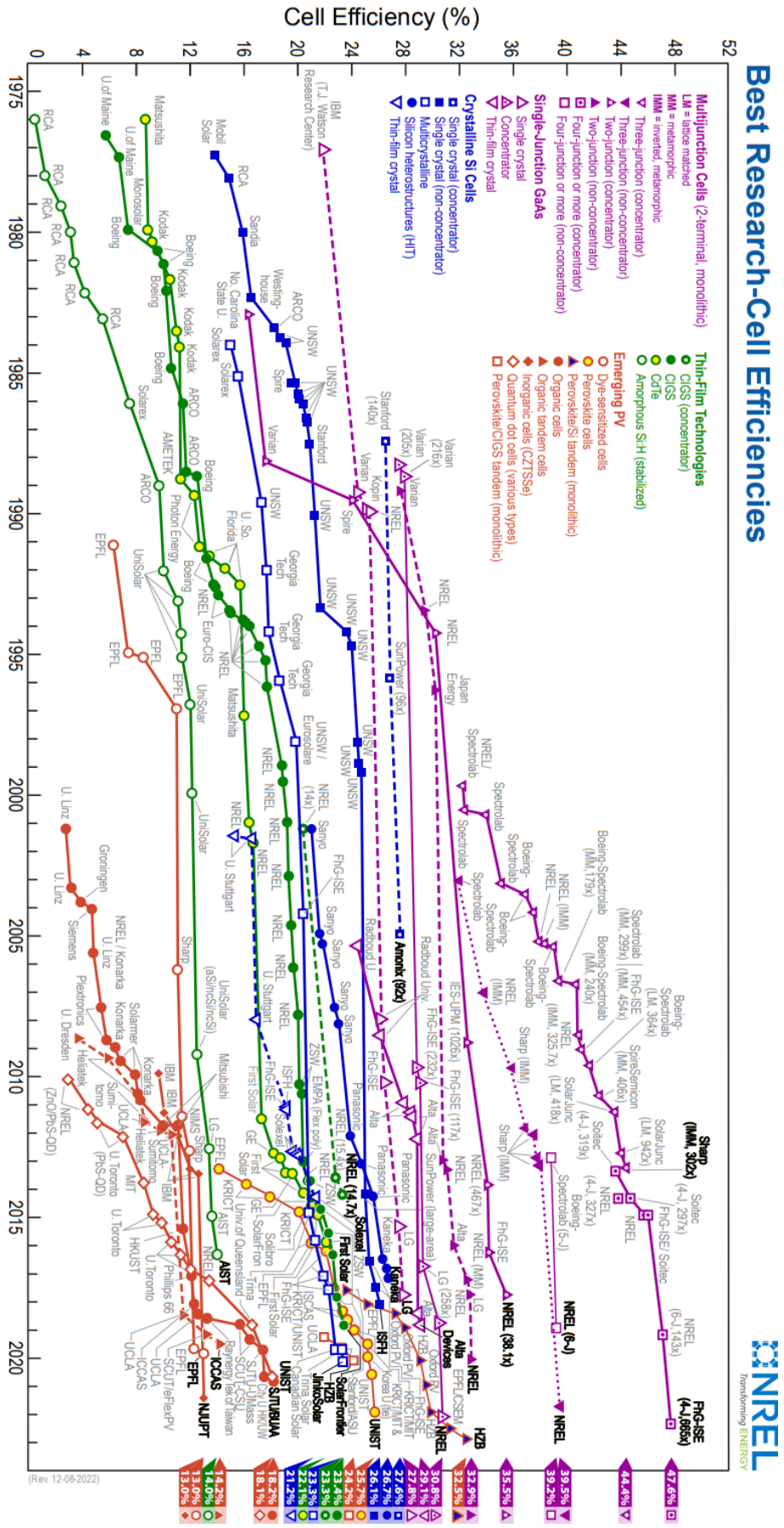

Figure 1.1. Efficiency chart of best-performing research solar cells.[7]

1.2. Properties of halide perovskites

Crystal structure

The standard ABX_3 configuration of ternary perovskites is depicted in **Figure 1.2**, where A is an organic or inorganic monovalent cation, B is usually a divalent metal, and X is a halide anion. This three-dimensional (3D) perovskite structure is mostly held by ionic bounds and consists of corner-sharing $[BX_6]^{4-}$ octahedral, with the A cations occupying the cavities formed by eight adjacent lead halide octahedra.

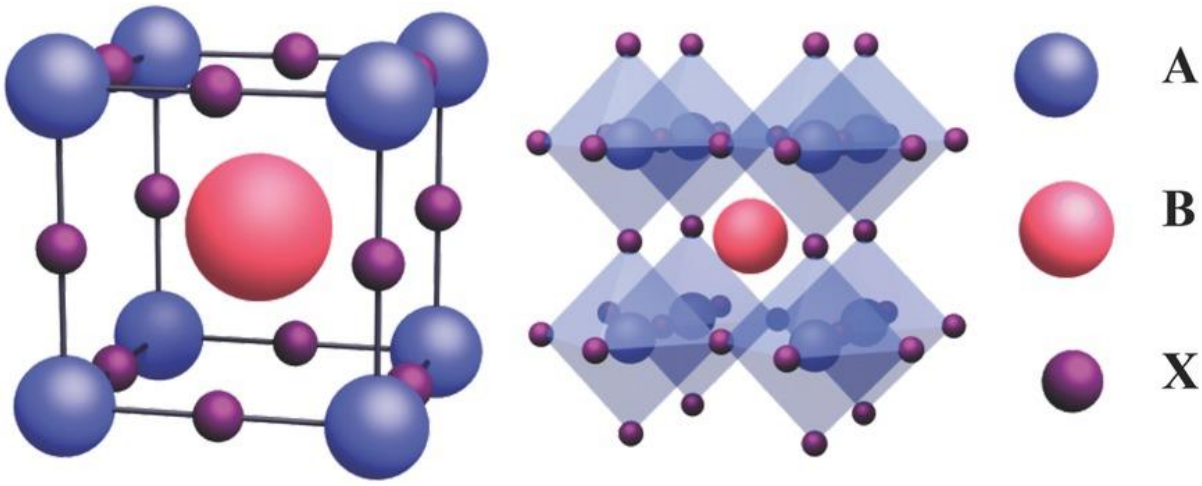

Figure 1.2. ABX_3 halide perovskite structure, where the A site is a monovalent cation, B is a divalent cation, and X is a halide anion.[11]

The perovskite ABX_3 structure can be constructed with a large variation of cations and anions (in this thesis exclusively composed of halide anions). The monovalent A cation can be a small organic cation, like methylammonium (MA^+), formamidinium (FA^+), or a large monovalent alkali cation such as cesium (Cs^+). The B-site is usually a divalent cation with stable octahedral coordination like lead (Pb^{2+}), tin (Sn^{2+}), and germanium (Ge^{2+}). The X-site is occupied by a halide anion such as iodine (I^-), bromine (Br^-), or chlorine (Cl^-). By changing or substituting different cations or anions the perovskite properties change accordingly.[12,13]

While the perovskite structure is susceptible to different compositions, the A cation must fit in the cavity delimited by the inorganic octahedral. To predict a stable structure two semi-empirical geometric parameters, known as the Goldschmidt tolerance factor (t), and the octahedral factor (μ), can be used.[2,14] Both geometrical indicators use the ionic radii, A (r_A),

B (r_B), and X (r_X) of the ions included in the perovskite structure to forecast its stability. The Goldschmidt tolerance factor takes into account all three ionic radii, as described in **equation 1.1.**

$$t = \frac{r_A + r_X}{\sqrt{2}(r_B + r_X)} \qquad \text{Equation 1.1.}$$

Empirically, a stable 3D perovskite structure is formed when the tolerance factor is between $0.81 \leq t \leq 1.0$. For the octahedral factor, the B and X-site ionic radii are used (**equation 1.2.**), where a value of the octahedral factor between $0.44 \leq \mu \leq 0.90$ is desired to obtain a stable structure.

$$\mu = \frac{r_B}{r_X} \qquad \text{Equation 1.2.}$$

It is possible to have a perovskite configuration with multiple different cations or anions, as long as the above considerations are met.

Optoelectronic properties

In **Figure 1.3a** the composition of the conduction and valence bands of (lead-based) perovskites is schematically displayed. The conduction band of lead-based perovskites is formed from the antibonding orbitals of the hybridization of the Pb p-orbital and the halide s-orbital. Owing to the high density of states of the Pb p-orbitals, the lower levels of the conduction band are mainly composed of degenerate lead p-bands. The valence band maximum, however, is formed by the antibonding stated by the hybridization of the halide p-orbitals and metal s-orbitals. Therefore, the halogen p-character in the valence band maximum can be increased by changing the halide ion from Cl^- to Br^- and from Br^- to I^-, resulting in a decrease of bandgap by changing the halide ion from Cl^- to I^-.[15] Intermediate bandgaps as compared to the pure halide materials can also be prepared by mixed halide perovskites (**Figure 1.3b**). Another factor that can modify the perovskite´s bandgap is the change in the octahedral tilt. This can occur when the Pb-X-Pb dihedral angle changes upon replacement of a different size A-site cation or when the crystal structure changes phases. For example, a decrease in an octahedral tilt, by replacing a large A cation with a smaller one or changing the crystal structure from cubic to tetragonal, weakens the spin-orbit coupling by lowering the orbital overlap between Pb and X, which in turn increases the bandgap.[16] Hence, the two above-described processes make it possible to adapt the bandgap of perovskites by simple substitution of the A-site or X-site.

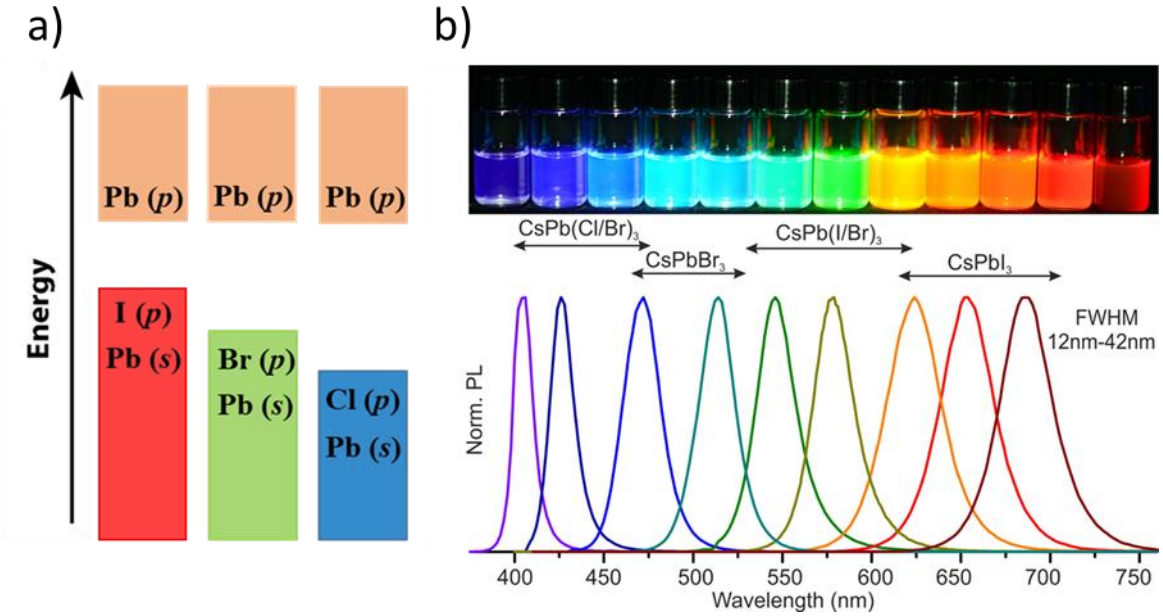

Figure 1.3. (a) Band energy of the conduction and valence band in perovskites, where the conduction band is mainly composed of degenerate lead p-bands and the valence band is formed by the antibonding stated by the hybridization of the halide p-orbitals and metal s-orbitals. (b) Colloidal solutions of $CsPbX_3$ (X= Cl, Br, I) nanocrystals in toluene under UV lamp and representative PL spectra.[17]

One of the interesting features of perovskites is their intense optical absorption. The optical absorption of a semiconductor is fundamentally determined by two factors: the transition matrix elements between valence band states and conduction band states, which measure the probability of each electronic transition, and the joint density of states, which measures the total number of possible transitions.[18] For perovskites, the valence band maximum and conduction band minimum lie at the same point in reciprocal space (*k*-space), and therefore perovskites exhibit a direct bandgap (**Figure 1.4a**). Additionally, as discussed earlier, the lower levels of the conduction band for (lead-based) perovskites are mainly composed of degenerate lead p-bands, and therefore the density of states at the lower conduction band is high. A high density of states is also observed at the top of the valence band which originates, for example for $MAPbI_3$, from mixed lead s-orbitals and iodide p-orbitals (**Figure 1.4b)**. All considered the transition probability between the valence band and conduction band is very high, and therefore the optical absorption for perovskites is intense.

Another interesting property of the band diagram of perovskites is that the electronic band structure exhibits energy surfaces that only deviate modestly. The band extrema can often be approximated using a parabolic relationship between energy (*E*) and momentum (*k*):

$$E = \frac{k^2\hbar}{2m^*}$$ Equation 1.3.

where $\hbar$ is the reduced Planck constant and m* is the effective mass of electrons (holes) in the conduction band (valence band). Therefore, the modest deviations in the electronic band structure of perovskite result in small effective masses of the charge carriers which explain the high mobility and long diffusion lengths in perovskites.[19]

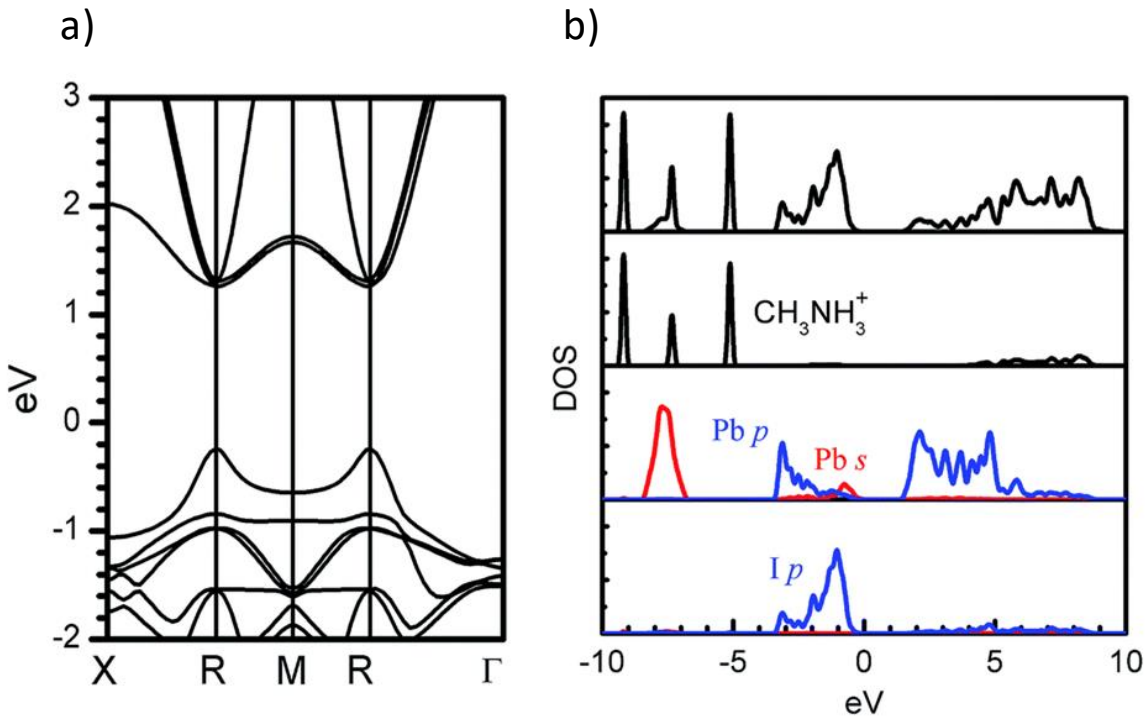

Figure 1.4. (a) Theoretical band structure of cubic $MAPbI_3$. (b) Calculated density of states for the cubic $MAPbI_3$ structure (top) and the density of states of the components constructing the $MAPbI_3$ structure.[18]

High defect tolerance

Defect tolerance is the tendency of a semiconductor to keep its properties despite the presence of crystallographic defects. Most semiconductors have an antibonding and bonding character for the conduction band and valance band, respectively. This feature can bring deep defect

states (states in the middle of the bandgap) when an atom is removed.[20] Perovskites, however, exhibit antibonding character both for the valence band and conduction band. The antibonding character of the valence band raises the band edge and therefore most defect states are within or close to the valence band creating shallow defect states. Moreover, the conduction band exhibits an ionic character, due to the weak coupling of the lead p-orbital with the iodide p-orbital, resulting in energy states which are not easily affected by external defect levels. Therefore, deep defect states within the bandgap are less frequent in perovskites and the properties of the perovskite are mostly preserved irrespective of the defect density.[21]

1.3. Mechanochemical synthesis of perovskite powders

For established photovoltaic (PV) materials, like silicon, cadmium telluride, and copper indium gallium (di)selenide, high-temperature synthetic processes are often needed, and the preparation, device design, and conditions have to be carefully optimized to obtain high quality semiconductors. In the case of perovskites, low temperature (< 150 °C) and simple techniques like spin-coating result in high-quality devices with ease.[22] Conventionally most perovskites are processed with solution-based techniques. This rather simple method uses solvents to dissolve all the chemical precursors followed by the removal of the solvent (often by annealing) to crystalize the perovskite.[23] Solution-based techniques have yielded perovskites that, when integrated into multiple (optoelectronic) applications, have led to record efficiencies. Nevertheless, there are some disadvantages and limitations with this processing technique, like the toxicity of some solvents, the limited choice of solvents for the metal precursor salts, limitations in composition freedom and stoichiometry due to the need for good solubility for all precursor materials, thickness control of the layer, and the difficulties in upscaling.[24] Therefore, alternative solvent-free methods to obtain perovskites are highly sought after, in particular scalable techniques leading to high-quality materials and films.

In 2013 Stoumpos et al. showed that it is possible to synthesize different metal halide perovskites by simple mechanochemical synthesis. [25] Mechanochemical chemistry refers to the branch of chemistry where the activation energy needed for a chemical reaction to occur is of mechanical origin, arising for example from impact, compression, or shear energy. With mechanochemical synthesis, the dry precursors are added together in the desired stoichiometric ratio, and simply by grinding them the perovskite phase is formed as depicted in **equation 1.4.**

$$\mathrm{AX(s)} + \mathrm{BX_2(s)} \xrightarrow{MCS} \mathrm{ABX_3(s)}$$ Equation 1.4.

This simple method can be performed by hand grinding with just a pestle and a mortar (**Figure 1.5a**), but to secure fully reacted precursor material, electrically powered ball-milling is preferred, where milling balls in a closed jar act as the grinding medium (**Figure 1.5b-c**). The precursor material is inserted in the mill jar and by setting the jar into motion (straight motion or rotational movement), the mechanical energy from the grinding medium is translated to the reaction mixture to form the perovskite. Parameters that can be tuned are the milling time, the rotation or shaking frequency, and the ball-to-powder weight ratio. Besides, the jars can be sealed and therefore the process can be performed in any desired environment like an inert atmosphere.

Owing to the simplicity of mechanical chemical synthesis, this solvent-free technique has no limitations in composition or stoichiometry, and high-purity perovskite materials are formed. For example, it has been shown that all the pure 3D lead halide perovskites can be obtained with excellent phase purity, and besides it is possible to include additives, form mixed phases, produce lead-free perovskites, and create perovskite structures of different dimensionality.[26] This technique is already used in the pharmaceutical industry, hence, it has proven scalability. The disadvantages of this technique are limited to inhomogeneous particle size distribution and possible contamination by abrasive wear.

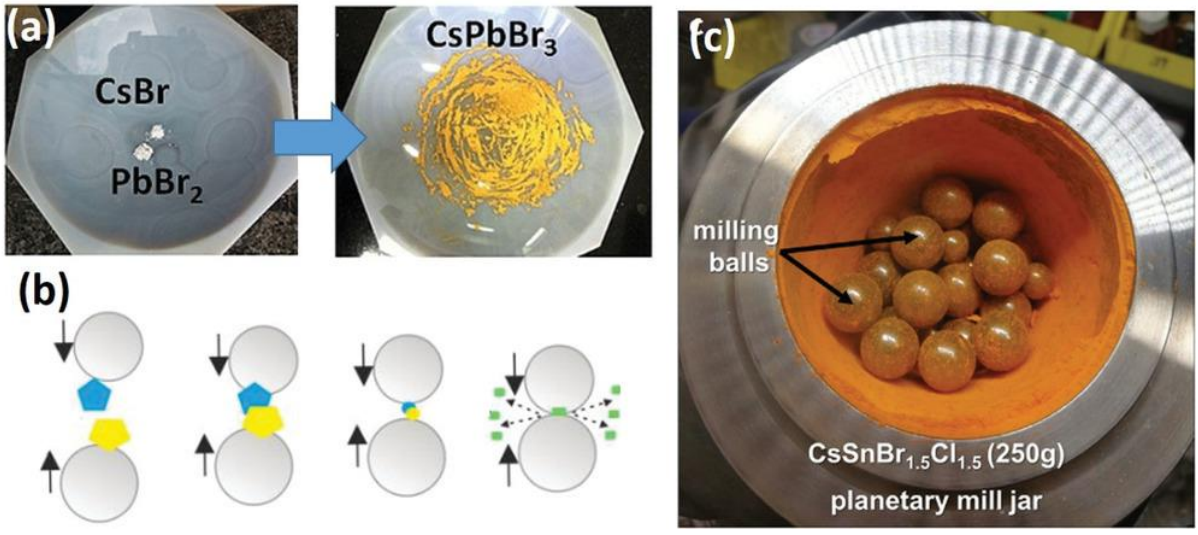

Figure 1.5. Mechanical synthesis process. (a) Precursor materials (CsBr and $PbBr_2$) where $CsPbBr_3$ is formed by hand grinding. (b) Impact of two milling balls on pre-cursor material to form perovskite phase. (c) Inside of a planetary mill jar with a perovskite end product.[26]

1.4. Processing of perovskite powders

As above stated, there are many advantages to the synthesis of perovskites by mechanochemical synthesis. However, for most applications, the perovskite powders have to be further processed, for example into a thin film if the perovskite has to be used in an optoelectronic device. In the following, a short summary of some methods to process perovskite powders into films is described.

Thermal evaporation

In thermal evaporation, the perovskite is deposited as a film on a desired substrate by sublimation under a high vacuum. In general, thermal evaporation is performed by heating the target material once the system is under vacuum (**Figure 1.6a)**. Once the sublimation temperature of the material is reached at a given pressure, the material starts to sublime and condenses on any surface that has a temperature below its sublimation temperature, such as the chamber walls and a suitably positioned substrate. The thickness of the films is commonly tracked, by quartz crystal microbalances, and sub-nanometer thickness accuracy can be reached. This method works well with materials that have a sublimation temperature well below its decomposition temperature. Perovskite precursors can, in general, be sublimed in a controlled manner as they fulfill the above-mentioned requirement. Perovskite powders, in particular when composed of mixed inorganic and organic components (hybrid), have a decomposition temperature below their sublimation temperature. Therefore, the sublimation and decomposition processes compete, and only when the sublimation is carried out very fast ("flash evaporation"), perovskite films can be obtained. Hence it is not straightforward to achieve a stoichiometric conversion from powder to film. Also, not all components (like some additives) can be sublimed, which limits the type of compositions that are feasible to evaporate. Single-source evaporation is most successfully employed for inorganic perovskites (that do not decompose before the sublimation temperature) and to produce thin films (< 200 nm). Furthermore, the performance of the devices produced nowadays by single-source evaporation is still lacking with respect to the simultaneous co-sublimation of the perovskite precursors.[27]

Melt processing

In this process, the perovskite powder is heated above its melting point and slowly cooled down to induce perovskite recrystallization (**Figure 1.6b**).[28] Here the melting temperature needs to be lower than the decomposition temperature, which is rarely the case for hybrid perovskites.

Hence, when melting, partial decomposition of the perovskite can also occur. By melting perovskite powders it is not trivial to reach thicknesses below 100 micrometers due to the limited flow (high viscosity) of the molten perovskite. Such very thick films are not suitable for most thin film optoelectronic applications.

Pressing

Perovskite powders can be pressed under high pressure (10-350 MPa), forming a compact rigid pellet. These pellets are often studied as X-ray detectors because of the thickness (> 50 micrometers) which can be achieved with this process.[29] Like with the melting processed perovskites, the considerable thickness hinders their use for several thin-film applications. It has also been shown that very high pressures can induce defects and structural changes in perovskites.[30–32] The mechanical properties of the perovskite-based disks are typically poor, as they are very brittle, difficult to handle and to integrate into devices.

Aerosol deposition

With the aerosol technique, powders are accelerated at high speeds (100 to 600 ms^{-1}) due to pressure difference and arrive in a deposition chamber with a pressure of approximately 1-10 mbar, reaching the substrate (**Figure 1.6c)**. Due to the speed, the particles break up and form a crystalline layer.[33,34] This technique is still in its infancy for metal halide perovskites and more research has to be performed to overcome the problem of pores and cracks in the film.[35]

Pulsed laser deposition

In pulsed laser deposition, the perovskite powder is first pressed into a thick pellet that is then used as a target. In a low-pressure chamber, a pulsed laser is used as a direct energy source to ablate a small volume of the target pellet which is transferred into a plasma directed on a substrate, where the perovskite is deposited (**Figure 1.6d**).[36,37] Only limited research has been carried out so far to produce metal halide perovskite films with this technique. Some of the challenges here are to have a one-to-one stoichiometric conversion from the target material to the substrate, and the difference in the elemental distribution of the plasma plume.[36] These challenges are particularly severe in the case of hybrid perovskites.

Wet powder processing

In wet powder processing, the perovskite powders are dissolved and then processed as a film. Dissolving pre-formed perovskite material in a solution rather than dissolving the precursors separately has two main advantages. First, solutions with pre-formed perovskites demonstrated increased stability over time compared to those obtained by adding pre-cursors.[38,39] Secondly,

it has been shown that an insoluble precursor material can be made soluble in the same solvent when it is incorporated into the pre-formed perovskite.[40] While positive results are achieved in this manner, it still requires the use of solvents and wet coating methods to prepare thin films.

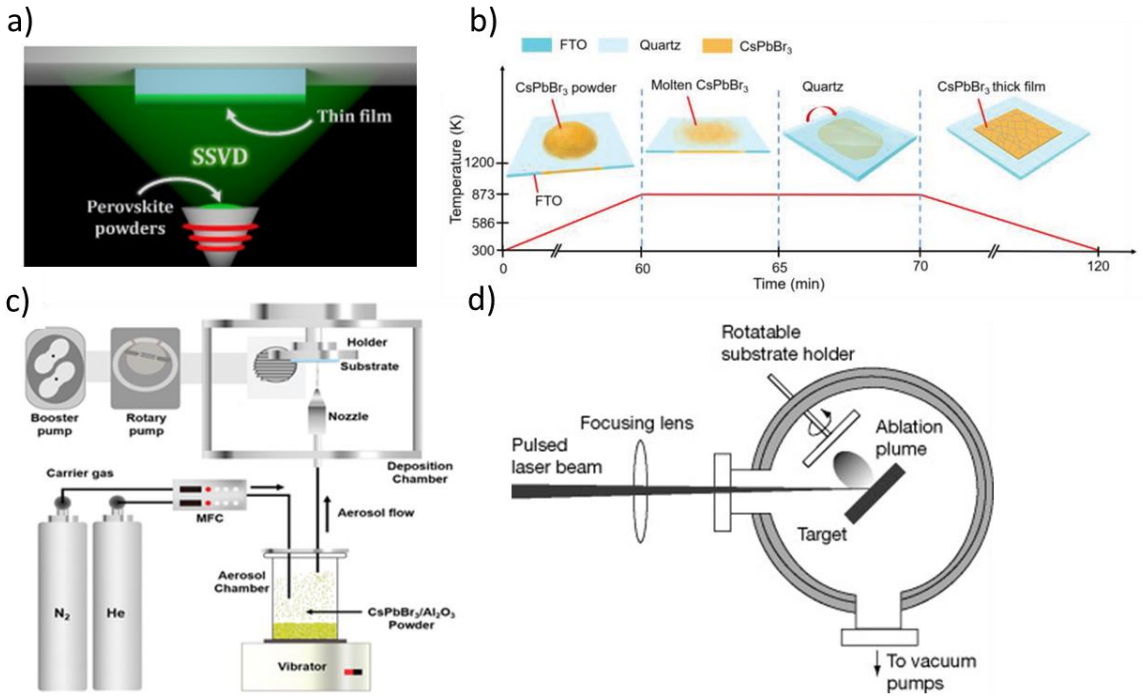

Figure 1.6. (a) Sketch of a single-source vacuum deposition setup, where perovskite powder is heated and evaporated in a low-pressure chamber.[41] (b) Melt process of $CsPbBr_3$ powder to a thick film.[28] (c) Schematic view of an Aerosol deposition tool.[33] (d) Scheme of a PLD system.[42]

1.5. Aim of the thesis

This thesis aims to develop a novel dry processing route to convert perovskite powders synthesized by mechanochemical synthesis into solids with dimensions and mechanical properties suitable for optical and optoelectronic applications. In particular, the focus is on photon conversion and detection.

To accomplish the general goal of the thesis, a dry synthetic route for the preparation of perovskite powders has been developed, which is detailed in **Chapter 2** and used throughout the thesis. The method relies on the mechanochemical synthesis of perovskites, the preparation

of polymer-perovskite composites, and its processing into stable thin disks by hot-pressing. As a first proof-of-concept, these materials are applied to high-quality color converters with high luminescence efficiency and promising stability, which is attained with a relatively low thermally stable perovskite formulation.

To expand the range of applications of the perovskite-polymer disks, it is imperative to create electrical contacts, which would allow to prepare optoelectronic devices. This is the aim of **Chapter 3**, where a simple lamination method is developed to fabricate lateral photoconductors with the polymer-perovskite disks used as the absorber materials. The methodology for the fabrication and optimization of lateral photoconductors is presented, realizing both broadband and narrowband detectors processed at mild conditions without the use of solvents.

In lateral devices, the active region of a semiconductor is limited by the electrode spacing, and by the charge diffusion length in the normal direction. To enlarge this region and use the full volume of the disk, vertical devices with contacts on both sides of the material should be prepared. A process to obtain vertical devices from polymer-perovskite composites is described in **Chapter 4**. As the thickness of the disks can be easily tuned from tens to hundreds of micrometers, these devices have potential for direct X-ray detection, which is the main application targeted in this chapter. Such devices would be of special relevance for applications in dosimetry for medical safety.

Chapter 2

Polymer-encapsulated halide perovskite color converters

2.1. Introduction

In this chapter, the processing technique that is used throughout this thesis to process perovskite powders, which relies on mixing the perovskite with an inert thermoplastic polymer, is introduced. Furthermore, perovskite-polymer formulations are optimized and studied for color converter applications. The perovskite methylammonium lead bromide ($MAPbBr_3$) is selected as it can lead to highly luminescent particles. To increase the perovskite luminescence efficiency, it is prepared by mechanochemical synthesis in the presence of the additive amantadine hydrochloride. The blending of these passivated perovskite particles with the thermoplastic polymer is then carried out by continued milling of the powder in the mechanochemical synthesis reactor. Three polymers are evaluated, namely: poly(methyl methacrylate (PMMA), polystyrene (PS), and polyethylene oxide (PEO). The synthesized powders are then pressed into thin disks that have a high photoluminescence quantum yield and depending on the perovskite concentration and thickness are semitransparent or opaque. These perovskite polymer composites are stable in air for over 2 months. By inserting a secondary emitter, white light can be obtained by illuminating it with a blue light source. This novel solvent-free technique to obtain highly luminescent perovskite–polymer composites in moldable shapes shows a promising route for the preparation of color converters.

2.1.1. Color converters

Color converters transform incident light to a desired wavelength longer or shorter than the incident wavelength, in a process called down- or up-conversion, respectively. Most color converters are used for down-conversion applications in LEDs and are nowadays widely used in commercial displays to convert the initial light source (often blue) to the desired color in the visible spectrum (**Figure 2.1a**).[43] The working mechanism of a common type of color converter is based on the photoluminescence process in semiconductors (**Figure 2.1b**). First, an incident photon with energy greater than the bandgap of the semiconductor excites an electron from the valence band to the semiconductor's conduction band, leaving behind a hole in the valence band (excitation). The excited electron and hole will eventually relax to the bottom of the conduction band in the case of the electron and to the top of the valence band for the hole by thermalization (energy relaxation). At last the electron and hole recombine by

releasing a photon with an energy equal to the bandgap of the semiconductor (radiative recombination). Therefore, the converted light is dependent on the bandgap energy of the semiconductor material the color converter exhibits.

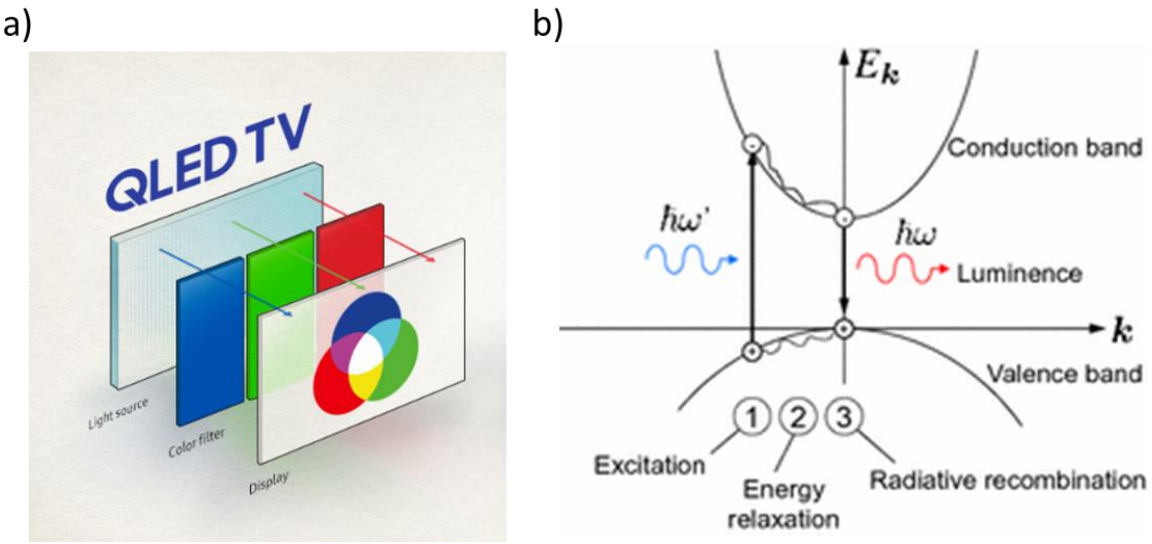

Figure 2.1. (a) QLED TV screen, with one light source and three color converters.[44] (b) Photoluminescence process of a direct semiconductor.[45]

2.1.2. Figures of Merit.

PLQY

The PLQY measures the yield of the emission with respect to the excitation and can be described in the following simple manner:

$$PLQY = \frac{Number\ of\ photons\ emitted\ by\ sample}{Number\ of\ photons\ absorbed\ by\ sample} \times 100\% \qquad \text{Equation 2.1.}$$

For an efficient color converter, a PLQY close to 100% is desirable to avoid conversion losses. However, due to non-radiative recombination pathways in the absorber material, this is often not achieved.

FWHM

The FWHM is of importance for the color purity of the converted light. A high color purity can be obtained when the emission spectrum of the color converter is narrow and dominantly emits one specific wavelength. The FWHM can be broadened by electronic disorder in the material, scattering, and trap states in the material, among others.

Color coordinates

The color coordinates link the distribution of wavelengths in the visible spectrum, with the physiologically perceived colors in human color vision. To take into account the perception of colors of the human eye, color matching functions are used, which match every wavelength with a different weight according to the sensitivity of the human eye at that specific wavelength. In this way, the color coordinates of a spectrum can be calculated by summing the product of the emitted spectrum with the color-matching functions at each wavelength. The color coordinates can be visualized by the color gamut (**Figure 2.2a**). This color gamut shows the color pallet that our human eye can distinguish, where every color has a specific coordinate, the color coordinates. A wide-color gamut display produces an image that can resemble a wider range of colors detectable by the human eye, which is favorable for most applications. Therefore, the color coordinate of the color converter is important. For example, when a screen uses three filters as can be seen in **Figure 2.1a**, each filter will have its color coordinate in the desired color. When combining the three color converters, a triangle can be constructed in the color gamut by connecting the color coordinates of each color converter as is done for the virtual screens 1 and 2 (**Figure 2.2a**). The area of the triangle shows the different color coordinates the three filters together can produce. Therefore, screen 2 can reproduce more colors and is said to have a wide color gamut, while screen 1 can reproduce just a few colors. The difference between two screens with different color gamut is visualized in **Figure 2.2b**.

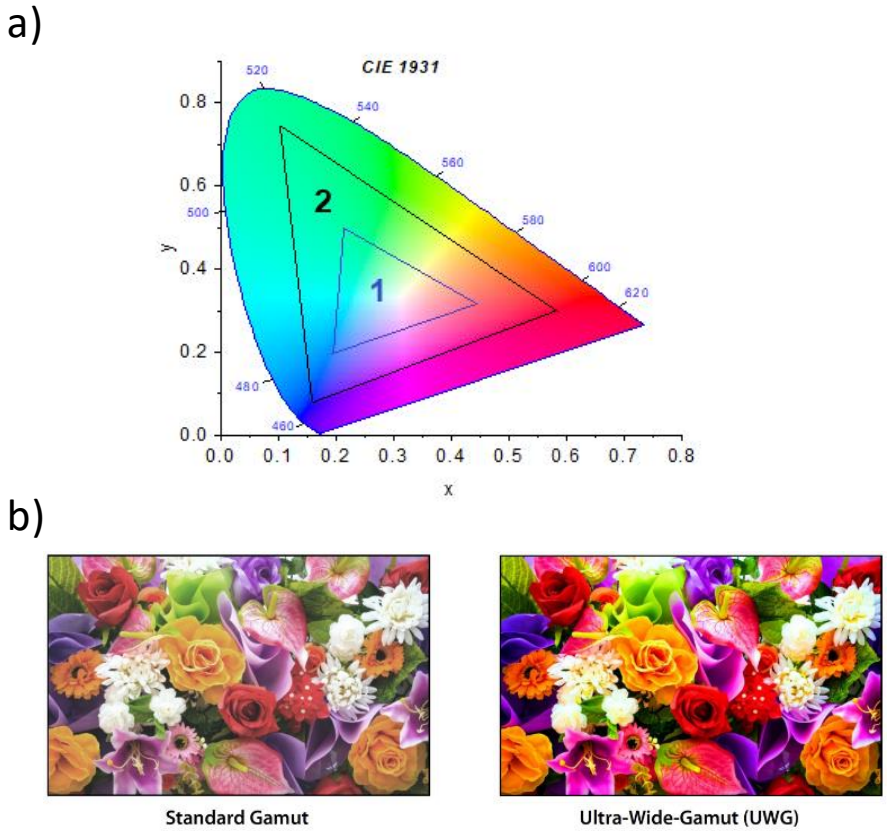

Figure 2.2. (a) CIE1931 color gamut where the two triangles represent two virtual displays with three color converters, where triangle 1 represents a low color gamut display and triangle 2 a wide color gamut. (b) Two TV screens with different color gamuts.[46]

2.1.3. Motivation and Aim

Metal halide perovskites are well suited as emitters in color converters as they fulfill all requirements above described. They can have a high PLQY, and a narrow FWHM (<30 nm) leading to a high color purity, and their emission wavelength can be tuned by the composition of the perovskite**.** Additionally, they have a high optical absorption coefficient for high-energy photons, and the material costs are low.[47–53] These unique properties can make halide perovskites interesting for commercialization in displays.[54,55]

Metal halide perovskites are generally prepared using solvent-based processes. Due to the different solubility of the precursor salts and additives, it is not always trivial to reproducibly control the final composition (and thus the optical properties) of the perovskite-based

emitters.[56] Residual solvents have also been reported to affect the perovskite stability and optical properties.[57,58]

Mechanochemical synthesis is an alternative, solvent-free, method to prepare highly luminescent perovskite materials.[59–62] Mechanochemical synthesis has shown the capability to easily adjust the composition or introduce an additive into the system without any extra difficulties for the synthesis itself.[63–65] It is a reproducible method and it has a high versatility to the final composition, making it a desirable route to prepare color converters. In this chapter, the aim is to produce high-performing and stable color converters from perovskite powder by dry mechanochemical synthesis.

2.2. Synthesis and Characterization

2.2.1. Synthesis

As discussed before, to obtain high-performing color converters, the initial perovskite powder must have a high PLQY. In previous reports, highly luminescent $MAPbBr_3$ perovskite powders were obtained by mechanochemical synthesis by introducing AmCl into the precursor mixture. By adjusting the stoichiometric amount of AmCl with respect to Pb(II) and methylammonium bromide, a PLQY as high as 29% for $MAPbBr_3$+50%AmCl was achieved.[65] The perovskite is synthesized by mechanochemical synthesis, where an electric MM-400 straight ball mill from Retsch is used combined with zirconia ball-mill jars with a volume of 10 mL and 2 zirconia beads of 10 mm in diameter **(Figure 2.3a-b)**. Here, the $MAPbBr_3$+50%AmCl perovskite formulation is reproduced with the same setup due to the relatively high reported PLQY. A load of 1 mmol of MABr, 1 mmol of $PbBr_2$, and 0.5 mmol of AmCl are ball-milled at a frequency of 30 Hz.

After the formation of the highly luminescent perovskite powders, a polymer is added to the system. The addition of the polymer has several advantages. First, most perovskites are known to degrade rapidly when in contact with ambient conditions. To compete with commercial color converters, the stability of perovskites needs to be improved.[66] One way to protect the perovskite from these influences is to shield the perovskite from the environment. Multiple articles have shown that polymers can passivate and protect the perovskite from getting in

contact with the environment.[67–70] Secondly, the partial substitution of the perovskite with the polymer material can have extra advantages for structuring the color converter.[71–73]

The effect of three commonly available thermoplastic polymers, namely PMMA, PS, and PEO, was evaluated. These polymers were selected as they are transparent and are frequently used as passivation or encapsulation material for perovskites.[74–79] To ensure a thorough mixing with the previously prepared luminescent perovskite powder, these powders and the polymer were mixed and ball-milled together for an additional 3 minutes. Notably, the perovskite powder and the mixed powders are not further processed to reduce or uniform the size of the particles.

The addition of the polymer to the perovskite allows to press the perovskite-polymer composite into thin disks at relatively low pressure and temperature. The Atlas constant thickness filmmaker and the Atlas series heated platens from Specac are used as mold and as temperature sources to heat the mold (**Figure 2.3c-e**). This setup is designed to produce up to 2.9 cm diameter round disks, where a maximum pressure of 4 metric Tons can be applied. To adjust the thickness of the disk, different spacer rings between the bottom and top mold can be introduced. Therefore, adjustable thicknesses of 15, 25, 50, 100, 150, and 500 µm can be produced with this setup. In order not to damage the polished mold, the temperature of the mold is set above the glass temperature of the used polymer by the heated platens. Furthermore, in between the bottom and top surface of the mold aluminum foils are used to prevent sticking of the powder mixture with the mold.

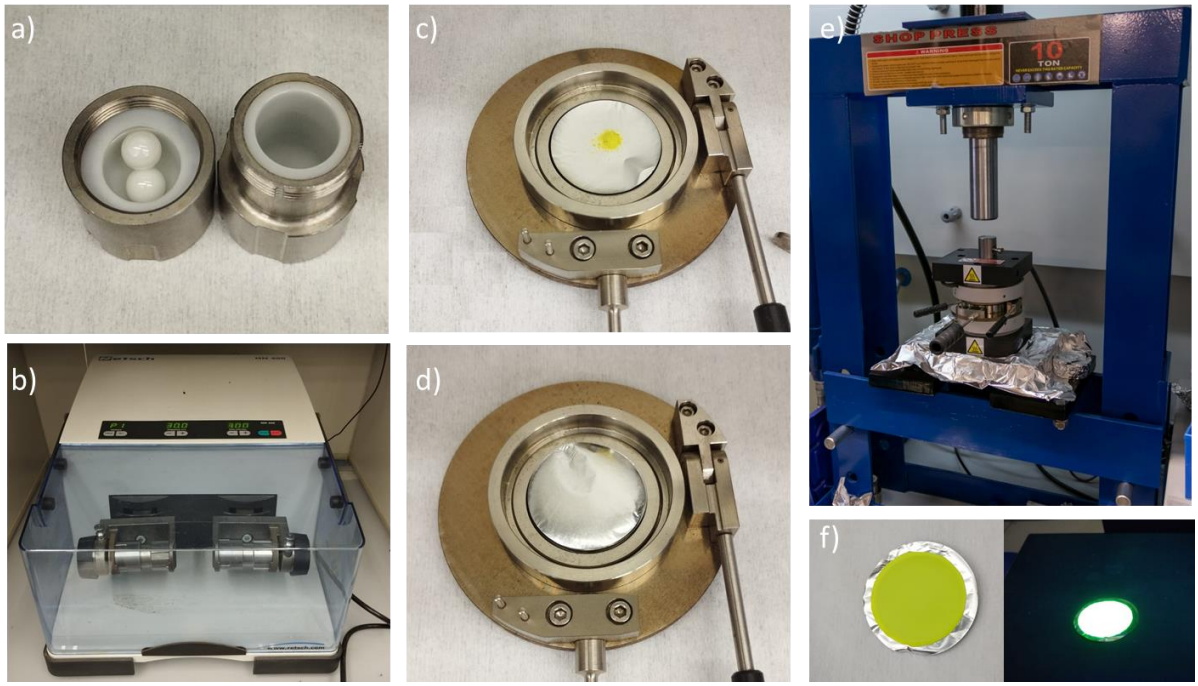

Figure 2.3. (a) Zirconia ball-mill jar and 2 zirconia beads. (b) Electric-powered straight ball mill from Retsch. (c) The bottom part of the mold where an aluminum foil separates the desired perovskite-polymer powder from the polished surface of the mold. (d) An extra aluminum foil is applied on top of the powder to separate the powder from the top part of the polished mold. (e) The mold sandwiched between the two heated platens placed under the press. (f) Photo of the obtained disk under normal light conditions and UV light of 365nm.

Important factors to consider before pressing the powder into a disk are the temperature of the mold, the pressing time, and the final force applied. To select the maximum temperature, first, the thermal stability of the perovskite material is studied by thermogravimetric analysis (TGA) under ambient conditions. With this method changes in mass of a specimen are measured while its temperature is increased in a dynamic manner (5 °C/min in this case). Therefore, the loss of volatile components can be measured at different temperatures. In **Figure 2.4a** the TGA analysis is visualized in the region from 100 to 200 °C. In this region, the first mass loss is observed around 130 °C, suggesting the initial degradation of the perovskite. Therefore, this point will be the maximum temperature where the disk can be pressed without altering the perovskite composition.

As a consequence of the implementation of the thermoplastic polymer in the perovskite-polymer composite, a solid disk can already be formed when a temperature is applied above the glass temperature of the polymer, and below the temperature where volatile components

are released from the perovskite structure making it feasible to process relatively low thermally stable perovskites. Since it is possible to form a solid disk by pressing the powder in a few seconds, the pressing time is set for a short period (10 seconds). Longer pressing times were also studied, but this did not lead to any improvement in the properties of the disk, and pressing times of 10 minutes or longer would even cause perovskite degradation.

In **Figure 2.4b-c** the PLQY and the FWHM of the final disks when pressing the perovskite-polymer powders containing PMMA or PS at different mold temperatures are presented. As can be observed, the PLQY for both polymers is unaltered till a temperature of 130 °C. When increasing the mold temperature to a temperature of 160 °C the PLQY for the PMMA holding powder is quenched. Interestingly the FWHM of the PL is decreasing with temperature for the PS holding disks, which can be related to an increase in viscosity of the polymer and therefore better passivation of the perovskite particles. Given the results above, a temperature of 130 °C at a pressing time of 10 seconds is set as a standard for the PMMA and PS holding disks. Since the PEO polymer has a lower melting temperature, a lower temperature of 70 °C is set. Increasing the temperature above the melting temperatures of the polymer and applying pressure can lead to non-uniform films and therefore temperatures significant above the melting point are not applied. At these settings also different pressing forces were studied, but this didn't have an impact on the final properties of the disks, which is likely due to the spacer ring that prevents the increase in pressure. Only at lower temperatures, where the polymer is not viscous enough, a higher pressing force can help to achieve the desired thickness.

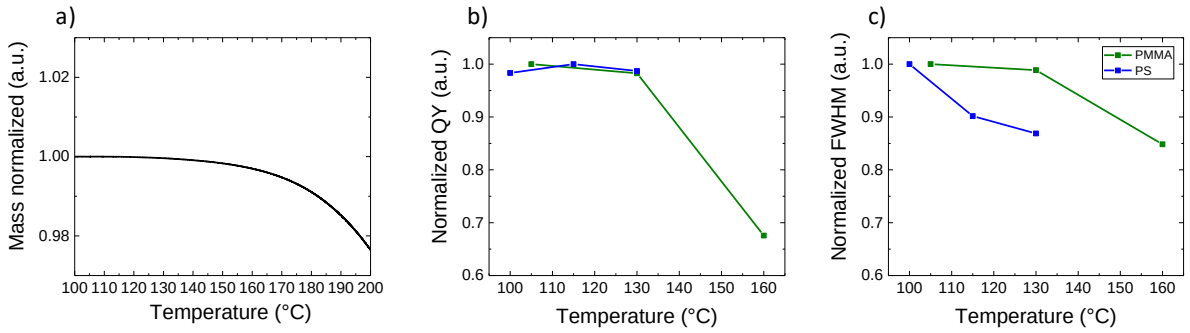

Figure 2.4 (a) TGA of the $MAPbBr_3$ + 50wt.%AmCl perovskite under ambient conditions, where a dynamic temperature is set at 5°C/min. (b) PLQY from the PS and PMMA disks are stated at different pressing temperatures and fixed pressing time of 10 seconds and a pressure of 1.5 metric Tons. The starting temperature is at the glass temperature of the two polymers which is 100 °C and 105 °C for PS and PMMA respectively. (c) FWHM of the resulting PL peak at different pressing temperatures. During these variable temperatures the peak wavelength of the PL for PS and PMMA didn't change significantly, ±2 nm and ±4 nm respectively.

In short, in this chapter, the disks are obtained by applying a pressure of 1.5 metric tons for 10 seconds. The mold temperature was set at 70 °C for the PEO-containing and at 130 °C for the PMMA and PS-containing composite powders. A spacer ring with a thickness of 25 µm is used to define the final thickness of the pressed disks, resulting in disks with a thickness between 25 and 30 µm.

2.2.2. Characterization

Scanning Electron Microscopy

The scanning electron microscope (SEM) is used to obtain microscopic pictures of the ball-milled powder. To obtain the image a Phenom Desktop SEM is used while measuring with the backscattered electron detector and the secondary electron detector in a 50:50 mix.

PLQY, FWHM, and color coordinates characterization

To measure the PLQY, the FWHM, and to calculate the final color coordinates an integrating sphere connected with a monochromatic light source and photonic multichannel analyzer is

used. The PLQY setup consists of a UV-VIS-NIR Absolute Photoluminescence Quantum Yield Spectrometer C13534-11 from Hamamatsu.

X-ray diffraction

X-ray diffraction (XRD) is performed to observe if the $MAPbBr_3$ crystal phase is maintained during the addition of polymer or production of the powder to the thin disk. Here, an Empyrean diffractometer from Malvern Panalytical equipped with a Cu Kα anode operated at 45 kV and 40 mA. Single scans were acquired in the theta = 5° to 50° range in Bragg-Brentano geometry in air. With Bragg-Brentano geometry the X-ray source and detector are placed at a fixed radius from the sample, fixed in a horizontal plane. Both source and detector are moved at the same time so that incident and diffracted beams impact and leave the sample at the same angle.

Reflectance and transmittance measurements

To measure the reflectance and the transmittance of the samples (powder or film) an integrating sphere is connected with a light source and detector. Here, as a source, an Avantes AvaLight DH-S-BAL deuterium halogen lamp is used and the light is collected by an Avantes reflection integrating sphere connected with an Avantes AvaSpec-2048L spectrometer. The substrate holder can be either black to exclude transmitted light or reflective to include transmitted light in the detection.

2.3. Results and Discussion

As stated in the introduction, the perovskite $MAPbBr_3$+50%AmCl is selected, because of the relatively high reported PLQY of 29%. In a different study, the importance of the ball-milling time with respect to the absolute photoluminescence (PL) of $CsPbBr_3$ was observed, noticing that prolonged ball-milling of the $CsPbBr_3$ leads to a loss of the PL.[80] The effect of the ball-milling time on the PLQY of the resulting composition $MAPbBr_3$+50%AmCl is investigated, and an optimum ball-milling time of 1 hour is observed, which leads to perovskite powders that have a PLQY of 49%. The perovskite powder contains a range of different particle sizes, where the smallest particles have a size of at least as small as 100 nm and the largest particles are up to ~3 µm (**Figure 2.5**).

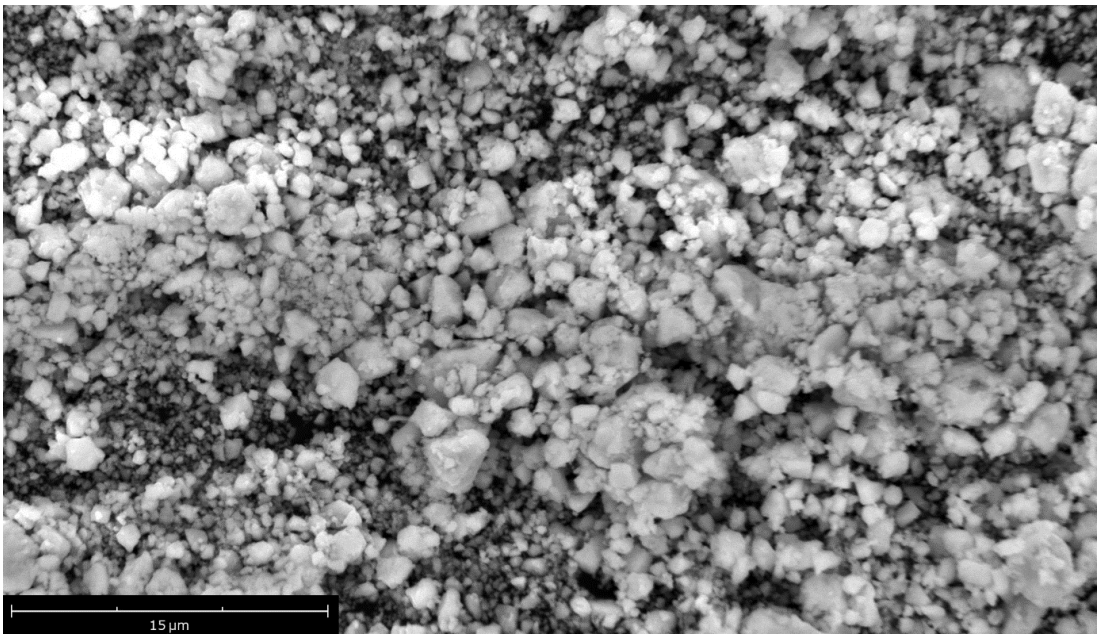

Figure 2.5. SEM image of perovskite particles after mechanochemical synthesis of 1 hour.

After the formation of the highly luminescent perovskite powders, a polymer is added to the powder. The effect of three thermoplastic polymers PMMA, PS, and PEO was evaluated. The optical properties of the pristine perovskite powder are compared with the perovskite powders to which the polymer was added (33wt.% $MAPbBr_3$+50%AmCl with respect to the polymer). **Figure 2.6a** depicts the normalized PL spectrum of the pristine perovskite powder which is obtained from a spectrometer equipped with an integrating sphere. The maximum of the emission spectrum is around 524 nm. Adding any of the polymers does not result in a significant shift in this maximum, but the FWHM of the PL is reduced when the polymers are introduced to the perovskite powders. In addition, the PLQY, deducted from **Figure 2.6b**, for the PS and PMMA-containing powders is increased to 55%, while the PLQY of the PEO-containing powders is reduced to 38%. The increase of the PLQY and reduction of the FWHM when introducing PMMA and PS is an indication that these polymers are passivating the perovskite surface/grain boundaries.

To study the effect of the polymers on the perovskite in more detail, structural analyses were performed. In **Figure 2.6c** the XRD data reveals that the pristine perovskite powder has the expected orthorhombic perovskite diffraction peaks.[65] When adding PMMA or PS, the perovskite-related diffraction peaks are preserved and no extra diffraction peaks are observed. This is different for the PEO-containing perovskite, where additional diffraction peaks appear, indicating the formation of additional crystalline phases different from the original orthorhombic perovskite. PEO is a known additive to passivate perovskites and the origin of

this passivation is discussed in multiple papers.[74,81–84] The consensus is that the hygroscopic PEO shares the C-O lone-electron pair with the empty 6p-orbital of Pb^{2+} in the perovskite, forming a Pb–O bond.[74] While this can passivate the surface of a perovskite when for example PEO is spin-coated on top of a film, this bonding of the PEO with the perovskite is also capable of hindering the formation of the orthorhombic perovskite phase when PEO is added during ball-milling.

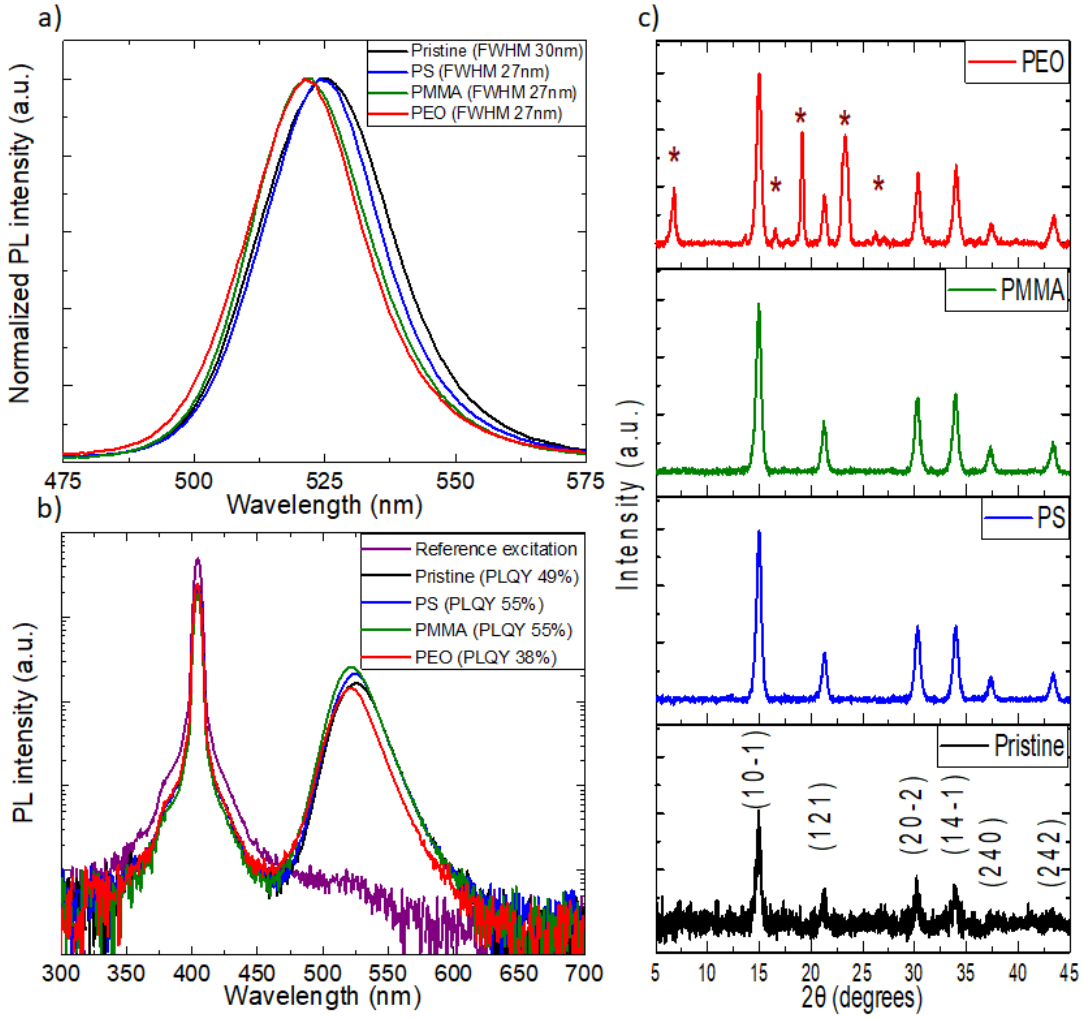

Figure 2.6. (a) Normalized PL emission of the ball-milled powders when excited by a 405nm laser, where pristine is the perovskite without polymer. In the legend, the FWHM of the PL is stated in nanometers. (b) PLQY spectra where the powders were excited at 405 nm (reference excitation) and a spectrometer coupled to an integrated sphere from Hamamatsu was used to obtain the spectra and the PLQY. In the legend, the PLQY of the powders is stated in percentages. (c) XRD pattern of the different powders. The indices display the orthorhombic perovskite diffraction peaks (ICSD collection code 158306). The asterisks at the diffraction pattern of PEO indicate the non-orthorhombic diffraction peaks.

To convert the powders into useful emitting elements, the perovskite-polymer composite powders are pressed into thin disks by heating the powder in a mold under high pressure. In **Figure 2.7a** the normalized PL spectra of the different thin disks are plotted together with that of the pristine perovskite powder. The PL spectra of the PMMA and PS-containing disks show no distinguishable shift with respect to that of the pristine perovskite powders, while the PL spectrum of the PEO-containing disk is blue-shifted. Taking into account the FWHM values of the PL from **Figure 2.7a** and the PLQY values from **Figure 2.7b**, the disk containing PS combines the best optical properties, with a PLQY of 53%, and a FWHM as narrow as 23 nm. The disks containing PMMA have almost the same PLQY (47%) and FWHM (31 nm) as the pristine perovskite, while the PLQY of the PEO-containing disks is reduced to 16% and the FWHM is around 28 nm. Taking into account the fact that the whole process is solvent-free and only moderate temperatures are employed for short times, these high PLQY values for the PMMA and PS holding disks are promising for applications.

To investigate the effect of the disk processing conditions on the perovskite composition, the XRD patterns were evaluated (**Figure 2.7c**). The PMMA and PS-containing disks have XRD patterns that are similar to those of the perovskite powders and no extra diffraction peaks are observed. For the PEO-containing disk, the XRD pattern demonstrates that the orthorhombic perovskite diffraction peaks are suppressed, which is especially noticeable at the higher angles. Furthermore, the additional diffraction peaks already observed when the PEO is added to the powders became more intense. This indicates that the amount of non-orthorhombic perovskite structures increases when processing the powders into the disks. Due to these negative effects of the insertion of PEO and the processing into a disk, the PEO disks for the following experiments are excluded.

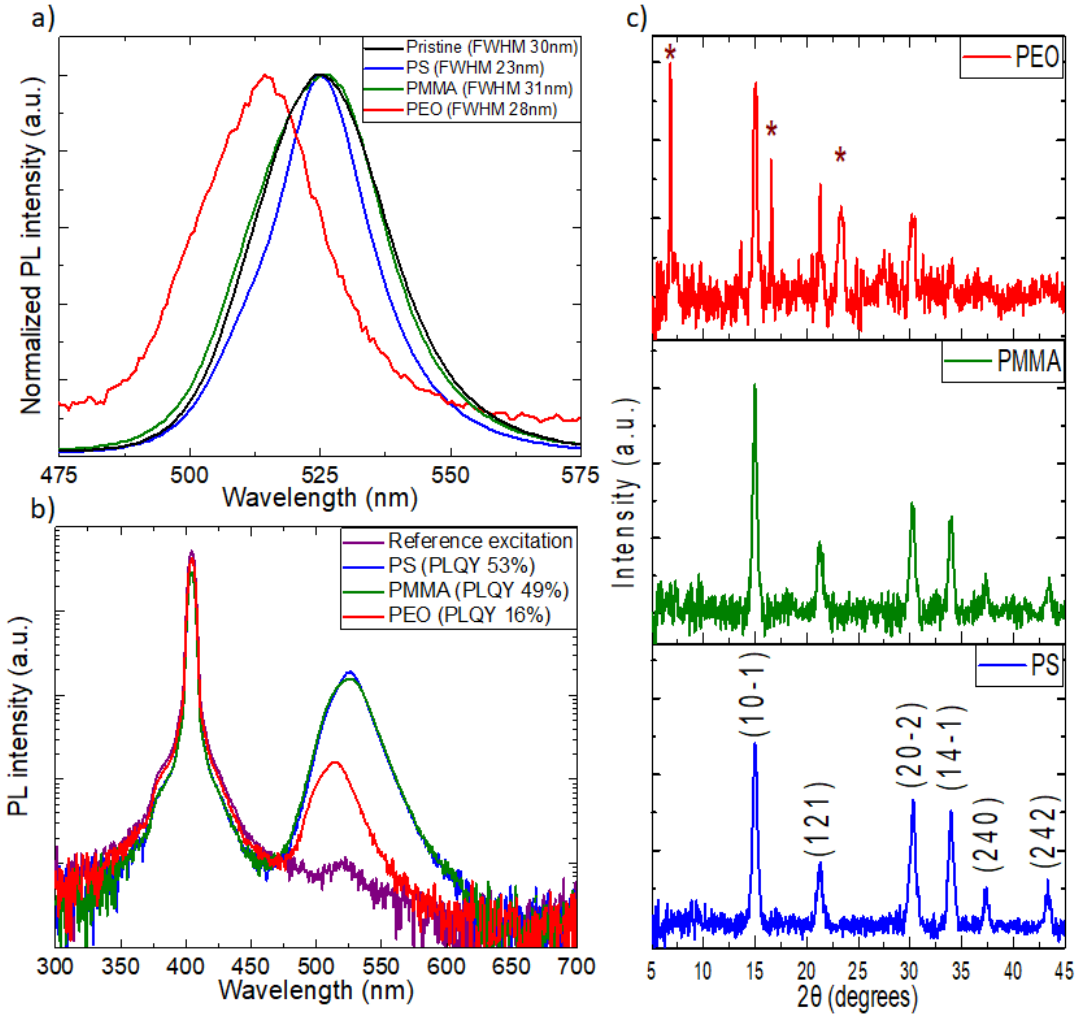

Figure 2.7. (a) Normalized PL emission of the 33 wt.% perovskite disks when excited by a 405nm laser, where pristine is the perovskite powder without polymer. In the legend, the FWHM of the PL in nanometers is stated. (b) PLQY spectra where the disks were excited at 405 nm (reference excitation) and a spectrometer coupled to an integrated sphere from Hamamatsu was used to obtain the spectra and the PLQY. In the legend, the PLQY of the disks is stated in percentages (c) XRD pattern of the different powders. The indices display the orthorhombic perovskite diffraction peaks (ICSD collection code 158306). The asterisks at the diffraction pattern of PEO indicate the non-orthorhombic diffraction peaks.

The stability of the color converter is an important factor. As mentioned before, encapsulation of the perovskite by polymers can enhance the stability of the perovskite significantly. For example, in an earlier study by Hintermayr et al., methylammonium lead trihalide perovskite nanocrystals were encapsulated by polymer micelles. These encapsulated nanocrystals

maintain almost 60% of the initial PL after 130 days in ambient conditions, whereas the non-capsulated nanocrystals degraded completely in 13 days.[85] A common method to measure the stability is to monitor the PLQY value of the color converter over time under different conditions.[86] One of the frequently used stressing conditions is the stability of the color converter under ambient air conditions. Under these conditions for 62 days, the fabricated disks with PS and PMMA maintain 83% and 77%, respectively, of the initial PLQY. As a comparison, the PLQY of the pristine perovskite powder without the added polymer dropped to 26% of the initial value in just 7 days in ambient conditions.

Another common stability test is to stress the disks at elevated temperatures. For this, the disks are placed on a hotplate at 85 °C in an inert atmosphere (N_2), and the PLQY loss is measured at set time intervals. **Figure 2.8** shows the normalized PLQY as a function of time at 85 °C. Both disks show a similar PLQY degradation and maintain some 70 % of the initial values after 2 months at 85 °C. Interestingly, the speed of degradation reduces over time. There is a partial recovery of the PLQY around day 28, which is difficult to rationalize but could be related to N_2-induced lattice recovery, as reported elsewhere.[88] These stability tests demonstrate that the color converters are also stable at elevated temperatures. It is known that PMMA can passivate under-coordinated Pb^{2+} ions, whereas PS is reported to passivate surface defects.[89–92] Overall, the increase in PLQY and the prolonged stability of the PS and PMMA-containing disks imply the passivation of the polymers on the perovskite particles with this processing method.

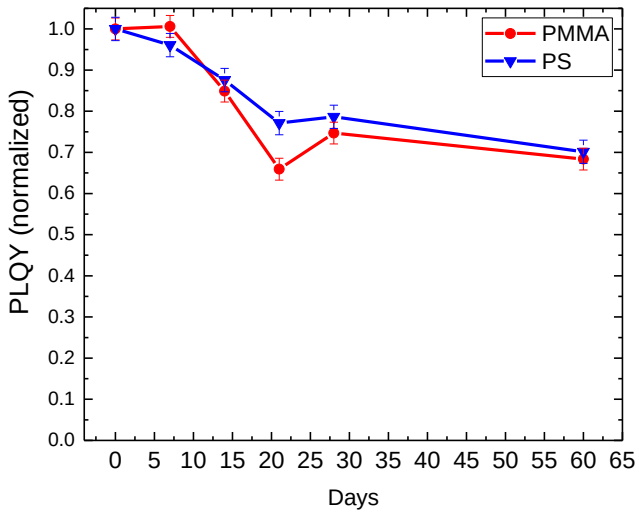

Figure 2.8. Normalized PLQY of the disks with 33 wt.% perovskite content as a function of time in an inert atmosphere at 85 °C.

The disks that are described so far, contain 33 wt.% $MAPbBr_3$+50%AmCl (with respect to the polymer) and are opaque. Hence, they can only reflect light as a color converter. It is more interesting to have semi-transparent color converters, which can be achieved by reducing the perovskite content with respect to the polymer. The PMMA-based disks are used to verify the optimum perovskite concentration in the polymer matrix. Disks were prepared with 0.5, 1, and 2 wt.% perovskite with respect to PMMA. The PLQY of the disks with 0.5 and 1 wt.% is roughly half of that of the opaque films, where the disks with 2 wt.% had a similar PLQY as the opaque films with the 33 wt.% perovskite with respect to PMMA (**Figure 2.9a**). The transmittance of the films reduces with increasing perovskite concentration and therefore, the perovskite loading was not increased beyond 2 wt.%. The transmittance for wavelengths beyond the absorption edge of the perovskite increases significantly reaching 72% at 600 nm for the disk containing 2 wt.% perovskite in PMMA (**Figure 2.9b**).

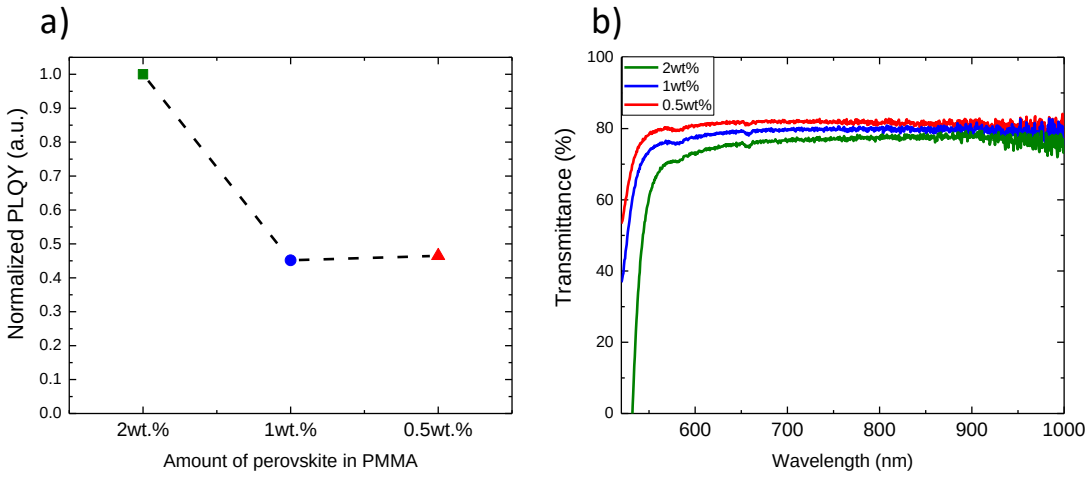

Figure 2.9. Optical properties of PMMA disks containing a low amount of the luminescent perovskites, 0.5, 1, and 2 wt.% with respect to PMMA. (a) Normalized PLQY with respect to the PLQY of the 33 wt.% PMMA disk as a function of perovskite concentration. (b) transmittance as a function of wavelength and perovskite concentration.

Now the properties of the semi-transparent and the opaque disks are compared with each other. The disks with a perovskite concentration of 2 wt.% are semi-transparent (**Figure 2.10a-b**) whereas those with 33 wt.% are almost completely opaque for the disks with thicknesses of 30 µm (**Figure 2.10c-d**). The disks with 33 wt.% perovskite in PMMA and PS have a below bandgap transmittance of 16% and 30%, respectively (**Figure 2.10e**). The low transmittance in

this wavelength range is due to the high reflectivity of the disks. The transmittance in this wavelength range increases when the content of the perovskite is reduced to 2 wt.%, resulting in a transmittance of above 72 and 75% for the PMMA and PS-containing disks, respectively. The PLQY of the disk with the 2 wt.% perovskite in PMMA is 48%, hence similar to what was observed for the more concentrated disks. The FWHM for the 2 wt.% perovskite-containing disks, however, is reduced to a value of approximately 20.5 nm. Hence, the reduction of the perovskite content improves the color purity without reducing the PLQY of the disks. For the PS-based disk with 2 wt.% perovskite, the PLQY increases to 60% and the FWHM is 21 nm, showing an improvement in optical properties, compared with the more concentrated perovskite PS disks. This hints at better passivation of the perovskite when increasing the polymer-to-perovskite ratio.

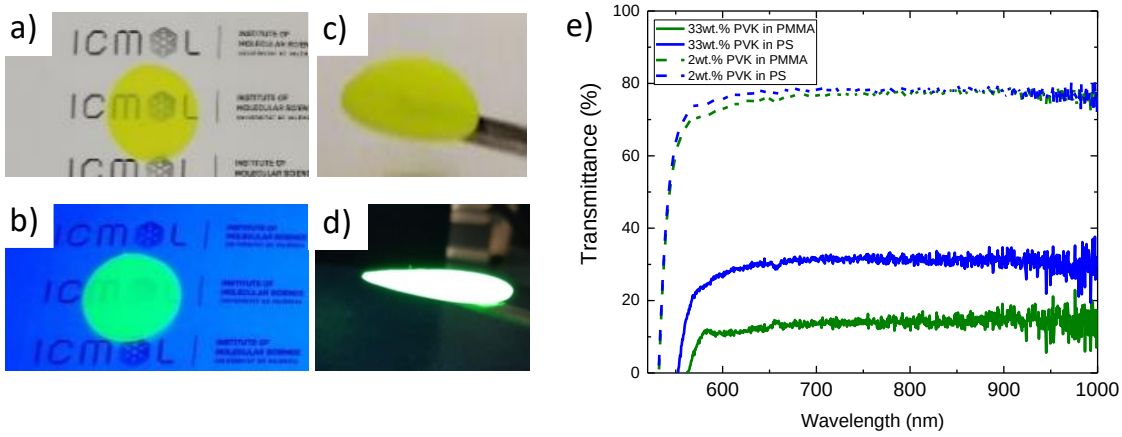

Figure 2.10. Photographs of PMMA disks containing 2 (a and b) and 33 wt.% (c and d) under ambient light and UV illumination (365 nm), respectively. (e) transmittance data for PMMA and PS disk with different concentrations of perovskites.

In **Figure 2.11a** the statistical distribution of the PLQY and FWHM of these disks are plotted. The width of the distribution of the properties is rather narrow, demonstrating the good reproducibility of this dry fabrication process. Higher PLQYs reaching 75 % were obtained when some of the disks were stressed at 85 °C for several weeks in an inert N_2 atmosphere, however, the origin of this increase in PLQY is not well understood.

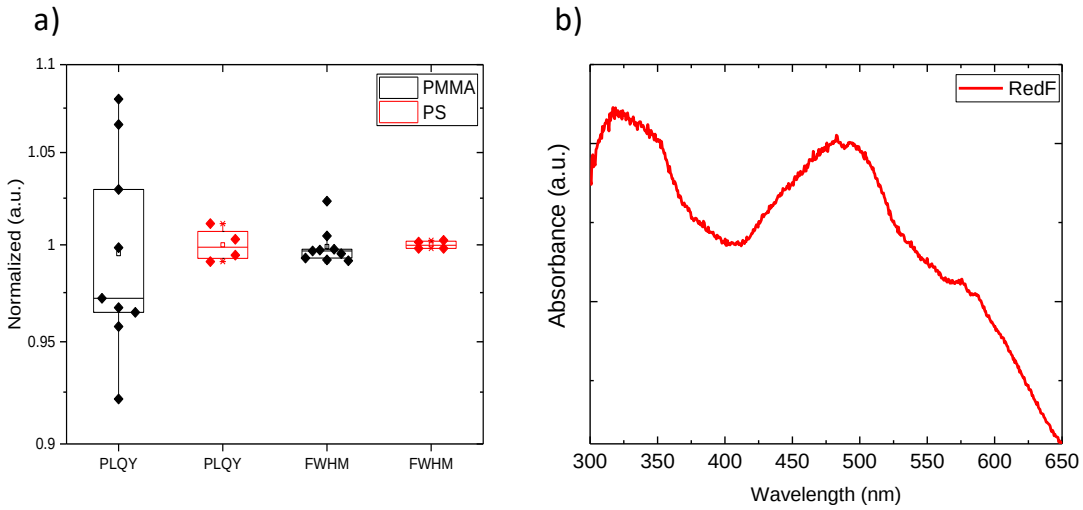

Figure 2.11. (a) Normalized statistics of the PLQY and the FWHM for the 2wt.% perovskite disks. Every solid dot represents a different disk. (b) Absorbance spectra of the light-emitting polymer RedF.

As mentioned, an additive such as AmCl can easily be incorporated into the perovskite-polymer complex since the process does not rely on solvents, and only moderate temperatures are used for a short period. As a proof of concept, a multiple-color emitter is prepared by inserting a fluorescent polymer in the perovskite/polymer disks. A commercial polyfluorene-based polymer named RedF from Sumitomo Chemical is used. RedF is selected because it emits at longer wavelengths, complementary to the emission spectra of the 2 wt.% $MAPbBr_3$+50%AmCl perovskite. Moreover, the disks have a high transmittance in the wavelength region where RedF emits. Importantly, RedF absorbs in the region where the perovskite also emits (see **Figure 2.11b**). Therefore, a low concentration of 2 wt.% RedF is selected, so the parasitic absorption of the RedF on the perovskite is reduced**.** The RedF is added to the PMMA and perovskite powder followed by 3 minutes of ball-milling. Accordingly, the powder mixture contains two light-emitting materials where $MAPbBr_3$+50%AmCl converts the incident blue light to green and RedF converts the incident blue light to red. This dual-emitter color converter is a simpler alternative to the frequently used stacked layers of two color converters.[93–95] Similarly as before, the powders are pressed into a thin disk. For comparison reasons, a RedF-only containing disk in PMMA is also prepared. In **Figure 2.12a** the photoluminescence spectra of this disk and the previously studied one containing only the perovskite composite are depicted. The emission spectrum of the dual emitter disks overlaps perfectly with the emission of both types of disks with only one of the

two emitters. The PLQY of the perovskite and RedF-only color converters are 48% and 60% respectively. When combining the two light-emitting materials, an orange color converter with a final PLQY of around 42% is produced. The decrease in PLQY is likely due to the partial reabsorption of the converted green light by the RedF emitter.

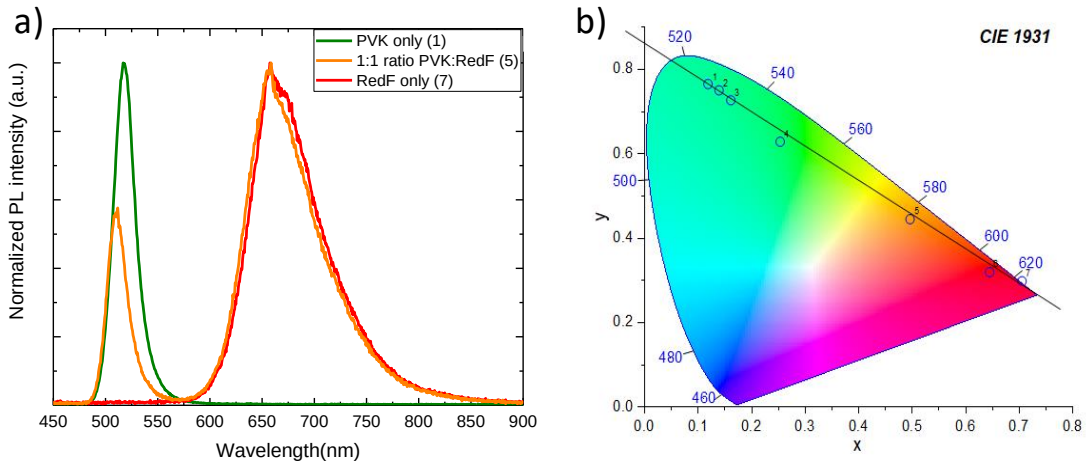

Figure 2.12. (a) Photoluminescence spectra of disks containing perovskite (PVK), Red F, and both at an individual concentration of 2 wt.% with respect to PMMA. (b) Color points depicted in the CIE 1931 graph from disks containing both 2 wt.% Red F and the 2 wt.% perovskite emitter in different ratios. Points number 1 to 7 have the following ratios of 2 wt.% PVK: 2 wt.% RedF: (1) PVK only (2) 99:1 (3): 90:10 (4) 67:33 (5) 50:50 (6) 33:67 and as last number 7 with only 2wt.% RedF.

Another way to specify the color converters is to look at their color points as represented in the CIE 1931 graph (**Figure 2.12b**). The color points were obtained from the emission spectra of the disks. The RedF-only (number 7) and perovskite-only (number 1) disks have color points lying at the extreme red and green of the CIE1931 graph. The color coordinates of the perovskite–only based disk are very close to the ideal green Rec 2020 standard. This implies that if the color coordinates of the perovskite emitter would be used for the green part of the Rec 2020 still >98% of the color gamut could be reproduced.[96,97] Disks that contain both the perovskite and RedF emitters have color points that fall on a line between the two single emitter-containing disks. This demonstrates the adaptability of this process. The above-described results show that with this synthesis method, it is possible to successfully produce a multiple (colored) color converter.

2.4. Conclusion

Polymeric disks containing highly luminescent perovskite emitters are prepared using a solvent-free process. Powders of widely available polymers are added to a previously mechanochemical synthesized luminescent $MAPbBr_3$ perovskite formulation. PMMA and PS are compatible with the perovskite and improved their luminescent properties reaching PLQY above 50%. Incorporating PEO in the perovskite powder results in a reaction with the bulk of the perovskite leading to a partial reduction of the PLQY. As luminescence polymer–perovskite powders do not have a form factor compatible with most applications, the powders are converted into thin disks. Importantly, by applying moderate temperature and pressure, it is possible to press the powders into thin disks while maintaining the luminescent properties and improving the stability. Hence, the presence of PMMA and PS improves the properties and allows the formation of mechanically robust disks. Depending on the perovskite content, semitransparent or opaque luminescent disks are obtained. Using a disk composition with 33 wt.% perovskite led to an opaque disk with a PLQY of 53% and an FWHM of 23 nm for the PS-containing disks and a PLQY of 48% and an FWHM of 28 nm for the PMMA-holding disk. Reducing the wt.% of the perovskite to 2% led to color converters with a PLQY of 60% and an FWHM as low as 21 nm for the PS. These properties make these disks excellent candidates for color converters as they have a very high color purity and high luminescence. The transmittance of these disks for wavelengths greater than 600 nm was above 72% and 75% for the PMMA and PS-based disks, respectively. A proof of concept, dual green and red light-emitting color-converting disks were also prepared by adding a fluorescent polymer to the perovskite during the mechanochemical synthesis, and subsequent pressing at moderate temperatures. The advantages of this dry process technology pave the way toward productive polymer-embedded perovskite color converter fabrication.

Chapter 3

Laminated polymer-encapsulated halide perovskite photoconductors

3.1. Introduction

In this chapter, a simple method to fabricate polymer-encapsulated halide perovskite photoconductors is presented. Dry mechanochemical synthesis is used to prepare $CsPbBr_3$ in the presence of poly(butyl methacrylate) (PBMA). The resulting composite powder is then heated and pressed into a free-standing disk with a thickness controlled by a metallic spacer ring. The disk is laminated on a glass substrate containing an interdigitated electrode, resulting in a planar photoconductor device. The best photoconductive performance is obtained for disks that consist of 75 wt.% of $CsPbBr_3$ in PBMA, reaching a detectivity of approximately $2 \cdot 10^{11}$ Jones. Moreover, by adjusting the thickness of the disk, narrowband detectors can be obtained due to charge collection narrowing. Depending on the thickness of the pressed disk, the position and width of the detectivity peak can be tuned. This work shows a simple and versatile approach toward the fabrication of halide perovskite photodetectors without the use of solvents.

3.1.1. Photoconductors

Photodetectors are widely used for optical communications, imaging, and biomedical sensing.[98–100] In short, a photodetector converts an optical signal to an electronic signal. Three main types of photodetectors exist, photodiodes, photoconductors, and phototransistors. Photodiodes include selective electron and hole transport layers that allow for current flow only in one polarization direction, while the layout of a photoconductor is simpler, consisting of a metal-semiconductor-metal structure.[101] The phototransistor has a similar design as a normal transistor, which consists of two p-n junctions. However, for the phototransistor the incident light can serve as an additional gate, altering the current of the phototransistor.[102] The working mechanism of photodetectors is based on the generation of an e-h pair when a semiconducting material is excited by a photon with an energy larger than the bandgap of the concerned semiconductor. However, where for the color converters the e-h pair recombines and emits a photon with an energy equal to the bandgap energy, in a photodetector the e-h pairs are extracted by an externally applied field before recombination takes place and therefore a photocurrent is produced. In a photoconductor, an applied voltage is needed to extract the e-h pair since there is no internal built-in voltage like in a photodiode (see **Figure 3.1**). The simple

structure of a photoconductor allows the use of simple device designs such as planar layouts, and therefore the fabrication costs are in general lower.

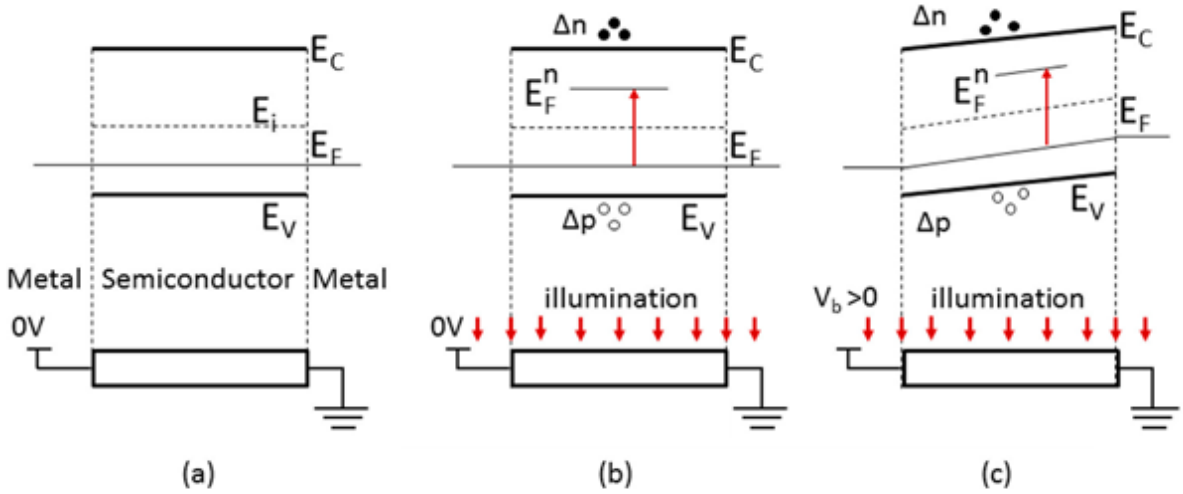

Figure 3.1. Simplified band-diagram of a metal-semiconductor-metal interface, where E_C and E_V are the conduction and valence band of the semiconductor, respectively, and E_F is the Fermi level.[103] (a) Band-diagram in the dark without external bias, where E_i is the intrinsic Fermi level of the semiconductor, but shifted due to alignment with the Fermi level of the metal. (b) Band diagram under illumination, but no applied external field. Electron and hole pairs are generated in the semiconductor but are not extracted by the metal. Furthermore, quasi-Fermi level splitting happens in the semiconductor due to the photogeneration of carriers, where E_F^n is the quasi-Fermi level splitting for electrons. (c) Band diagram under illumination and with an applied bias. Electrons and holes drift to the metal contacts, leading to a photocurrent.

Another advantage of photoconductors is the possibility to achieve gain, which allows a very high photocurrent per incident unit of optical power. The gain (G) can be formulated as in the following (for the full derivation of the gain mechanism in photoconductors see **Appendix A**):

$$G = \left(\frac{\tau}{t_e + t_h}\right) EQE \qquad \text{Equation 3.1.}$$

where τ is the excess carrier recombination lifetime, t_e, t_h the transit time of the electron and hole respectively, and EQE the external quantum efficiency, which is the ratio of the number of carriers extracted by the photoconductor to the number of incident photons.

Assuming that the mobility of one of the charge carriers in the semiconductor is far greater than the mobility of the other charge carrier, for example, if the mobility of the electron is far greater than the mobility of the hole ($\mu_e \gg \mu_h$), and therefore $t_e \ll t_h$ the gain can be expressed as:

$$G = EQE \left(\frac{\tau}{t_e}\right) \qquad \text{Equation 3.2.}$$

Gain will hence be attained if $\tau \gg t_e$. So in the case that the recombination time is far greater than (in this case) the transit time of the electrons, electrons can circulate many times before recombining with a hole, and therefore EQE higher than 100% can be achieved. To maximize this gain mechanism traps of the opposite carrier can be introduced in the semiconductor.[104] However, while photoconductive gain is favorable for the sensitivity of the device it is also accompanied by photoconductive lag, which is a lag in the photocurrent response caused by the flow of excess injected carrier from one of the contacts for a period that depends on the lifetime.[105]

Besides the three different types of photodetectors, the detectors can also be classed between narrowband and broadband, based on the width of their spectral response. Broadband photodetectors have a wide spectral response range and are applied in multicolor detection, while narrowband photodetectors are used to detect certain spectra, where other wavelengths that are not in the desired spectra should be excluded or negligible. Narrowband photodetectors are often used to exclude false signals from the environment.[106] While the spectral range for broadband photodetectors is dependent on the absorption of the used semiconductor, narrowband photodetectors often rely on optical filters to be color-selective. To avoid the use of additional components such as optical filters, the difference in absorption coefficient at different wavelengths in thick semiconducting layers can be used to attain selective narrowband response. Photons with shorter wavelengths are absorbed relatively close to the surface of the material, where most of the generated electron-hole pairs will form. If the charge carrier diffusion length is shorter than the semiconductor thickness, photogenerated charges will not be collected and hence not contribute to the photocurrent.[106] On the other hand, low-energy photons are absorbed more homogeneously through the section of the material, leading to charge collection and photocurrent. Therefore, by optimizing the thickness of the absorber material, narrowband photodetectors with a spectral range close to the bandgap of the semiconductor can be obtained.

3.1.2. Figures of Merit

Responsivity

The responsivity is defined as the photocurrent per incident unit optical power (AW^{-1}), representing the photoelectric conversion capability of a photoconductor at different wavelengths, and can be described as follows:

$$R = \frac{q\lambda}{hc} EQE \qquad \text{Equation 3.3.}$$

where q is the elementary electron charge, λ is the wavelength, h is the Planck constant, and c is the speed of light.

External quantum efficiency (EQE)

The EQE represents the ratio of the number of excited electron–hole pairs extracted by the photoconductor to the number of incident photons. Where for most optoelectronic devices, for example in solar cells, this cannot exceed 100%, it can exceed for photoconductors due to the gain mechanisms described above.

Specific Detectivity

The specific detectivity is a figure of merit used to characterize the performance of a photodetector. The photosensitive area is taken into account and therefore the sensitivity of two different detectors can be compared to each other. This resolves in the following formula:

$$D^* = \frac{\sqrt{A\Delta f} \cdot R}{i_n} \qquad \text{Equation 3.4.}$$

Where D^* is the specific detectivity in Jones, A the active area of the detector, Δf is the electrical bandwidth, and i_n is the noise current. There are three contributions to noise that limit D^*: the shot noise from dark current, Johnson noise, and thermal fluctuation ´´flicker´´ noise.[105] On the premise that the shot noise is commonly assumed to be the dominant contribution, the expression of D^* can be written as:

$$D^* = \frac{R\sqrt{A}}{\sqrt{2qI_{dark}}} \qquad \text{Equation 3.5.}$$

Where, A the active area of the detector, q is the elementary electron charge, and I_{dark} is the dark current of the device.

Response time

This is an important figure of merit as it defines the speed of the detector. Generally, the response time is the time it takes for the photocurrent to rise (fall) from 10% to 90% (90% to 10%) of the maximum photocurrent under excitation with a light pulse.

3.1.3. Motivation and Aim

The semiconducting material employed determines to a large extent the characteristics of photoconductors, such as their response speed and spectral sensitivity.[107] Metal halide perovskites are widely studied semiconductors, due to their favorable optoelectronic properties, simple processing, and easy tunability of their properties.[108–110] As a result, high-performing visible light photodetectors have been demonstrated using perovskites.[101,111–114] However, several challenges remain regarding stability, the realization of filterless narrowband photodetectors, as well as very broadband photodetectors. Additionally, processing methods compatible with large-scale production in industrial environments are still to be demonstrated.[101,111,113,114] Solvent-free, low-cost, simple production processes are advantageous to bring some of these devices closer to the market.

In the previous chapter, mechanochemical synthesis is used for the preparation of perovskite-polymer composites for color converters. Here the investigation continues for the possible application of perovskite-polymer composites as an absorber layer in photoconductors. Furthermore, the possible application as filterless narrowband photoconductors is investigated, since the process enables thick disks with ease.

3.2. Synthesis and Characterization

3.2.1. Synthesis

The synthesis technique to obtain polymer-perovskite disks has the same steps as explained in the previous chapter, however, a different perovskite material and polymer are used. First, the inorganic halide perovskite $CsPbBr_3$ was selected as the absorber material for the

photoconductor due to its high thermal stability and simple processability. The perovskite was mechanochemical synthesized by adding 1.5 grams of stoichiometric ratio of cesium bromide and lead bromide in a zirconium ball jar of 10 mL followed by ball milling at a frequency of 30 Hz for 5 minutes with a Rensch MM400.[115]

To obtain lateral photoconductors, the disks need to be attached to a substrate without using any additional layers. To reach this goal and to keep the process simple, hot roll lamination was selected to adhere the disk to a substrate with a pre-patterned interdigitated electrode. Here, an interdigitated tin-doped indium oxide (ITO) layout with 28 ITO contacts with each a spacing of 40 µm and a length of 4960 µm is used. However, to be able to laminate the disks on a substrate by simple hot roll lamination, the polymer needs to be mechanically stable, flexible, and able to adhere to the substrate. Therefore, several transparent and inert polymers were screened (**Table 3.1**) on their mechanical stability and adhesion properties with the substrate. The polymers are pressed into disks and their mechanical stability is evaluated by performing a 5 mm radius bend test. Next, the polymers are tested on their adhesive properties with the interdigitated substrate. First, the substrates are cleaned by different ultrasonic baths of soap, water, and isopropanol, followed by 20 minutes of UV treatment. Then, the polymers are tested to adhere to the substrate by simple hot-roll lamination at different temperatures. For the lamination, a 420 W hot/cold laminator is used, where the rolls of the laminator can be heated up to 160 °C.

Polymer	**Passed 5 mm radius bend test**	**Substrate adhesion**
Poly(methyl-methacrylate)	No	No
Polystyrene	No	No
Poly(ethylene oxide)	No	No
Poly(isobutyl methacrylate)	No	At 100 °C
Poly(butyl methacrylate)	Yes	At 100 °C
Poly(ethyl methacrylate)	Yes	No
Poly(benzyl methacrylate)	No	At 100 °C
Poly(cyclohexyl methacrylate)	No	No
Kollicoat MAE	No	No
Poly(tert-butyl acrylate-co-ethyl acrylate-co-methacrylic acid)	No	At 160 °C
Poly(methyl methacrylate-co-ethyl acrylate)	Yes	No

Table 3.1. Compiled list of polymers and their processability.

As can be observed from the table, from all the polymers tested, PBMA (visualized in **Figure 3.3a)** was the only polymer that passed both the bending and the adhesion tests. Furthermore, PBMA has a very low parasitic absorption since PBMA absorbs only in the UV region (< 300 nm) (**Figure 3.3b**), comparable to that of the glass substrates used in the devices. Therefore, PBMA in powder form was added to obtain the desired polymer-perovskite ratio and the mixture was ball-milled for an additional 3 minutes at a frequency of 30 Hz to obtain a thoroughly mixed polymer-perovskite composite.

Then the perovskite-polymer powder was heated up to 100 °C and pressed for 1 second at 2 metric Tons, using a spacer ring to obtain a 100 µm thick mechanical stable disk (**Figure 3.3c**). Once the disks are produced, they can be laminated on the desired substrate to produce the photoconductor (**Figure 3.3d**). If needed the disks can be cut into a desired shape to have a better fit with the substrate.

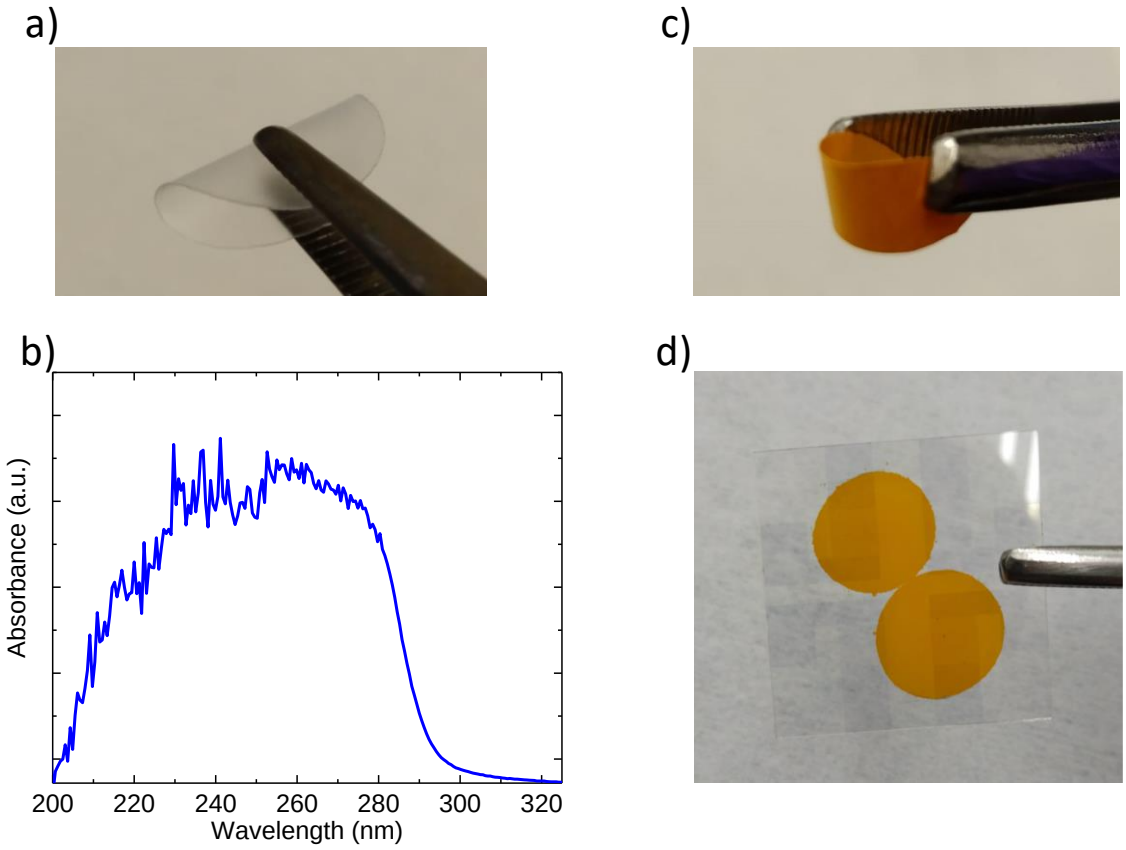

Figure 3.3. (a) Photograph of a PBMA disk. (b) Absorbance spectra of a PBMA disk. (c) Photograph of a disk of 75 wt.% $CsPbBr_3$ in PBMA. (d) Photograph of a device with two disks adhered on a substrate with interdigitated electrodes.

3.2.2. Characterization

Optical characterization

The PL measurement was performed using a 405 nm Matchbox laser where the signal is measured by an Avantes AvaSpec-2048L spectrometer. The reflectance of the disks was measured using the Avantes AvaLight DH-S-BAL deuterium halogen source connected with an Avantes reflection integrating sphere and collected by the Avantes AvaSpec-2048L spectrometer.

X-ray diffraction

X-ray diffraction was measured with the same setup as the former chapter using a Panalytical Empyrean diffractometer equipped with CuKα anode operated at 45 kV and 40 mA and a Pixel

1D detector in scanning line mode. Single scans were acquired in the 2θ = 10° to 50° range in Bragg-Brentano geometry in air.

Current-voltage (IV) measurements

To measure the dark current and the photocurrent the device was connected to a Keithley source measure unit. The measurement was carried out in a black metal case, to avoid parasitic light and minimize electrical noise. For the photocurrent, white light illumination is used with a power density of 100 mW cm^{-2}.

External quantum efficiency

The EQE measurements were measured by exciting the devices with a Quartz Tungsten Halogen lamp filtered by a monochromator from Newport (see **Figure 3.4**). The monochromatic light is mechanically chopped and synchronized with a lock-in amplifier. In this way, the dark current is subtracted and the pure photocurrent can be measured. Before measuring the desired cell, a silicon reference cell is measured to calibrate the power of the lamp.

Photo-response

The photo-response was measured by modulating a Matchbox 405 nm laser with a 1 Hz signal generated by a function generator. The 1 Hz pulsed laser was directed on the device and the output signal of the device was measured by an oscilloscope.

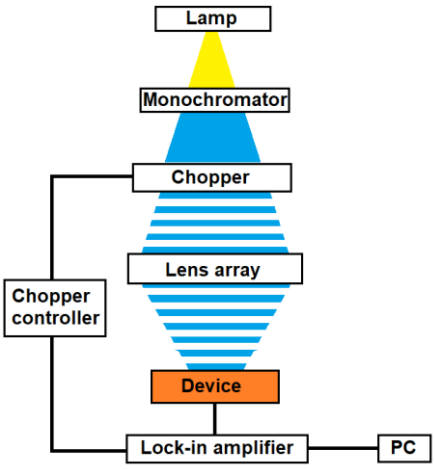

Figure 3.4. Schematic representation of the EQE setup.

3.3. Results and Discussion

Initially, the effect of the perovskite content on the physical properties of the composite was studied. In **Figure 3.5a-b**, the optical properties of the disk with different perovskite loading (expressed in weight percentages, wt.%) in PBMA are reported. From the reflectance measurements in **Figure 3.5a**, it is visible that all disks have a cut-off around 530 nm, which is in agreement with the bandgap of $CsPbBr_3$.[116] In **Figure 3.5b** the photoluminescence spectra of the different disks, when excited by a 405 nm laser are shown. The spectra are very similar independent of the perovskite concentration, although there is an optimum in the intensity for the disk containing 50 wt.%. This is most likely due to a more complete encapsulation of the $CsPbBr_3$ regions as the amount of PBMA is larger in this composite. For all the disks the most intense PL peak is at approximately 525 nm ± 2 nm, and there is a secondary PL component visible at lower energy around 540 nm. The lower-energy emission is typical for an orthorhombic bulk $CsPbBr_3$ perovskite, whereas the PL peak at 525nm is explained by weakly-quantum-confined (i.e., ‘‘nano’’) $CsPbBr_3$ particles.[115,116]

The X-ray diffraction (XRD) patterns of disks with different perovskite loading in PBMA are reported, together with the XRD pattern of the pure as-prepared $CsPbBr_3$ powder in **Figure 3.5c**. The pristine $CsPbBr_3$ powder shows a diffraction pattern compatible with that of an orthorhombic phase, as expected at room temperature.[117,118] This diffraction pattern is maintained when adding the PBMA to the perovskite powder and when these powders are pressed into thin disks with different perovskite concentrations. Both the XRD and PL measurements are consistent with the formation of polycrystalline orthorhombic $CsPbBr_3$ perovskite in the composite disks.

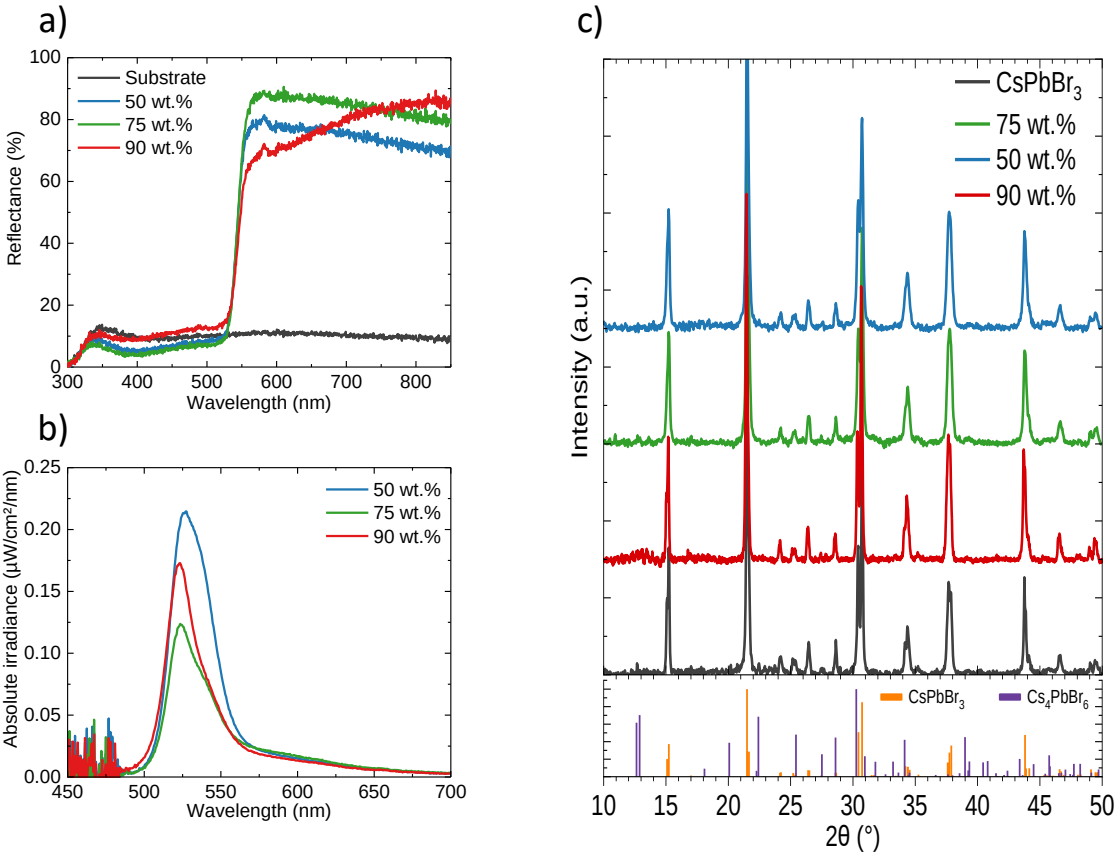

Figure 3.5. (a) Reflectance spectra of disks with different concentrations of $CsPbBr_3$ laminated on a glass substrate (black reference). (b) Photoluminescence spectra of the different disks, excited by a 405 nm laser. (c) XRD pattern of the initial ball-milled $CsPbBr_3$ powder and the patterns of the disks with different wt.% of $CsPbBr_3$ in PBMA. In the lower section, the reference patterns of $CsPbBr_3$ (COD ID: 4510745), and Cs_4PbBr_6 (COD ID: 1538416) are reported.

The disks laminated on planar interdigitated ITO electrodes are then characterized for their photoconductive properties. To characterize the devices, the current vs. voltage (IV) curves are measured in dark conditions and under illumination, as well as the external quantum efficiency (EQE). In any photodetector, a high EQE is desired, since the responsivity (R) and therefore the specific detectivity (D*) are directly dependent on the EQE. Furthermore, it is obvious that a low dark current is desirable to maintain a low noise level of the device, as this regulates the specific detectivity (see introduction 3.1).

First, IV curves are measured in dark conditions and under white light illumination (100 mW cm^{-2}) for the photoconductors with disks containing perovskite PBMA composites with different perovskite contents (**Figure 3.6a**). The voltage is swept from negative to positive bias. Interestingly, the dark current increases with increasing perovskite content in the composite material. This might be related to a better charge percolation with higher perovskite content, or a transition from hopping transport between the perovskite particles to bulk semiconductivity.[119] Under illumination, the photoconductor with 75 wt.% and 90 wt.% perovskite shows the highest photocurrent.

In **Figure 3.6b** the EQE of the photoconductors with different content of $CsPbBr_3$ in PBMA, recorded under an applied field at 2.5 V/µm (100 V applied bias), are reported. All devices show a cut-off around 2.3 eV, which agrees with the bandgap of $CsPbBr_3$.[120] As expected from the photocurrent measurements, the photoconductor with 75 wt.% and 90 wt.% $CsPbBr_3$ in PBMA shows also the highest EQE, where the EQE decreases when decreasing the perovskite concentration to 50 wt.%. For the photoconductor with 75 wt.% perovskite in PBMA, the EQE exceeds 100% in certain regions, a consequence of the gain mechanism typically observed in photoconductors.[121] Besides the EQE, the responsivity of the devices is displayed in **Figure 3.6b**. The responsivity is similarly constant over the visible-UV range, which is desirable for any photodetector and not always observed in the case of perovskite photoconductors.[122,123]

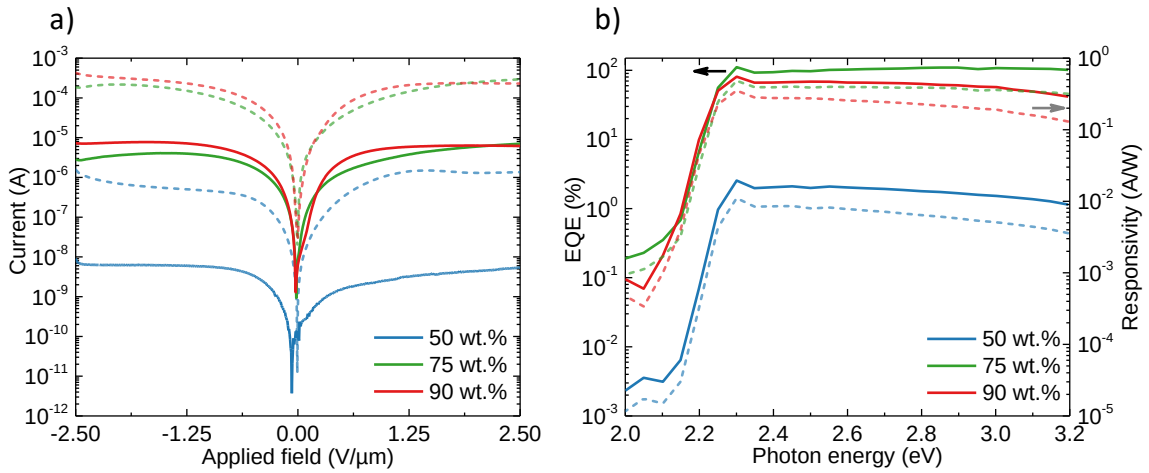

Figure 3.6. (a) IV curves under dark conditions (solid lines) and under white light illumination (dashed lines). (b) The solid lines represent the EQE of the devices with different weight percentages of perovskite with respect to PBMA under an applied field of 2.5 V/μm. The dashed lines are the corresponding responsivity.

To evaluate the reproducibility of the processing method reported here, the device configurations with different perovskite content were repeated several times with different batches of ball-milled powder. In **Figure 3.7** the statistics of the different devices are plotted for the dark current, responsivity, and detectivity, respectively. Although the 90 wt.% devices observed similar performances as the 75 wt.% devices, the yield of working devices for 90 wt.% is very low (<20%). The low yield of working devices is likely due to bad lamination of the disk on the substrate or due to cracks in the film, because of the small amount of PBMA. Due to the low reproducibility of the 90 wt.% devices and the fact that the 75 wt.% show similar performance, the 90 wt.% devices were not analyzed for their time response. Observing, the devices with 50 and 75 wt.% perovskite content, small differences in the dark current can be observed at different wt.% for the different devices, but overall most devices have a dark current mean value of $2.8 \cdot 10^{-8}$ A for the 50 wt.% devices, and of $2.3 \cdot 10^{-6}$ A for the 75 wt.% devices. The mean value of the responsivity (R) of the 50 wt.% photoconductor (0.028 A/W) is approximately one order of magnitude lower than the mean value of R for the device with 75 wt.% perovskite (0.42 A/W). Furthermore, the responsivity of the photoconductor with 75 wt.% perovskite seems more consistent, with a much narrower data distribution. Finally, from the dark current and the responsivity data, an estimation of the specific detectivity of the

different devices can be calculated using **equation 3.5**. This resulted in D* with a mean value of $7 \cdot 10^{10}$ Jones for the photoconductor with 50 wt.% perovskite. Increasing the perovskite content to 75 wt.% leads to a mean value of $2 \cdot 10^{11}$ Jones. Also, for the 75 wt.% perovskite composite, another batch of eight devices was measured with a lower applied field of 1.25 V/µm, resulting in a mean value of 10^{11} Jones. The difference in dark currents over the devices is likely due to different ambient conditions the powders are pressed during half a year of processing devices. It is known that humidity can affect the semiconducting properties of $CsPbBr_3$. Therefore, to enhance reproducibility it is suggested to press in a controlled environment, like a humidity chamber. Overall, the devices showed very promising reproducibility despite the simple fabrication in ambient air.

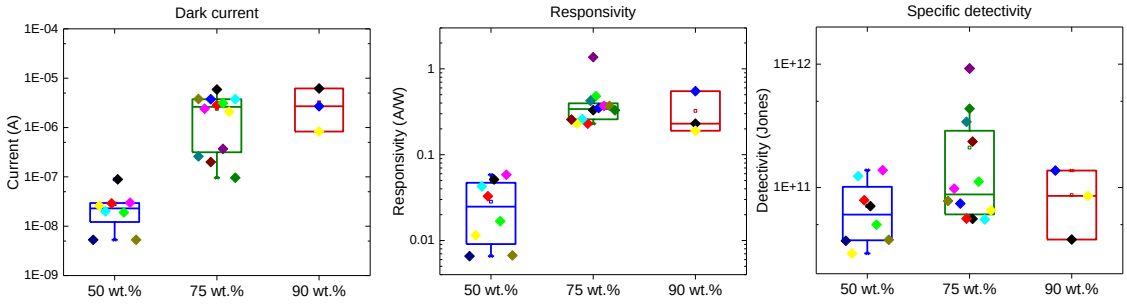

Figure 3.7 Statistics of device parameters for several photoconductors with 50, 75, and 90 wt.% perovskite at an applied field of 2.5 V/µm. Every colored dot represents a different device.

As discussed earlier, another important figure of merit for photodetectors is their rise and fall time. To calculate the response time, a pulsed laser with a wavelength of 405 nm at a frequency of 1 Hz excites the device and the response of the device is measured. In **Figure 3.8** the response of a 75 wt.% perovskite device is reported, showing a rise time of 1.78 ms and a fall time of 8.63 ms, at an applied field of 2.5 V/µm. In the same figure, the response of a 50 wt.% perovskite device is displayed at an applied field of 2.5 V/µm, where a rise time of 13.5 ms and a fall time of 28.9 ms were measured. The increase in rise and fall time with a lower amount of perovskite can be related to the lower conductivity of the 50 wt.% perovskite devices (**Figure 3.6a**). Also, in general, a higher applied field results in a faster response time for the device due to a higher drift velocity.[124,125] Indeed, when measuring a 75 wt.% perovskite device

where a lower field of 1.25 V/µm is applied the rise and fall time were increased to 12.2 and 55.9 ms, respectively.

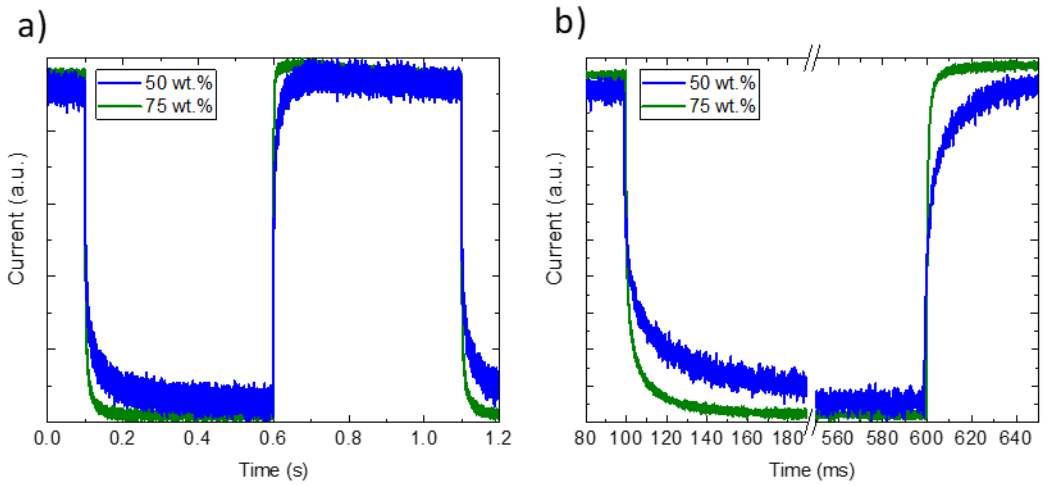

Figure 3.8 Response devices (50 wt.% and 75 wt.% perovskite) when excited by a pulsed laser of 1 Hz and an excitation wavelength of 405 nm. (a) Response of the devices in a time scale where the whole on and off state is visible. (b) Cropped figure of the response of the devices, where the fall and rise response is visualized.

The process presented here allows us to tune the thickness of the disks by simply changing the height of the spacer rings, from tens to hundreds of micrometers. Such thick films can be used to obtain narrowband photodetectors leveraging the process known as charge collection narrowing. In a thick semiconductor, the shorter wavelengths are quantitatively absorbed in the vicinity of the surface, and the photogenerated charges will recombine before reaching the electrodes. On the other hand, low-energy photons close to the bandgap of the semiconductor are absorbed within the volume of the material, hence creating charge carriers closer to the contact which leads to the photocurrent. In this way, it is possible to make a filterless narrow-band photodetector with only one thick absorber layer.[126,127] To test for this effect on our perovskite-polymer composites, a series of devices with increasing disk thickness was prepared, and characterized with illumination from the top of the perovskite composite disk (opposite side as of the ITO electrodes). The specific detectivity spectra of devices with increasing disk thickness are reported in **Figure 3.9**, both in linear and semi-log scales. A narrowband response is observed in all cases, although thinner disks (25 µm) were found to lead to higher specific detectivity. The thicker the disk, the more effective charge collection

narrowing, narrowing, and red-shifted the spectral response peak. However, by increasing the disk thickness, D* was found to decrease accordingly, as fewer low-energy photons can reach the vicinity of the bottom interdigitated ITO contacts. The device with a thickness of 25 µm when illuminated at the perovskite side at a field of 2.5 V/µm has a peak at 555 nm, corresponding to a narrow-band photodetector. The FWHM of the peak is as narrow as 15 nm, which is remarkable for such a simple device layout. The specific detectivity of the narrow-band detectors is in the range of $1 \cdot 10^9$ Jones.

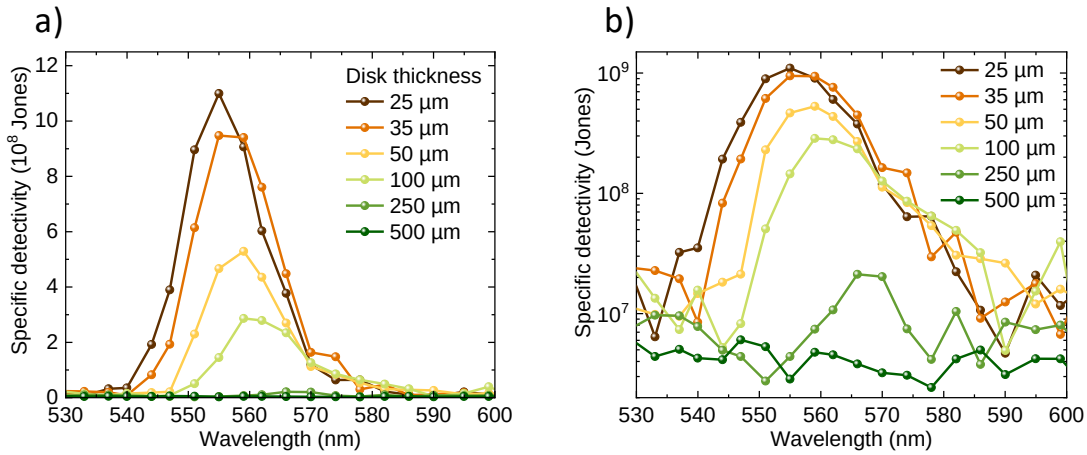

Figure 3.9. Narrowband photodetectors are obtained by illuminating the devices on the opposite side of the ITO electrodes. (a) Specific detectivity of 75 wt.% perovskite devices with different thicknesses, collected at 2.5 V/µm. (b) The same dataset is plotted but represented in a semi-log scale.

3.4. Conclusion

In summary, a dry process to prepare perovskite-polymer composites in ambient air is presented. Mechanochemical synthesized $CsPbBr_3$ powders are mixed with the polymer PBMA and pressed into thin disks with enhanced mechanical properties. The disks can be handled and laminated on interdigitated ITO/glass substrates, obtaining functional photoconductors. Different perovskite/polymer concentrations were evaluated. The composite containing 75 wt.% of perovskite resulted in the highest specific detectivity with a mean value of $2 \cdot 10^{11}$ Jones, at an applied field of 2.5 V/µm. The spectral response of the photoconductors was found to be rather constant over the whole absorption range of the perovskite. Despite the

thick composite film and the large inter-electrode distance (40 µm), a rise time of 1.78 ms is measured for the 75 wt.% devices. Moreover, the thickness of the composite disks can be leveraged to obtain narrow-band detectors, by illuminating the device from the perovskite-polymer material. The peak of the narrow band detector with a thickness of 25 µm is at 555 nm with a very narrow FWHM of 15 nm, and a detectivity of $1 \cdot 10^9$ Jones. Overall, this process shows a simplified route to produce polymer-embedded perovskite photodetectors, processed in air and in the absence of solvents. Due to the fabrication´s simplicity and the process´s flexibility, it can be applied to more complex perovskite systems and applications in real working conditions.

Chapter 4

Polymer-encapsulated halide perovskite ionization detectors

4.1 Introduction

This chapter discusses the application of the disks containing $CsPbBr_3$ and poly(butyl methacrylate) to absorber materials for X-ray detectors. First, the lateral configuration from Chapter 3 was tested under X-ray irradiation, where a stable and reliable response is measured for perovskite-polymer disks with 50 wt.% perovskite content. Then a vertical device configuration is fabricated to utilize the full volume of these 50 wt.% disks, which resulted in a sensitivity as high as 98±2 μC Gy^{-1} cm^{-2} for a device with a 470 μm thick absorber layer. Furthermore, a low detection limit and high irradiation stability were measured. Finally, flexible X-ray detectors are also demonstrated, leading to performance on par with the rigid devices.

4.1.1. X-rays photon energy

X-rays are high-energy electromagnetic photons that originate from the electron cloud of an atom, with energies ranging from 1 keV to 10 MeV and wavelengths ranging from 1 pm to 10 nm. Depending on the energy of the X-ray photon the X-ray is classified as hard X-ray, with an energy greater than 10 keV, or soft X-ray when the energy of the photon is below the hard X-ray value with a minimum of 1 keV. While there is no definition difference, photons with energies above 100 keV are often described as gamma rays. Gamma rays have the same basic properties but the difference between X-rays and gamma rays is the origin of the photons, where X-rays are emitted by the electrons outside the nucleus, the gamma rays are emitted by the excited nucleus itself. Traditionally X-rays were distinguished from gamma rays but this is obsolete with modern X-ray production methods and therefore in further context gamma and X-rays are unified under the name X-rays. Hard X-rays are often used for medical, security, and industry screening applications, whereas soft X-rays can be used for microscope applications (**Figure 4.1**).

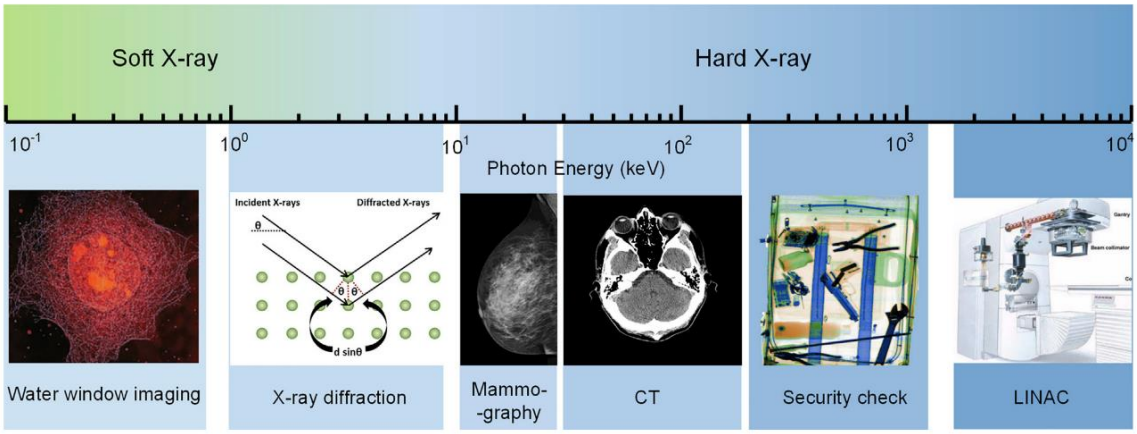

Figure 4.1. The photon energy range of X-rays and the possible applications at different photon energies.[128]

4.1.2. Absorption of X-rays

When an X-ray passes through matter, the probability of absorption is proportional to the thickness of the layer, the density of the material, and the absorption cross-section of the material. X-ray absorption can occur via three processes: photoelectric effect, Compton scattering, and pair production (**Figure 4.2a**).

Photoelectric effect

Here the photon interacts with an atomic electron, causing the ejection of that electron from the atom (the photoelectron). Photoelectric absorption can occur when the incident photon's energy is larger than the binding energy of the shell electron. The kinetic energy of this photoelectron can be described by the energy of the incident photon minus the electron's binding energy to the atom. This photoelectric effect is the dominant interaction mechanism at photon energies of 50 keV and less.

Compton scattering

The same interaction occurs as the photoelectric effect, but where with the photoelectric effect the incident photon energy is fully transferred to the bounded electron, with Compton scattering the incident photon loses sufficient energy to cause the ejection of the electron from the atom and where the residual photon energy is emitted as a new lower energy X-ray photon. This energy X-ray has a new directional path hence the name scattering. This effect is relatively

independent of the atomic number of the absorbing material and is more pronounced in the energy range between 100 keV to 10 MeV.

Pair production

In the case of high-energy photons greater than 1.02 MeV, that is $2m_ec^2$ where m_e is the static mass of the electron and c is the speed of light, the photon can interact with the electric field of the nucleus of the atom.[129] The energy of the incident photon is converted into the mass of an electron-positron pair. Any excess energy of the equivalent rest mass of the two particles appears as the kinetic energy of the pair and in the displacement of the emitting nucleus. The positron will subsequently annihilate after slowing down in the absorbing medium and combines with a free electron where they annihilate and the entire mass is converted into two gamma photons.

Rayleigh scattering

This is an interaction where no absorption has taken place, but for completeness, it would be stated here as well. With Rayleigh scattering an incident X-ray photon can interact with an electron and be scattered with no loss in energy (also known as coherent or elastic scattering). It occurs by temporarily raising the energy of the electron without removing it from the atom. The electron returns to its previous energy level by emitting an X-ray photon of equal energy but in a slightly different direction.

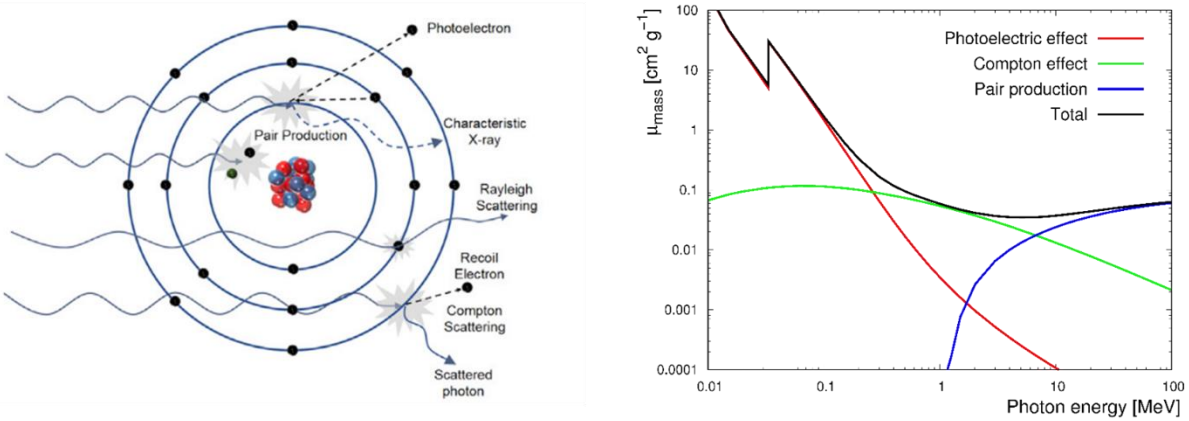

Figure 4.2. (a) Possible interactions of X-rays with an atom.[128] (b) The mass attenuation coefficient as a function of the photon energy, where the influence of the interaction mechanisms at different energies are stated.[130]

4.1.3. Attenuation of X-rays

The total interaction probability for a photon propagating in matter is the sum of the individual interaction probabilities affiliated with the photoelectric, Compton, and pair production interaction mechanisms at a given photon energy (**Figure 4.2b**). Given a mono-energetic beam of photons (I_0) traversing a material of thickness x, the total number of photons transmitted after passing through the material can be formulated in the following way:

$$I = I_0\, e^{-\left(\frac{\mu}{\rho}\right)\rho x} = I_0\, e^{-\mu x} \qquad \text{Equation 4.1.}$$

Where I is the attenuated beam intensity in number of photons, I_0 is the incident beam intensity in number of photons, μ/ρ is the mass attenuation coefficient of the absorber for a specific photon energy given in cm^2/g, μ is the linear absorption coefficient of the absorber for a specific photon energy given in cm^{-1}, x is the absorber thickness in cm, and ρ the density of the traversed material in g/cm^3.

At a given photon energy, the linear attenuation coefficient can vary significantly for the same material if it exhibits differences in physical density, and therefore the mass attenuation coefficient is often used to compare materials which compensates for these variations by normalizing the linear attenuation by the density of the material.

The mass attenuation coefficient relies heavily on theoretical values for the total cross section per atom, which is related to μ/ρ according to:

$$\frac{\mu}{\rho} = \sigma_{tot} u / A_m \qquad \text{Equation 4.2.}$$

Where u is the atomic mass, A_m is the relative atomic mass of the target element, and σ_{tot} is the total cross-section for interaction by the photon, frequently given in units of barns/atom.

Therefore, every atom has its mass attenuation coefficient, but the attenuation coefficients for compounds can be easily determined as the weighted average (by mass) of the individual mass attenuation coefficients of the compound's constituent elements:

$$\frac{\mu}{\rho} = \sum_i (\mu/\rho)_i \qquad \text{Equation 4.3.}$$

4.1.4. X-ray detectors

X-ray detectors are widely used for medical imaging, non-destructive industrial inspections, scientific research, and safety screening.[131,132] The detectors are used to characterize properties of X-rays like the dose, spatial distribution, spectrum, and other properties. The working principle is again based on the formation of electron-hole pairs when incident high-energy photons are traversing a semiconductor material. When photoelectric, Compton, and pair production interaction mechanisms take place in the absorber material, the high-energy secondary electrons (and/or positrons) produced by the incident photons pass through the semiconductor and release many low-energy free electrons through ionization. These free electrons move to the conduction band and leave behind holes in the valence band, generating electron-hole pairs that can be recombined to emit light (indirect detection) or collected under an electric field (direct detection).[133,134] Here the focus is on direct solid-state detectors, where X-ray photons are directly converted to electrical charge by a semiconducting material. First, important characteristics of the absorber material are explained and second important device parameters for X-ray detectors are specified.

4.1.4.1. Important characteristics absorber material

Stopping power

A large stopping ability of a material is needed to effectively absorb the X-ray photons with smaller thicknesses of the absorber material. As a figure of merit, the mass attenuation coefficient can be used to compare different materials with each other.

Mobility lifetime product

This is often used to characterize the carrier properties, which indicate a semiconductor's capability of extracting charge from the bulk. Especially in the case of X-ray detectors where thick absorber layers are needed for completely absorbing high energy X-ray photons this figure of merit is of importance. While the mobility lifetime product is mostly dependent on the semi-conducting material properties, it can be enhanced by applying a higher applied bias to improve the carrier drift length to fill the criteria. However, this induces higher dark currents that decrease the detection accuracy of devices.

Resistivity

As stated above, a low dark current is desired to increase the detection accuracy of the devices. Therefore, the resistivity, which evaluates the conductivity of a (semi-)conductor is of importance. Large bulk resistivity contributes to a small dark current and low noise for radiation detector

Ionization energy

The ionization energy ($W_{\pm}$), is the average energy utilized by the primary X-ray photon to produce one electron-hole pair and relates closely to the sensitivity of the detector. An empirical relationship between the ionization energy and the bandgap energy (E_G) provided by the Klein rule is commonly used stated in equation 4.4.[135]

$$W_{\pm} \sim 3E_G \qquad \text{Equation 4.4.}$$

And determines the photo-generated charges as the following:

$$Q = \frac{E_{X-ray}}{W_{\pm}} \qquad \text{Equation 4.5.}$$

where Q represents the carriers generated by the X-ray, and E_{X-ray} the X-ray energy. According to these formulas, a low $W_{\pm}$ is desired and therefore a low-bandgap semiconductor. However, when the bandgap is too narrow the thermal equilibrium concentration of carriers is high which results in a poor dark current. Vice versa, a large bandgap induces low thermal noise but results in a small number of generated carriers. Therefore, a suitable bandgap is desired which improves the sharpness of the image (low-dark current) and can generate more carriers to increase the sensitivity. Typically, the suitable bandgap for X-ray detectors is between 1.35-2.55 eV when operating at room temperature.[136]

4.1.4.2. Figures of Merit

Sensitivity

Sensitivity, defined as the collected charge per unit area under the exposure of radiation, is one of the most essential parameters for X-ray detectors. Especially for medical applications a higher sensitivity lowers the exposure time of the human body under radiation. The operative

definition of sensitivity can be obtained by taking the linear dependence of the X-ray photocurrent signal $\Delta I = I_{X-ray} - I_{dark}$ as a function of impinging dose rate (DR):

$$S = \frac{1}{A}\frac{\partial(I_{X-ray} - I_{dark})}{\partial DR} \quad \text{Equation 4.6.}$$

Where I_{X-ray} and I_{dark} are the photocurrents and the dark current, respectively, while DR is the X-ray dose rate, and A is the effective detection area.

Signal-to-Noise-Ratio and Limit of Detection

The signal-to-noise ratio (SNR) is an important parameter that determines the lowest detectable dose rate which is of importance for the possible potential application. The International Union of Pure and Applied Chemistry (IUPAC) defines the detection limit as the equivalent dose that generates a signal three times greater than the noise (SNR = 3).[137] To calculate the SNR first, the net signal current density is calculated by subtracting the photocurrent density from the dark current density:

$$J_{net} = J_{X-ray} - J_{dark} \quad \text{Equation 4.7.}$$

Then the noise current density can be calculated by taking the standard deviation of the dark current density:

$$J_{noise} = \sqrt{\frac{1}{N}\sum_{i}^{N}(J_i - J_{dark})^2} \quad \text{Equation 4.8.}$$

Then the SNR can be calculated by dividing the net current density by the noise current density:

$$SNR = \frac{J_{net}}{J_{noise}} \quad \text{Equation 4.9.}$$

Response speed

The response speed, defined as the time taken to respond to an external stimulus, is significant in X-ray detectors because a faster response speed can shorten the exposure time, and enable a higher frame rate during imaging. The response speed is defined similarly to the response speed in Chapter 3.

4.1.5. Motivation and Aim

Traditional semiconductors that are used for direct X-ray detectors nowadays like amorphous silicon, germanium, cadmium telluride, and cadmium zinc telluride have impressive performances. However, there are some limitations regarding these semiconductors, which are the difficulties in obtaining larger areas, the intrinsic stiffness of the materials which limits flexible detectors, costly fabrication processes to obtain high-quality materials, and the materials are heavy.[138] Therefore, a new material without these issues would be highly desirable. Halide perovskites, as discussed earlier, have a large carrier mobility-lifetime product, consist of relatively lightweight materials, and low-cost synthesis processes are possible. Furthermore, due to the inclusion of heavy atoms (i.e. caesium, lead, iodide), the atomic number of perovskites can be high, and therefore the X-ray attenuation coefficient as well. This makes perovskites a very interesting material for X-ray detection.[128,139,140]

Common ways to prepare perovskite solids for X-ray detectors are, dissolution and recrystallization, spray deposition process, scraper method, melt and crystallization, thermal evaporation, and spin-coating processes.[6,7] All these processes have shown some remarkable signs of progress in the past few years, however, there are still some important obstacles to overcome. First of all, the stability of perovskite materials is still relatively poor. Second, for perovskite X-ray detectors the thickness of the absorber material should be at least hundreds of micrometers for complete or sufficient absorption. The above-described processes have difficulties in making uniform thick films and the cost of most processes is high. Therefore, development in process techniques for thick perovskites is needed.[128,139,140] At last, most research has not focused on flexible large-area perovskite-based X-ray detectors. Currently, the highest-performing perovskite-based X-ray detectors are rigid, which limits the applications.

Motivated by their photoconductive properties with wavelengths in the visible range of the polymer-perovskite disks from the previous chapter, the disks are characterized as possible absorber material for X-ray detectors. As mentioned earlier, the preparation method allows to production of thick disks with ease, which makes them also interesting as active materials for the detection of ionizing radiation. Furthermore, the disks are flexible which could produce flexible X-ray detectors.

4.2. Synthesis and Characterization

4.2.1. Synthesis

For the first experiments, the same lateral photoconductors introduced in Chapter 3 are used. New vertical devices are also produced by laminating the $CsPbBr_3$-PBMA disks on a glass substrate with an ITO layout or, to produce flexible devices, on a polyethylene terephthalate (PET) substrate with the same ITO layout. The disks can be simply cut by scissors to obtain the desired shape if needed. Once the disks are laminated on the substrate, 300 nm thick copper contacts are thermally evaporated on top of the disks, resulting in a vertical device structure with 8 contacts of 0.0825 cm^2 (**Figure 4.3**). An extra conductive copper tape can be used to ensure metal contact at the edge of the disks when great thicknesses of the disk are used. Additionally, the vertical photoconductors are encapsulated with an aluminum oxide (Al_2O_3) layer of 20 nm by atomic layer deposition.

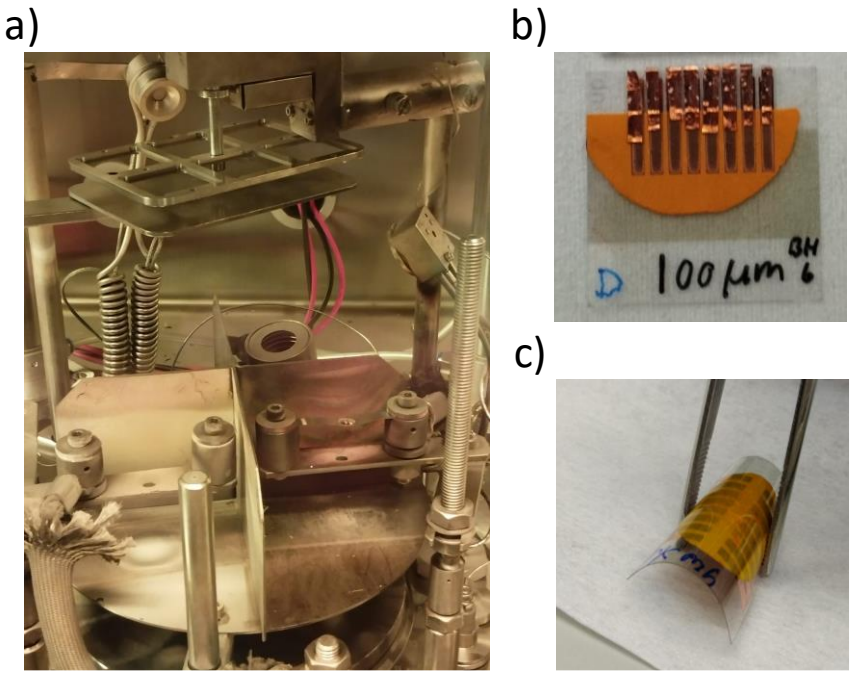

Figure 4.3 (a) Inside of a metal evaporator. (b) Vertical photoconductor with copper tape at the edges to ensure contact with the evaporated copper on top of the disk. (c) Flexible X-ray detector.

4.2.2. Characterization

X-ray characterization

The X-ray source consists of a Hamamatsu L12161 Microfocus X-ray tube with a W target operated at an accelerating voltage of 150 kVp for the lateral photoconductors and 40 kVp for the vertical photoconductors. The filament currents could be adjusted in the range from 10 to 500 μA. The photocurrent was acquired using a Keithley 2614B Precision Source/Measure Unit. For the lateral photoconductors the irradiation measurements were held in a nitrogen atmosphere (glovebox), while for the vertical photoconductors, the devices were measured in air.

4.3. Results and Discussion

Initially, the lateral photoconductors with different weight percentages of $CsPbBr_3$ in PBMA produced in Chapter 3 are tested on their ability to convert X-rays to an electronic signal. Hence, the devices were tested under irradiation with 150 kVp photons at different doses. The optimal bias for the device is identified by looking at the current on/off ratio at different applied voltages, at a dose of 1480 μG/s. The on/off ratio is maximized at an applied field of 0.5 V/μm (20 V), and it does not increase further for higher voltages. To determine the linearity of the devices and their sensitivity, the devices were irradiated at different dose rates and the output signal was measured. However, for the devices with disks at 75 wt.% perovskite content, the current was observed to drift substantially during the measurements, hindering a reliable characterization. Furthermore, the devices with disks at 90 wt.% perovskite content showed a low yield as reported in the previous chapter. For the 50 wt.% of $CsPbBr_3$, the device output signal was found to be stable over time, with a fast and linear response to different X-ray doses (**Figure 4.4a-b**). A reliable sensitivity could be measured for these disks which have a sensitivity of around 1 μC Gy^{-1}. For the 50 wt.% perovskite disks, additional measurements with lower doses are performed to obtain the limit of detection, which was found to be 3 ± 1.1 μG/s (**Figure 4.4c-d**). It is worth noting that both the device sensitivity and limit of detection are likely limited by the charge diffusion length in the perovskite/polymer composite, as in the lateral device configuration used here not the full volume of the disks contributes to the photocurrent. Indeed, among the ≈1.8% absorbed radiation in a 100 μm thick perovskite

polymer composite, the majority is absorbed far from the bottom electrodes. Overall, the results of the 50 wt.% perovskite content disks show promising properties for their use as X-ray absorber materials.

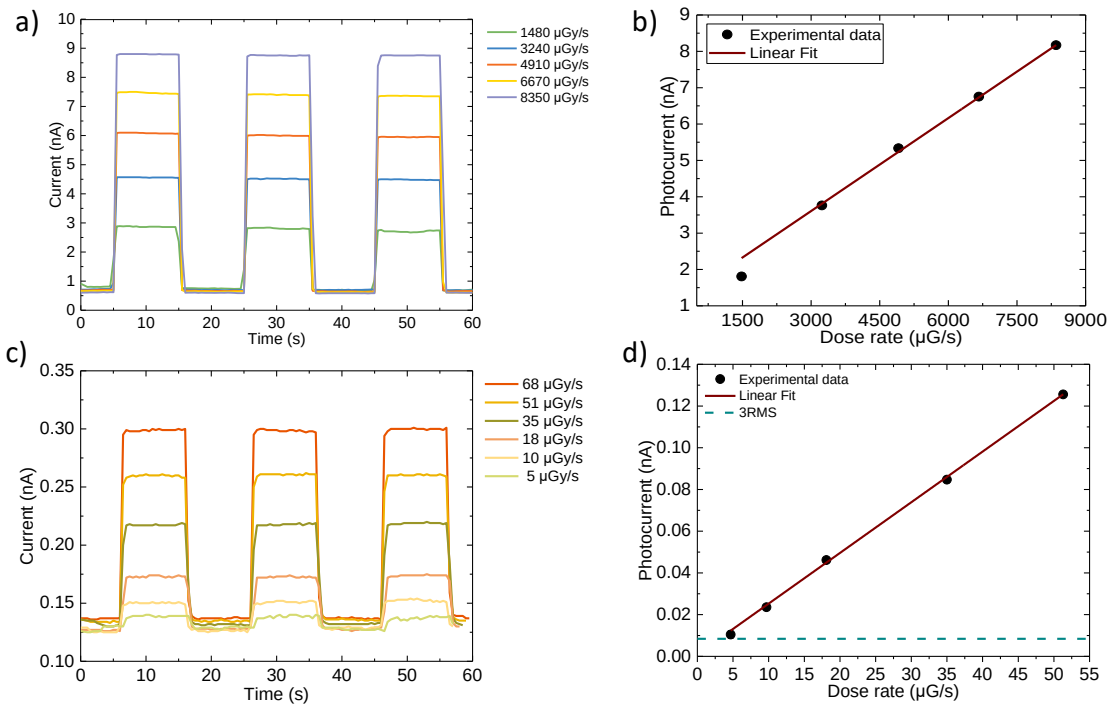

Figure 4.4. (a) Response of a 50 wt.% perovskite content device when exposed to pulsed 150 kpV photons at different doses. (b) Photocurrent versus dose rate of the results in Figure 4.4a, where a linear fit is applied. (c) Response of a 50 wt.% perovskite content device when exposed to pulsed 150keV photons at low doses. (d) Photocurrent versus dose rate of the results in Figure 4.4c, where a linear fit is applied and the 3RMS is calculated with a value of 8.43 pA.

Due to the promising results of the 50 wt.% perovskite-polymer disks in lateral configuration further experiments are conducted on this composition. As discussed above, the lateral device configuration possibly hinders the sensitivity and the limit of detection of the final device, therefore, a vertical design will be highly desirable. Hence, a vertical configuration is produced by applying copper contacts on top of the disk which is laminated on a substrate covered by ITO, forming a vertical ITO/perovskite-polymer/copper configuration. An extra alumina encapsulation layer is applied to cover the copper contacts to minimize the interaction of the copper contacts with the ambient environment. To confirm if the vertical designs are operating, first, the photoconductive properties are measured for wavelengths in the visible range,

resulting in a responsivity of ±0.4 A/W, dark current of ±1.4 $\cdot 10^{-4}$ mA/cm^{2,} and a specific detectivity around ±2 $\cdot 10^{11}$ Jones for an absorber thickness of 47 µm, showing working devices with this vertical design.

Now X-ray detectors with this vertical design are produced with different absorber thicknesses of 47, 100, 270, and 470 µm. To determine the linearity of the devices and their sensitivity, the devices were irradiated at different dose rates and the output signal was measured. All the vertical devices show linear response using the different dose rates of 408, 842, 1275, 1711, and 2139 µGy/s (**Figure 4.5a)**. To compare the sensitivity versus thickness of the absorber material, the same applied field of 4255 V/cm is used for the devices with different thicknesses. At this applied field, the devices with 100, 270, and 470 µm absorber thickness have a sensitivity of 56±2, 69.4±1.5, and 98±2 µC Gy^{-1} cm^{-2}, respectively. The device with a thickness of 47 µm faced strong instabilities in the current at this applied field, and therefore a lower applied field of 435 V/cm was used, resulting in a sensitivity of 3.6±0.2 µC Gy^{-1} cm^{-2}.

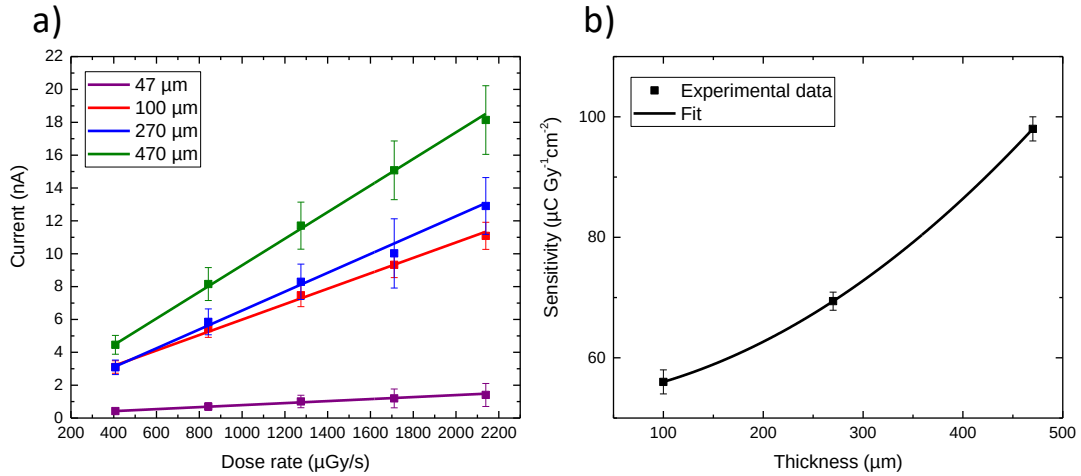

Figure 4.5. (a) Linear response of the photocurrent for devices with different thicknesses at different dose rates. For the 100, 270, and 470 µm thick devices, an applied field of 4255 V/cm was used, whereas an applied field of 435 V/cm was employed for the 47 µm thick device (b) Sensitivity versus thickness at a fixed applied bias of 4255 V/cm.

In **Figure 4.5b** the sensitivity of the devices versus the thickness of the absorber is visualized when the same applied field of 4255 V/cm is used. Although there are only three different thicknesses due to the instabilities of the thinnest device at this electric field, it is visible that the sensitivity increases with greater thickness, but the trend does not follow Beer Lambert's

law which **equation 4.1** suggests. Utilizing **equation 4.2-4.3** the absorption coefficient for the 50 wt.%, perovskite in PBMA can be calculated, as depicted in **Figure 4.6**. For a 40 kpV X-ray source, the absorption efficiency of the polymer-perovskite disks increases from 7.1 to 52.2% when increasing the thickness of the polymer-perovskite blend from 47 to 470 µm. However, this trend is not observed in **Figure 4.5b** and this is likely related to the increase of charge trapping in thicker films which is often observed with perovskite X-ray detectors.[141]

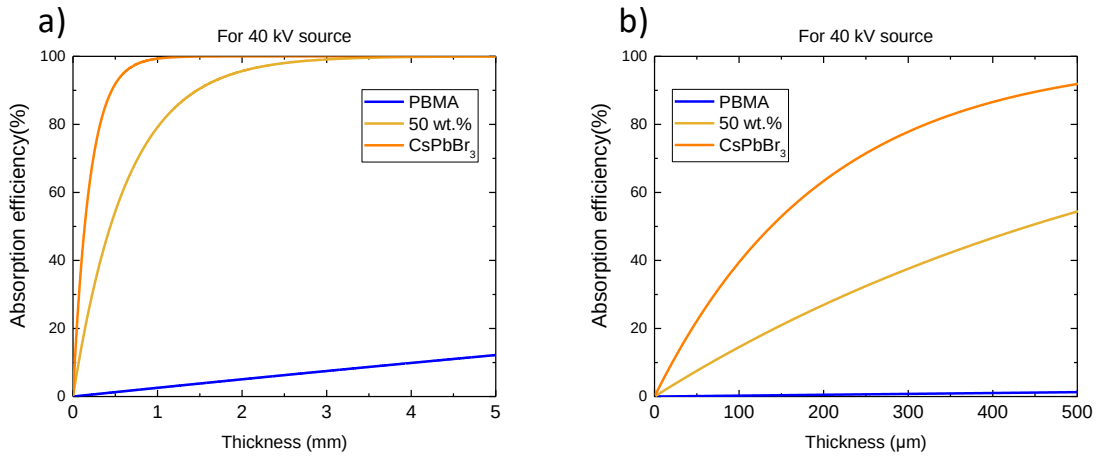

Figure 4.6. Theoretical absorption efficiency of $CsPbBr_3$, 50 wt.% $CsPbBr_3$ in PBMA and, PBMA only for 40 kpV X-rays. (a) Absorption efficiencies of all three materials. (b) Zoomed-in absorption efficiency of 50 wt.% $CsPbBr_3$ in PBMA.

For the device with a 470 µm thick absorber layer, the limit of detection and the device stability were assessed. First, the limit of detection was studied at a field of 106 V/cm, where the photocurrent versus dark current ratio was the lowest. At this applied field, the LoD was determined to be as low or lower than 46±2 nG/s (**Figure 4.7**). The LoD could be even lower than this value, but with this setup, lower signals could not be resolved.

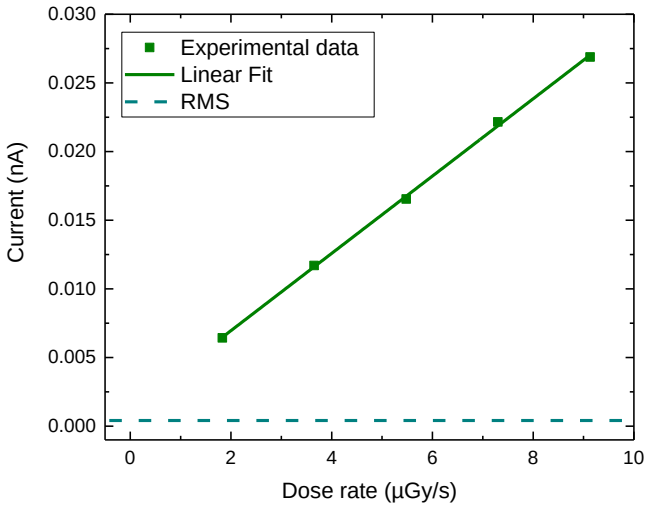

Figure 4.7. Limit of detection measurement with an applied field of 106 V/cm with an RMS of 0.408 pA.

To test the stability of the 470 µm thick device, the device is exposed to pulsed irradiation for 20 minutes at an applied bias of 4255 V/cm. After 1200 cycles no deviation in the signal is observed, indicating excellent stability of the device under irradiation (**Figure 4.8**).

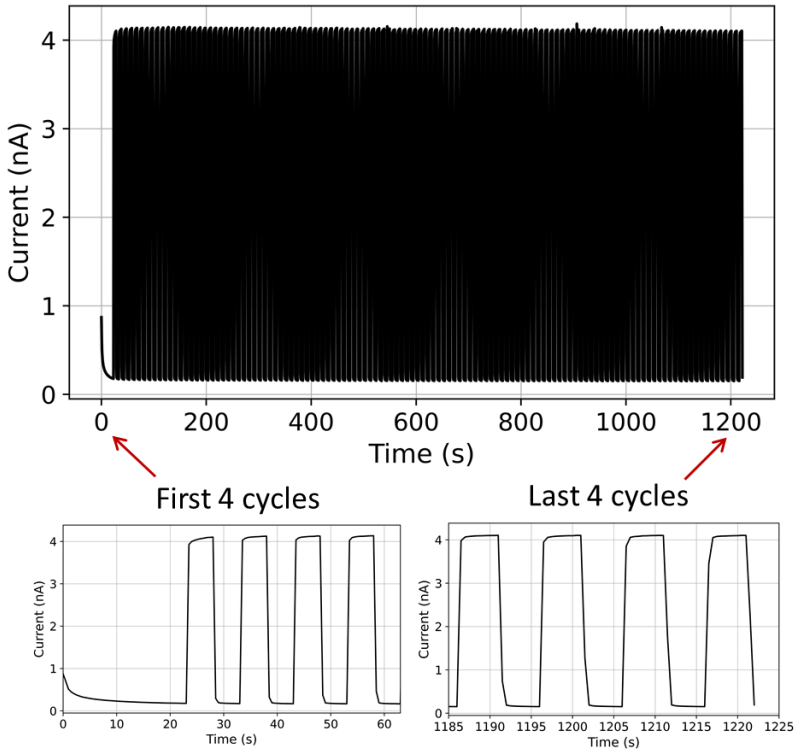

Figure 4.8. Stability over time for a 470 µm thick device at an applied field of 4255 V/cm. A pulsed X-ray source is applied with an on/off period of 5 seconds for 20 minutes with source settings of 40 kpV source at 100 µA.

As shown in the previous chapter, the disks are flexible, and therefore flexible detectors could be fabricated (**Figure 4.3c**). Flexible detectors are produced by utilizing 47 and 100 µm thick disks which are laminated on a flexible PET substrate followed by evaporation of copper contacts. Greater thicknesses of the disks were not possible to apply due to delamination of the disk with the PET substrate. However, for both the 47 and 100 µm thick flexible devices, a linear photocurrent versus doses is measured (**Figure 4.9a**). Furthermore, comparing the sensitivities of the flexible PET devices with the rigid detectors, the values are almost similar for the same electric field, showing the potential for obtaining flexible X-ray detectors of this simple fabrication process (**Figure 4.9b**).

a) PET substrates

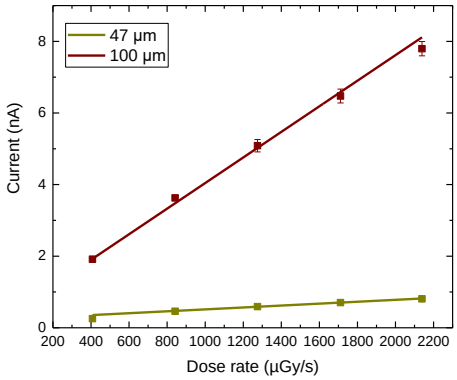

b)

Device	Electric field (V/cm)	Areal sensitivity (µC Gy-1 cm-2)
Glass (46µm)	435	3.6±0.2
GLass (100µm)	4255	56±2
PET (46µm)	435	3.7±0.3
PET (100µm)	4255	40.8±1.1

Figure 4.9. (a) Linear response of the photocurrent versus different dose rates for flexible devices with 47 µm thickness and an electric field of 435 V/cm, and with 100 µm thickness and an electric field of 4255 V/cm. (b) Table for comparison areal sensitivity rigid devices (glass substrate) versus flexible devices (PET substrates).

4.4. Conclusion

In summary, from the different weight percentages of $CsPbBr_3$ in PBMA studied, the 50 wt.% $CsPbBr_3$ in PBMA disks were considered the most promising absorber material for ionization detectors since they exhibit a stable and reliable response. To use the full volume of the absorber material, vertical devices were produced with different absorber material thicknesses. The sensitivity versus thicknesses at the same applied electric field did not follow Beer Lambert's law which is likely due to the increase in trap states with increasing thickness of the absorber material. However, the sensitivity of the vertical designs increased with thickness up to a maximum sensitivity of 98±2 µC Gy^{-1} cm^{-2} for the 470 µm thick absorber layer. The same device had a very low LoD of at least 46±2 nG/s and excellent stability under pulsed irradiation for 20 minutes. At last, flexible X-ray detectors were performed with a maximum thickness of 100 µm, showing almost the same response as the rigid substrates. Overall, this simple dry fabrication process shows promising results in producing rigid and flexible X-ray detectors with ease.

Chapter 5

General Conclusions

This thesis presents a new and simple preparation method to obtain functional materials and devices starting from perovskite powders. The results collected in the thesis demonstrate the potential of this approach in applications such as photon conversions and photon detection.

In Chapter 2, the development of the solvent-free processing method to convert perovskite powders produced by mechanochemical synthesis in a functional layer is reported. Thermoplastic polymers are blended with the perovskite powders and pressed into disks by hot-pressing in ambient air. Thanks to the use of thermoplastic polymers, a mechanically stable disk can be obtained by pressing the powder above the polymer glass transition temperature and within the thermal stability window of the perovskite. With this method, color converters based on highly luminescent particles of $MAPbBr_3$ dispersed in transparent polymers such as PMMA, PEO, and PS, are obtained. The color quality for the PMMA and PS-based color converters is high, with a narrow emission spectrum having a full width at half maximum of less than 25 nm. Furthermore, the color converters are stable for over two months at an elevated temperature of 85 °C. As a proof of concept, a multiple-color converter is prepared by inserting an additional fluorophore in the disks. This chapter shows that the processing method is highly versatile, does not require harmful solvents, and can be used to prepare color converters with good stability and high optical quality.

Chapter 3, extends the research on the polymer-perovskite disks, synthesized by the same method as in the former chapter, by utilizing them as absorber material for visible photoconductors. To obtain a functional device, the composite disks are adhered to a pre-patterned electrode by hot-roll lamination, preserving the simple and dry nature of the processing method. To ensure a robust and electrical connection between the substrate and the disk, the polymer PBMA was blended with the perovskite material, as it is mechanically stable, with good adhesion properties and low parasitic absorption. The PBMA was mixed with the perovskite $CsPbBr_3$ in different ratios, which were then tested on their photoconductive performances, resulting in the best properties for 75 wt.% of $CsPbBr_3$ in PBMA with a specific detectivity above 10^{11} Jones. Since the process allows to prepare thick disks, filterless narrowband detectors can be achieved by illuminating the device from the perovskite side, obtaining narrowband spectral response with a FWHM down to 15 nm. This chapter reveals that the perovskite-polymer composites can be easily laminated on substrates with thickness control of the disks, obtaining functional optoelectronic devices that can be used as sensitive photodetectors.

Finally, in Chapter 4, the same polymer-perovskite disks are used as ionizing radiation detectors. Since the synthesis method allows to obtain very thick disks, they can be used as absorber material of X-ray photons. First, the lateral configuration of Chapter 3 is used to observe the influence of different perovskite polymer ratios. The best results were achieved with a 50 wt.% perovskite in polymer which resulted in a linear and fast response to X-rays, with a detection limit of 3 µG/s. However, in the lateral configuration, most charge carriers are produced far from the contact and are hence lost due to recombination within the bulk of the material. For this reason, vertical device structures are fabricated by sandwiching the disks between ITO and copper contacts. These devices can use the full volume of the absorber material, resulting in a sensitivity of 98±2 µC Gy^{-1} cm^{-2} for a 470 µm thick absorber layer with a LoD at least as low as 46±2 nG/s and with good stability under irradiation. Lastly, flexible devices are produced using a PET substrate instead of glass resulting in the same sensitivity as the rigid X-ray detectors. This chapter shows that stable rigid and flexible vertical ionization detectors can be realized using perovskite-polymer composites.

In general, a methodology is developed to process these perovskite powders into functional devices. The approach is versatile and simple, solvent-free, allows for thickness control, and simple adhesion on substrates. In view of these advantages, this method can be easily adopted by other researchers working in this field, but also by the industry, expanding the implementation of perovskite powders by mechanochemical synthesis to functional applications.

Chapter 6

Spanish Summary/Resumen en Español

Capítulo 1: Introducción

1.1. El origen de las perovskitas de haluros metálicos

El término "perovskita" fue utilizado por primera vez en 1839 por el geólogo Gustav Rose quien, en honor al mineralogista ruso Perovski, lo utilizó para dar nombre al mineral CaTiO3 que él mismo descubrió en ese mismo año.[1] En 1926 Goldschmidt también utilizó este término en su investigación sobre el factor de tolerancia para referirse al mismo grupo de cristales.[2] A partir de ese momento, el término perovskita empezó a adoptarse comúnmente en química y mineralogía.

Las perovskitas son un tipo de cristal que presenta la fórmula general de ABX_3. Debido a esta estructura tan simple y general, un gran número de compuestos pueden considerarse perovskitas. Aunque las perovskitas más comunes son los óxidos, esta tesis se centra en un subgrupo específico, denominado perovskitas de haluro metálico (que de aquí en adelante se denominará simplemente perovskitas). En la última década, las perovskitas han sido objeto de intensa investigación debido a sus prometedoras propiedades optoelectrónicas, como la alta absorbancia óptica, las largas longitudes de difusión electrón-hueco, la banda prohibida directa y de valor fácilmente modificable y la fotoluminiscencia de banda muy estrecha.[5,6] La posibilidad de controlar las propiedades de la perovskita mediante sustitución de sus componentes A, B o X, ha hecho que las posibles aplicaciones de estos materiales se hayan multiplicado notablemente.

1.2. Síntesis mecanoquímica de perovskitas

En 2013, Stoumpos et al. demostraron que es posible sintetizar diferentes perovskitas síntesis mecanoquímica.[25] La mecanoquímica se refiere a la rama de la química en la que la activación de las reacciones químicas se origina a partir de energía mecánica que puede surgir, por ejemplo, por impacto, compresión o tensión. En la síntesis mecanoquímica, los precursores secos se añaden juntos en la proporción estequiométrica deseada y, al molerlos, los materiales precursores reaccionan formando otro compuesto.

Este sencillo método se puede llevar a cabo moliendo a mano con un mortero, pero para conseguir que el material precursor reaccione por completo y de manera más homogénea, es preferible utilizar un molino de bolas eléctrico, donde los materiales se muelen por impacto de unas bolas de molienda dentro de un recipiente cerrado. Los precursores se introducen en el recipiente del molino y al ponerlo en movimiento (movimiento lineal o de rotación), la energía mecánica del medio de molienda se traslada a la mezcla de reacción para formar el producto. Los parámetros que pueden ajustarse durante la molienda por bolas son el tiempo de molienda, la frecuencia de rotación o agitación y la relación entre el peso de la bola y el del material en polvo. Además, los tarros pueden sellarse y, por tanto, el proceso puede realizarse en cualquier entorno deseado, como por ejemplo en atmósfera inerte.

Debido a la simplicidad de la síntesis mecanoquímica, esta técnica sin disolventes no tiene limitaciones en cuanto a composición o estequiometría, y puede usarse para la preparación de materiales de perovskita de gran pureza. Por ejemplo, se ha demostrado que puede usarse para la síntesis cuantitativa de perovskitas de haluro de plomo 3D, con una pureza de fase excelente. Además es posible añadir aditivos, formar fases mixtas, producir perovskitas sin plomo y crear diferentes estructuras de perovskita (2D, quasi-2D).[26] Por último, esta técnica ya se utiliza en la industria farmacéutica, por lo que es fácilmente escalable. Las desventajas de esta técnica se limitan a la distribución no homogénea del tamaño de las partículas y a la posible contaminación por desgaste abrasivo de las bolas y del recipiente.

1.3. Objetivo de la tesis

Esta tesis pretende desarrollar una novedosa ruta para convertir polvos de perovskita, preparados en seco mediante síntesis mecanoquímica, en sólidos con dimensiones y propiedades mecánicas adecuadas para aplicaciones ópticas y optoelectrónicas. En particular, la atención se centra en la conversión y en la detección de fotones.

Para lograr el objetivo general de la tesis, se ha desarrollado una ruta sintética en seco para la preparación de polvos de perovskita, que se detalla en el capítulo 2 y se utiliza a lo largo de toda la tesis. El método se basa en la síntesis mecanoquímica de perovskitas, la preparación de compuestos polímero-perovskita y su transformación en discos delgados estables mediante prensado en caliente. Como primera prueba de concepto, estos materiales se aplican a convertidores de color de alta calidad con una elevada eficiencia de luminiscencia y una

prometedora estabilidad, que se consigue con una formulación de perovskita relativamente poco estable térmicamente.

Para ampliar la gama de aplicaciones de los discos de perovskita-polímero, es imprescindible crear contactos eléctricos, lo que permitiría preparar dispositivos optoelectrónicos. Este es el objetivo del Capítulo 3, donde se desarrolla un método de laminación simple para fabricar fotoconductores laterales con los discos de polímero-perovskita como materiales absorbentes. Se presenta la metodología para la fabricación y optimización de fotoconductores laterales, realizando tanto detectores de banda ancha como de banda estrecha procesados en condiciones suaves sin el uso de disolventes.

En los dispositivos laterales, la región activa de un semiconductor está limitada por la separación entre electrodos y por la longitud de difusión de la carga en la dirección normal. Para ampliar esta región y utilizar todo el volumen del disco, deben prepararse dispositivos verticales con contactos a ambos lados del material. En el capítulo 4 se describe un proceso para obtener dispositivos verticales a partir de compuestos polímero-perovskita. Como el grosor de los discos puede ajustarse fácilmente de decenas a cientos de micrómetros, estos dispositivos tienen potencial para la detección directa de rayos X, que es la principal aplicación a la que se dirige este capítulo. Estos dispositivos serían de especial relevancia para aplicaciones en dosimetría para la seguridad médica.

Capítulo 2: Convertidores de color de perovskita de haluros encapsulados en polímeros

2.1. Motivación y objetivo

Las perovskitas de haluros metálicos son óptimas candidatas para desempeñar la función de emisores fluorescentes, ya que pueden tener una eficiencia cuántica de luminiscencia (PLQY, del inglés *photoluminescence quantum yield*) elevada y un pico de emisión con anchura a media altura (FWHM, del inglés *full width at half maximum*) muy estrecha (< 30 nm), lo que conlleva una alta pureza de color. Además, la longitud de onda de emisión puede ajustarse mediante simples cambios en la composición de la perovskita. Asimismo, las perovskitas tienen un alto coeficiente de absorción y los precursores químicos empleados son de bajo coste.[47–53] Estas propiedades únicas hacen de las perovskitas de haluro un material de gran interés para su comercialización en pantallas y sistemas de iluminación.[54,55]

Las perovskitas de haluro metálico se preparan generalmente mediante procesos en disolución. Debido a las diferentes solubilidades de las sales precursoras y de eventuales aditivos, no siempre es trivial controlar de forma reproducible la composición final (y, por tanto, las propiedades ópticas) de estas perovskitas.[56] Además, también se ha observado que los disolventes residuales afectan a la estabilidad y las propiedades ópticas de las mismas.[57,58]

La síntesis mecanoquímica es un método alternativo para la preparación de materiales de perovskita altamente luminiscentes que no implica el uso de disolventes.[59–62] Este método ha demostrado brindar la capacidad de ajustar fácilmente la composición o introducir aditivos en el sistema sin dificultades adicionales relacionadas, por ejemplo, con la solubilidad.[63–65] Es un método reproducible y tiene una gran versatilidad de cara a la composición final, lo que lo convierte en una ruta deseable para preparar materiales funcionales. En este capítulo el objetivo es producir convertidores de color (fósforos luminiscentes) estables y de alto rendimiento, a partir de polvo de perovskita mediante síntesis mecanoquímica.

2.2. Detalles experimentales

La perovskita se sintetiza mediante síntesis mecanoquímica, en la que se utiliza un molino de bolas lineal MM-400 de Retsch, accionado eléctricamente, con recipientes de circonio con un volumen de 10 mL y 2 perlas de circonio de 10 mm de diámetro. La frecuencia del movimiento lineal es variable, pero en este caso se mantuvo constante en 30 Hz. Para obtener convertidores de color de alto rendimiento, el polvo de perovskita inicial debe tener un PLQY elevado. En un trabajo anterior de nuestro grupo, se obtuvieron polvos de perovskita $MAPbBr_3$ altamente luminiscentes mediante síntesis mecanoquímica introduciendo clorhidrato de amantadina (AmCl) en la mezcla de reactivos. Ajustando la cantidad estequiométrica de AmCl con respecto a los precursores de bromuro de plomo(II) y bromuro de metilamonio, se consiguió un PLQY de hasta el 29% para $MAPbBr_3$+50%AmCl.[65] Por ello, en este trabajo, se usa la formulación de perovskita $MAPbBr_3$+50%AmCl. Para la síntesis, se emplea 1 mmol de MABr, 1 mmol de $PbBr_2$ y 0,5 mmol de AmCl y se muele la mezcla a una frecuencia de 30 Hz.

Tras la formación de los polvos de perovskita, se añade un polímero para modificar las propiedades mecánicas del material. Se evaluó el efecto de tres polímeros termoplásticos comúnmente disponibles: PMMA, PS y PEO. Estos polímeros fueron seleccionados por su transparencia y por ser materiales de uso común en la pasivación o encapsulación de perovskitas.[74–79] Para garantizar una mezcla completa entre el polvo de perovskita luminiscente previamente preparado y el polímero, ambos fueron molidos durante 3 minutos más.

La adición del polímero a la perovskita permite moldear el composite en discos finos a una presión y temperatura relativamente bajas. Como molde y calefactor se utilizan la prensa de espesor constante Atlas y los discos calentadores de la serie Atlas de Specac. Esta configuración está diseñada para producir discos redondos de hasta 2,9 cm de diámetro con un grosor ajustable mediante la introducción de diferentes anillos espaciadores entre el molde inferior y el superior. Por lo tanto, con esta configuración se pueden producir espesores de 15, 25, 50, 100, 150 y 500 µm. Se puede aplicar una presión máxima de 4 toneladas métricas, pero en esta tesis no se aplican más de 2 toneladas métricas. Para no dañar el molde pulido, la temperatura del molde se ajusta para que esté por encima de la temperatura de transición vítrea del polímero utilizado. Además, entre la superficie inferior y superior del molde se utilizan láminas de aluminio para evitar que la mezcla de polvo se pegue al molde. Un tiempo de

prensado de 1 segundo es suficiente para producir un disco compuesto de polímero-perovskita. En este capítulo los discos se obtienen con una presión de 1.5 toneladas métricas. La temperatura del molde se fijó en 70 °C para los polvos compuestos que contienen PEO y en 130 °C para los polvos compuestos que contienen PMMA y PS. Para definir el grosor final de los discos prensados se utiliza un anillo espaciador con un grosor de 25 µm, lo que da como resultado discos con un grosor de entre 25 y 30 µm.

2.3. Resultados y discusión

En este trabajo se añaden satisfactoriamente algunos polímeros bien conocidos a una formulación de perovskita $MAPbBr_3$ luminiscente sintetizada mecanoquímicamente. El PMMA y el PS son compatibles con la perovskita y mejoran sus propiedades luminiscentes alcanzando PLQYs superiores al 50%. La incorporación de PEO en el polvo de perovskita da lugar a una reacción con el volumen de la perovskita que conduce a una reducción parcial del PLQY. Como los composites de polímero-perovskita luminiscentes no tienen un factor de forma compatible con la mayoría de las aplicaciones, se convierten en discos delgados mediante prensado (this I don't really understand what you mean). Sorprendentemente, aplicando temperaturas y presiones moderadas, es posible prensar los polvos en discos delgados manteniendo las propiedades luminiscentes y al mismo tiempo mejorando la estabilidad. Por tanto, la presencia de PMMA y PS mejora las propiedades de la perovskita y permite la formación de discos mecánicamente robustos. Dependiendo del contenido de perovskita, se obtienen discos luminiscentes semitransparentes u opacos. Utilizando una composición de disco con un 33% en peso de perovskita se obtuvo un disco opaco con un PLQY de alrededor del 53% y un FWHM de unos 23 nm para los discos que contenían PS y un PLQY de alrededor del 48% y un FWHM de unos 28 nm para el disco que contenía PMMA. Reduciendo el porcentaje en peso de perovskita al 2% se obtuvieron convertidores de color con un PLQY del 60% y un FWHM tan bajo como 21 nm para la PS. Estas propiedades hacen de estos discos unos candidatos excelentes para convertidores de color, ya que tienen una elevada pureza de color y una alta luminiscencia. La transmitancia de estos discos para longitudes de onda superiores a 600 nm fue superior al 72% y al 75% para los discos con PMMA y PS, respectivamente. También se preparó como prueba de concepto un disco con luminiscencia

dual verde y roja, añadiendo un polímero fluorescente a la perovskita durante la síntesis mecanoquímica con el posterior prensado a temperaturas elevadas.

Capítulo 3: Fotoconductores laminados para detección de luz visible basados en perovskita encapsulada con polímeros

3.1. Motivación y objetivo

Las perovskitas de haluros metálicos son semiconductores ampliamente estudiados, debido a sus propiedades optoelectrónicas favorables, su procesamiento sencillo y la posibilidad de modular sus propiedades.[108–110] Como resultado, se ha demostrado la fabricación de fotodetectores de luz visible de alto rendimiento utilizando perovskitas.[101,111–114] Sin embargo, aún quedan varios retos por superar en lo que respecta a la estabilidad y a la realización de fotodetectores de banda estrecha sin filtros ópticos, entre otros. Además, aún faltan métodos de procesado compatibles con la producción a gran escala en entornos industriales.[101,111,113,114] Los procesos de producción sencillos, sin disolventes y de bajo coste son ventajosos para acercar algunos de estos dispositivos al mercado.

En el capítulo anterior, se utiliza la síntesis mecanoquímica para la preparación de compuestos de perovskita-polímero para convertidores de color. Debido a la sencillez de este proceso de fabricación, aquí se explora otra posible aplicación de estos compuestos perovskita-polímero como capa absorbente en fotoconductores. Además, se investiga la posible aplicación en fotoconductores de banda estrecha, ya que el proceso permite fabricar discos gruesos con facilidad.

3.2. Detalles experimentales

La técnica de síntesis para obtener discos de polímero-perovskita sigue los mismos pasos que en el capítulo anterior, pero utilizando una composición de perovskita y un polímero diferente. Se seleccionó la perovskita de haluro inorgánico $CsPbBr_3$ como material absorbente para el fotoconductor debido a su alta estabilidad térmica y buenas propiedades semiconductoras. La perovskita se sintetizó mecanoquímicamente añadiendo una proporción estequiométrica de bromuro de cesio y bromuro de plomo en un recipiente de circonio de 10 mL, seguida de un molido de bolas a una frecuencia de 30 Hz durante 5 minutos con un Rensch MM400.[115] Tras la formación de la perovskita, se añadió PBMA en polvo para obtener la proporción polímero-

perovskita deseada y la mezcla se molió con bolas durante 3 minutos más a la misma frecuencia para obtener un compuesto polímero-perovskita más homogéneo. Se seleccionó PBMA por su estabilidad mecánica y su baja absorción óptica, ya que sólo absorbe en la región UV (< 300 nm), comparable a la de los sustratos de vidrio utilizados en los dispositivos. El polvo de polímero y perovskita se calienta a 100 °C y se prensa durante 1 segundo a 2 toneladas métricas utilizando un anillo espaciador para obtener un disco de 100 µm de grosor, que resulta mecánicamente muy estable.

Una vez fabricados los discos, pueden laminarse sobre el sustrato deseado para producir el fotoconductor. En este caso se utiliza un sustrato de vidrio con electrodos interdigitados de óxido de indio y estaño (ITO) con una separación de 40 µm y una longitud total de 4960 µm. Si es necesario, los discos pueden cortarse con la forma deseada para que se ajusten mejor al sustrato. Gracias a las propiedades adhesivas del PBMA con el sustrato, los discos se pueden laminar fácilmente a una temperatura de 100 °C, lo que da como resultado un fotoconductor lateral.

3.3. Resultados y discusión

Los discos pueden manipularse y laminarse sobre sustratos interdigitados de ITO/vidrio, obteniéndose fotoconductores funcionales. Se evaluaron diferentes concentraciones de perovskita/polímero. El compuesto que contenía un 75 % en peso de perovskita dio lugar a la mayor detectividad específica, con un valor medio de $2 \cdot 10^{11}$ Jones, a un campo aplicado de 2.5 V/µm. La respuesta espectral de los fotoconductores resultó ser bastante constante en todo el rango de absorción de la perovskita. A pesar del grosor de la película compuesta y de la gran distancia entre electrodos (40 µm), se ha medido un tiempo de respuesta de 1.78 ms para los dispositivos con 75 % de perovskita. Además, el grosor de los discos de material compuesto puede aprovecharse para obtener detectores de banda estrecha, iluminando el dispositivo desde el lado del disco en lugar de por el lado del vidrio. El pico del detector de banda estrecha con un espesor de 25 µm se encuentra a 555 nm, con un FWHM muy estrecho de 15 nm y una detectividad de $1 \cdot 10^{9}$ Jones. En general, este proceso muestra una ruta simplificada para producir fotodetectores de perovskita embebidos en polímeros, procesados en aire y en ausencia de disolventes. Debido a la simplicidad de la fabricación y a la flexibilidad del

proceso, puede aplicarse a sistemas de perovskita más complejos y a aplicaciones en condiciones reales de trabajo.

Capítulo 4: Perovskita de haluro encapsulada en polímeros como detectores de ionización

4.1. Motivación y objetivo

Las formas más comunes de preparar detectores de rayos X de perovskita son la disolución y recristalización, el proceso de deposición por pulverización, la fusión y cristalización, la evaporación térmica y los procesos de recubrimiento por rotación.[6,7] Todos estos procesos se han desarrollado notablemente en los últimos años, sin embargo, todavía hay algunos obstáculos importantes que superar. En primer lugar, la estabilidad de los materiales de perovskita sigue siendo relativamente baja. En segundo lugar, para los detectores de rayos X de perovskita, el grosor del material absorbente debe ser de al menos cientos de micrómetros para una absorción suficiente. Los procesos descritos anteriormente presentan dificultades a la hora de fabricar capas gruesas uniformes y, además, el coste de la mayoría de ellos es elevado. Por lo tanto, es necesario desarrollar nuevas técnicas de procesado para la preparación de perovskitas gruesas.[128,139,140] Por último, solo una pequeña parte de la investigación se ha centrado en el desarrollo de detectores de rayos X flexibles y de gran superficie basados en perovskitas. Actualmente, los detectores de rayos X basados en perovskita de mayor rendimiento son pequeños y rígidos, lo que limita sus aplicaciones.

Motivados por las propiedades fotoconductoras en el rango visible de los discos de polímero-perovskita del capítulo anterior, se caracterizan como posible material absorbente para detectores de rayos X. Como se ha mencionado anteriormente, el método de preparación permite producir discos gruesos con facilidad, lo que los hace también interesantes como materiales activos para la detección de radiaciones ionizantes. Con el proceso de fabricación utilizado para estos discos, es posible producir discos gruesos con facilidad, el coste de fabricación es bajo, y la fabricación sobre gran área podría ser viable. Además, los discos son flexibles, lo que permitiría fabricar detectores de rayos X flexibles.

4.2. Detalles experimentales

Para los primeros experimentos, se utilizan los fotoconductores laterales detallados en el capítulo 3. También se fabrican nuevos dispositivos verticales laminando los discos de $CsPbBr_3$-PBMA sobre un sustrato de vidrio con ITO o sobre un sustrato de tereftalato de polietileno con la misma capa de ITO para producir dispositivos flexibles. En caso necesario, los discos pueden cortarse simplemente con tijeras para obtener la forma deseada. Una vez laminados los discos sobre el sustrato, se evaporan térmicamente contactos de cobre de 300 nm de espesor sobre los discos, lo que da lugar a una estructura de dispositivo vertical con 8 contactos de 0,0825 cm^2. Se puede utilizar una cinta de cobre conductora adicional para garantizar el contacto de la parte superior del disco, ya que los discos pueden tener grosores de hasta medio milímetro. Además, los fotoconductores verticales se encapsulan con una capa de óxido de aluminio de 20 nm mediante deposición en capa atómica.

4.3. Resultados y discusión

En resumen, los discos de $CsPbBr_3$ al 50 % en peso en PBMA se consideraron los más prometedores para los detectores de ionización, ya que presentan una respuesta estable y fiable. Para utilizar todo el volumen del material absorbente se fabricaron dispositivos verticales con diferentes espesores de material absorbente. La sensibilidad para diferentes grosores no siguió la ley de Beer Lambert, lo que probablemente se deba al aumento de los estados electrónicos de tipo trampa con el aumento del grosor del material absorbente. Sin embargo, la sensibilidad de los dispositivos verticales aumentó con respecto al diseño lateral, con una sensibilidad máxima de 98±2 µC Gy^{-1} cm^{-2} para la capa absorbente de 470 µm de espesor. El mismo dispositivo tenía un límite de detección muy baja de al menos 46±2 nG/s y una estabilidad excelente bajo irradiación pulsada durante 20 minutos. Por último, se realizaron detectores de rayos X flexibles con un grosor máximo de 100 µm que mostraban casi la misma respuesta que los sustratos rígidos. En conjunto, este sencillo proceso de fabricación en seco permite fabricar detectores de rayos X rígidos y flexibles con propiedades prometedoras.

Capítulo 5: Conclusiones generales

Esta tesis presenta un nuevo y sencillo método de preparación para obtener materiales y dispositivos funcionales a partir de polvos de perovskita. Los resultados recogidos en la tesis demuestran el potencial de este enfoque en aplicaciones como la conversión y la detección de fotones.

En el capítulo 2 se describe el desarrollo de un método de procesamiento sin disolventes que permite convertir polvos de perovskita preparados por síntesis mecanoquímica en una capa funcional. Los polímeros termoplásticos se mezclan con los polvos de perovskita y se prensan, en aire ambiente, en discos mediante prensado en caliente. Gracias al uso de polímeros termoplásticos, se puede obtener un disco mecánicamente estable prensando el polvo por encima de la temperatura de transición vítrea del polímero y dentro de la ventana de estabilidad térmica de la perovskita. Con este método se obtienen convertidores de color basados en partículas altamente luminiscentes de MAPbBr3, dispersas en polímeros transparentes como PMMA, PEO y PS. La calidad del color de los convertidores de color basados en PMMA y PS es alta, con un espectro de emisión estrecho que tiene una anchura total a medio máximo de menos de 25 nm. Además, los convertidores de color son estables durante más de dos meses a una temperatura elevada de 85 °C. Como prueba de concepto, se prepara un convertidor multicolor insertando un fluoróforo adicional en los discos. Este capítulo muestra que el método de procesamiento es muy versátil, no requiere disolventes nocivos y puede utilizarse para preparar convertidores de color con buena estabilidad y alta calidad óptica.

El capítulo 3 amplía la investigación sobre los discos de polímero-perovskita, sintetizados por el mismo método que en el capítulo anterior, utilizándolos como material absorbente para fotoconductores visibles. Para obtener un dispositivo funcional, los discos compuestos se adhieren a un electrodo prepatinado mediante laminación en caliente, preservando la naturaleza simple y seca del método de procesado. Para garantizar una conexión eléctrica robusta entre el sustrato y el disco, se mezcló el polímero PBMA con el material de perovskita, ya que es mecánicamente estable y presentabuenas propiedades de adhesión y baja absorción parásita. El PBMA se mezcló con la perovskita CsPbBr3 en diferentes proporciones, que luego se prueban en sus prestaciones fotoconductoras, observando las mejores propiedades para el 75 % en peso de CsPbBr3 en PBMA con una detectividad específica superior a 10^{11} Jones. Dado que el proceso permite preparar discos gruesos, se pueden conseguir detectores de banda estrecha sin

filtro iluminando el dispositivo desde el lado de la perovskita, lo cual da una respuesta espectral de banda estrecha con un FWHM de hasta 15 nm. Este capítulo revela que los compuestos perovskita-polímero pueden laminarse fácilmente sobre sustratos con buen control del espesor de los discos, obteniéndose dispositivos optoelectrónicos funcionales que pueden utilizarse como fotodetectores sensibles.

Por último, en el capítulo 4, los mismos discos de polímero-perovskita se utilizan como detectores de radiación ionizante. Dado que el método de síntesis permite obtener discos muy gruesos, éstos pueden utilizarse como material absorbente de fotones de rayos X. En primer lugar, se utiliza la configuración lateral del capítulo 3 para observar la influencia de diferentes proporciones de polímero de perovskita. Los mejores resultados se obtuvieron con un 50 % en peso de perovskita en el polímero, lo que dio lugar a una respuesta lineal y rápida a los rayos X, con un límite de detección de 3 μG/s. Sin embargo, en la configuración lateral, la mayoría de los portadores de carga se producen lejos del contacto y, por tanto, se pierden debido a la recombinación dentro del grueso del material. Por este motivo, se fabrican estructuras de dispositivos verticales intercalando los discos entre ITO y contactos de cobre. Estos dispositivos pueden utilizar todo el volumen del material absorbente, lo que da como resultado una sensibilidad de 98±2 μC Gy-1 cm-2 para una capa absorbente de 470 μm de grosor con una LoD tan baja como 46±2 nG/s y con una buena estabilidad bajo irradiación. Por último, los dispositivos flexibles se fabrican utilizando un sustrato de PET en lugar de vidrio, con lo que se obtiene la misma sensibilidad que con los detectores de rayos X rígidos. Este capítulo muestra que se pueden realizar detectores de ionización vertical estables tanto rígidos como flexibles utilizando compuestos de perovskita-polímero.

En general, se desarrolla una metodología para transformar estas perovskitas granulares en dispositivos funcionales. El método es versátil y sencillo, no requiere disolventes, permite controlar el espesor y se presenta una buena adehsión a los sustratos. En vista de estas ventajas, este método puede ser fácilmente adoptado por otros investigadores que trabajen en este campo, pero también por la industria, ampliando la aplicación de perovskitas granulares por síntesis mecanoquímica a aplicaciones funcionales.

7. Bibliography

[1] D. J. W. Alexandra Navrotsky, *Perovskite: A Structure of Great Interest to Geophysics and Materials Science*, *Volume 45*, **1989**.

[2] V. M. Goldschmidt, *Naturwissenschaften* **1926**, *14*, 477.

[3] Y. Cheng, Y. Peng, A. K. Y. Jen, H. L. Yip, *Sol. RRL* **2022**, *6*, 2100545.

[4] W. J. Yin, J. H. Yang, J. Kang, Y. Yan, S. H. Wei, *J. Mater. Chem. A* **2015**, *3*, 8926.

[5] W. J. Yin, T. Shi, Y. Yan, *Adv. Mater.* **2014**, *26*, 4653.

[6] Y. Zhou, J. Chen, O. M. Bakr, H. T. Sun, *Chem. Mater.* **2018**, *30*, 6589.

[7] NREL, *Best Research-Cell Efficiency Chart*, **2023**, p. 1.

[8] K. Lin, J. Xing, L. N. Quan, F. P. G. de Arquer, X. Gong, J. Lu, L. Xie, W. Zhao, D. Zhang, C. Yan, W. Li, X. Liu, Y. Lu, J. Kirman, Edward H. Sargent, Q. Xiong, Z. Wei, *Nature* **2018**, *562*, 245.

[9] Q. Chen, N. De Marco, Y. Yang, T. Bin Song, C. C. Chen, H. Zhao, Z. Hong, H. Zhou, Y. Yang, *Nano Today* **2015**, *10*, 355.

[10] H. Kim, J. S. Han, J. Choi, S. Y. Kim, H. W. Jang, *Small Methods* **2018**, *2*, 1700310.

[11] J. Zhou, J. Huang, *Adv. Sci.* **2018**, *5*, 1700256.

[12] L. Protesescu, S. Yakunin, M. I. Bodnarchuk, F. Krieg, R. Caputo, C. H. Hendon, R. X. Yang, A. Walsh, M. V Kovalenko, *Nano Lett* **2015**, *15*, 3692.

[13] C.-H. Lu, G. V Biesold-Mcgee, Y. Liu, Z. Kang, Z. Lin, *Chem. Soc. Rev* **2020**, *49*, 4953.

[14] F. S. Galasso, *Structure, properties and preparation of perovskite-type compounds: international series of monographs in solid state physics.*, Elsevier, **2013**.

[15] L. Protesescu, S. Yakunin, M. I. Bodnarchuk, F. Krieg, R. Caputo, C. H. Hendon, R. X. Yang, A. Walsh, M. V. Kovalenko, *Nano Lett.* **2015**, *15*, 3692.

[16] A. Amat, E. Mosconi, E. Ronca, C. Quarti, P. Umari, M. K. Nazeeruddin, M. Grätzel, F. De Angelis, *Nano Lett.* **2014**, *14*, 3608.

[17] L. Protesescu, S. Yakunin, M. I. Bodnarchuk, F. Krieg, R. Caputo, C. H. Hendon, R. X. Yang, A. Walsh, M. V Kovalenko, *Nano Lett.* **2015**, *15*, 3692.

[18] W.-J. Yin, J.-H. Yang, J. Kang, Y. Yan, S.-H. Wei, *J. Mater. Chem. A* **2015**, *3*, 8926.

[19] F. Brivio, K. T. Butler, A. Walsh, M. Van Schilfgaarde, *Phys. Rev. B - Condens. Matter Mater. Phys.* **2014**, *89*, 155204.

[20] A. Zakutayev, C. M. Caskey, A. N. Fioretti, D. S. Ginley, J. Vidal, V. Stevanovic, E. Tea, S. Lany, *J. Phys. Chem. Lett.* **2014**, *5*, 1117.

[21] G. W. Kim, A. Petrozza, *Adv. Energy Mater.* **2020**, *10*, 2001959.

[22] D. A. Egger, A. Bera, D. Cahen, G. Hodes, T. Kirchartz, L. Kronik, R. Lovrincic, A. M. Rappe, D. R. Reichman, O. Yaffe, *Adv. Mater.* **2018**, *30*, 1800691.

[23] X. Cao, L. Zhi, Y. Jia, Y. Li, K. Zhao, X. Cui, L. Ci, D. Zhuang, J. Wei, *ACS Appl. Mater. Interfaces* **2019**, *11*, 7639.

[24] S. R. Bae, D. Y. Heo, S. Y. Kim, *Mater. Today Adv.* **2022**, *14*, 100232.

[25] C. C. Stoumpos, C. D. Malliakas, M. G. Kanatzidis, *Inorg. Chem* **2013**, *52*, 9019−9038.

[26] F. Palazon, Y. El Ajjouri, H. J. Bolink, *Adv. Energy Mater.* **2020**, *10*, 1902499.

[27] P. Du, L. Wang, J. Li, J. Luo, Y. Ma, J. Tang, T. Zhai, *Adv. Opt. Mater* **2021**, *10*, 2101770.

[28] W. Pan, B. Yang, G. Niu, K. H. Xue, X. Du, L. Yin, M. Zhang, H. Wu, X. S. Miao, J. Tang, *Adv. Mater.* **2019**, *31*, 1904405.

[29] S. Shrestha, R. Fischer, G. J. Matt, P. Feldner, T. Michel, A. Osvet, I. Levchuk, B. Merle, S. Golkar, H. Chen, S. F. Tedde, O. Schmidt, R. Hock, M. Rührig, M. Göken, W. Heiss, G. Anton, C. J. Brabec, *Nat. Photonics 2017 117* **2017**, *11*, 436.

[30] G. Liu, L. Kong, W. Yang, H. kwang Mao, *Mater. Today* **2019**, *27*, 91.

[31] S. Jiang, Y. Fang, R. Li, H. Xiao, J. Crowley, C. Wang, T. J. White, W. A. Goddard, Z. Wang, T. Baikie, J. Fang, *Angew. Chemie - Int. Ed.* **2016**, *55*, 6540.

[32] D. Ghosh, A. Aziz, J. A. Dawson, A. B. Walker, M. S. Islam, *Chem. Mater.* **2019**, *31*, 4063.

[33] J. Akedo, *J. Therm. Spray Technol.* **2008**, *17*, 181.

[34] S. Kim, M. Y. Cho, I. S. Kim, W. J. Kim, S. H. Park, S. Baek, J. M. Oh, S. W. Kim, *Adv. Mater. Interfaces* **2019**, *6*, 1900359.

[35] M. Schubert, D. Hanft, T. Nazarenus, J. Exner, P. Nieke, P. Glosse, N. Leupold, J. Kita, R. Moos, *Funct. Mater. Lett.* **2019**, *12*, 1930005.

[36] T. Soto-Montero, S. Kralj, W. Soltanpoor, J. S. Solomon, J. S. Gómez, K. P. S. Zanoni, A. Paliwal, H. J. Bolink, C. Baeumer, A. P. M. Kentgens, M. Morales-Masis, *Adv. Funct. Mater.* **2023**, 2300588.

[37] H. Wang, Y. Wu, M. Ma, S. Dong, Q. Li, J. Du, H. Zhang, Q. Xu, *ACS Appl. Energy Mater.* **2019**, *2*, 2305.

[38] B. Dou, L. M. Wheeler, J. A. Christians, D. T. Moore, S. P. Harvey, J. J. Berry, F. S. Barnes, S. E. Shaheen, M. F. A. M. Van Hest, *ACS Energy Lett.* **2018**, *3*, 979.

[39] N. Leupold, K. Schötz, S. Cacovich, I. Bauer, M. Schultz, M. Daubinger, L. Kaiser, A. Rebai, J. Rousset, A. Köhler, P. Schulz, R. Moos, F. Panzer, *ACS Appl. Mater. Interfaces* **2019**, *11*, 30259.

[40] D. Prochowicz, P. Yadav, M. Saliba, D. J. Kubicki, M. M. Tavakoli, S. M. Zakeeruddin, J. Lewiński, L. Emsley, M. Grätzel, *Nano Energy* **2018**, *49*, 523.

[41] Y. El Ajjouri, F. Palazon, M. Sessolo, H. J. Bolink, *Chem. Mater.* **2018**, *30*, 7423.

[42] H. S. Bob Cottis, Michael Graham, Robert Lindsay, Stuart Lyon, Tony Richardson, David Scantlebury, *Shreir's Corros.* **2010**, *4*, 2622.

[43] A. K. Srivastava, W. Zhang, J. Schneider, J. E. Halpert, A. L. Rogach, *Adv. Sci.* **2019**, *6*, 1901345.

[44] Samsung, *QLED TV vs. OLED TV*, **2018**.

[45] W. Lu, Y. Fu, *Spectroscopy of Semiconductors Numerical Analysis Bridging Quantum Mechanics and Experiments*, Vol. 215, **2018**.

[46] NDSSI, *Wide color gamut*, **2023**.

[47] F. Deschler, M. Price, S. Pathak, L. E. Klintberg, D.-D. Jarausch, R. Higler, S. Hü, T. Leijtens, S. D. Stranks, H. J. Snaith, M. Atatü, R. T. Phillips, R. H. Friend, *J. Phys.*

Chem. Lett **2014**, *5*, 1421.

[48] L. Protesescu, S. Yakunin, M. I. Bodnarchuk, F. Krieg, R. Caputo, C. H. Hendon, R. X. Yang, A. Walsh, M. V Kovalenko, *Nano Lett* **2015**, *15*, 25.

[49] Z. Song, J. Zhao, Q. Liu, *Inorg. Chem. Front.* **2019**, *6*, 2969.

[50] N. Sakai, B. Wenger, *Dig. Tech. Pap. - SID Int. Symp.* **2021**, *52*, 892.

[51] G. Lozano, *J. Phys. Chem. Lett.* **2018**, *9*, 3987.

[52] K. Ji, M. Anaya, A. Abfalterer, S. D. Stranks, *Adv. Opt. Mater.* **2021**, *9*, 2002128.

[53] Y. H. Kim, S. Kim, S. H. Jo, T. W. Lee, *Small Methods* **2018**, *2*, 1800093.

[54] Helio Display Materials, *Why next generation tvs need perovskites*, **2022**.

[55] T. Guner, M. M. Demir, *Phys. status solidi* **2018**, *215*, 1800120.

[56] H. Lee, J. Park, S. Kim, S. C. Lee, Y. H. Kim, T. W. Lee, *Adv. Mater. Technol.* **2020**, *5*, 2000091.

[57] E. Radicchi, E. Mosconi, F. Elisei, F. Nunzi, F. De Angelis, *ACS Appl. Energy Mater.* **2019**, *2*, 3400.

[58] L. Yuan, R. Patterson, X. Wen, Z. Zhang, G. Conibeer, S. Huang, *J. Colloid Interface Sci.* **2017**, *504*, 586.

[59] A. Pan, B. He, X. Fan, Z. Liu, J. J. Urban, A. P. Alivisatos, L. He, Y. Liu, *ACS Nano* **2016**, *10*, 7943.

[60] J. De Roo, M. Ibáñez, P. Geiregat, G. Nedelcu, W. Walravens, J. Maes, J. C. Martins, I. Van Driessche, M. V. Kovalenko, Z. Hens, *ACS Nano* **2016**, *10*, 2071.

[61] Z. Y. Zhu, Q. Q. Yang, L. F. Gao, L. Zhang, A. Y. Shi, C. L. Sun, Q. Wang, H. L. Zhang, *J. Phys. Chem. Lett.* **2017**, *8*, 1610.

[62] L. Wang, D. Ma, C. Guo, X. Jiang, M. Li, T. Xu, J. Zhu, B. Fan, W. Liu, G. Shao, H. Xu, H. Wang, R. Zhang, H. Lu, *Appl. Surf. Sci.* **2021**, *543*, 148782.

[63] P. Sadhukhan, S. Kundu, A. Roy, A. Ray, P. Maji, H. Dutta, S. K. Pradhan, S. Das, *Cryst. Growth Des* **2018**, *18*, 3428.

[64] Z. Hong, D. Tan, A. John, N. Mathews, F. García, H. Sen Soo, *ISCIENCE* **2019**, *16*,

312.

[65] L. Martínez-Sarti, F. Palazon, M. Sessolo, H. J. Bolink, *Adv. Opt. Mater.* **2020**, *8*, 1901494.

[66] M. A. Van De Haar, M. Tachikirt, A. C. Berends, M. R. Krames, A. Meijerink, F. T. Rabouw, *ACS Photonics* **2021**, *8*, 1784.

[67] K. A. Bush, C. D. Bailie, Y. Chen, A. R. Bowring, W. Wang, W. Ma, T. Leijtens, F. Moghadam, M. D. McGehee, *Adv. Mater.* **2016**, *28*, 3937.

[68] S. Shi, L. Cao, H. Gao, Z. Tian, W. Bi, C. Geng, S. Xu, *Nanoscale* **2021**, *13*, 9381.

[69] X. Li, X. Qu, Z. Wen, B. Xu, K. Wang, X. W. Sun, *Dig. Tech. Pap. - SID Int. Symp.* **2020**, *51*, 1775.

[70] J. Xue, Y. Gu, Q. Shan, Y. Zou, J. Song, L. Xu, Y. Dong, J. Li, H. Zeng, *Angew. Chemie* **2017**, *129*, 5316.

[71] N. Sakai, H. Hopkin, G. De Keyzer, B. Wenger, In *Digest of Technical Papers - SID International Symposium*, **2022**, pp. 307–309.

[72] Z. Nie, E. Kumacheva, *Nat. Mater.* **2008**, *7*, 277.

[73] L. J. Guo, *Adv. Mater.* **2007**, *19*, 495.

[74] M. Kim, S. G. Motti, R. Sorrentino, A. Petrozza, *Energy Environ. Sci* **2018**, *11*, 2609.

[75] L. Song, X. Guo, Y. Hu, Y. Lv, J. Lin, Z. Liu, Y. Fan, X. Liu, *J. Phys. Chem. Lett* **2017**, *8*, 4148−4154.

[76] M. Li, X. Yan, Z. Kang, Y. Huan, Y. Li, R. Zhang, Y. Zhang, *ACS Appl. Mater. Interfaces* **2018**, *10*, 18787.

[77] Y. Wei, X. Deng, Z. Xie, X. Cai, S. Liang, P. Ma, Z. Hou, Z. Cheng, J. Lin, *Adv. Funct. Mater.* **2017**, *27*, 1703535.

[78] W. Li, Z. Zhong, F. Huang, al -, Q. Dai, C. Luo, F. Corsini, G. Griffin, *J. Phys. Energy* **2020**, *2*, 031002.

[79] J. Peng, J. I. Khan, W. Liu, E. Ugur, T. Duong, Y. Wu, H. Shen, K. Wang, H. Dang, E. Aydin, X. Yang, Y. Wan, K. J. Weber, K. R. Catchpole, F. Laquai, S. De Wolf, T. P. White, *Adv. Energy Mater.* **2018**, *8*, 1801208.

[80] F. Palazon, Y. El Ajjouri, P. Sebastia-Luna, S. Lauciello, L. Manna, H. J. Bolink, *J. Mater. Chem. C* **2019**, *7*, 11406.

[81] S. G. Motti, D. Meggiolaro, A. J. Barker, E. Mosconi, C. A. R. Perini, J. M. Ball, M. Gandini, M. Kim, F. De Angelis, A. Petrozza, *Nat. Photonics* **2019**, *13*, 532.

[82] Y. Ling, Y. Tian, X. Wang, J. C. Wang, J. M. Knox, F. Perez-Orive, Y. Du, L. Tan, K. Hanson, B. Ma, H. Gao, *Adv. Mater.* **2016**, *28*, 8983.

[83] P. Qin, T. Wu, Z. Wang, X. Zheng, X. Yu, G. Fang, G. Li, *Sol. RRL* **2019**, *3*, 1900134.

[84] Z. Wang, Z. Luo, C. Zhao, Q. Guo, Y. Wang, F. Wang, X. Bian, A. Alsaedi, T. Hayat, Z. Tan, *J. Phys. Chem. C* **2017**, *121*, 28132.

[85] V. A. Hintermayr, C. Lampe, M. Löw, J. Roemer, W. Vanderlinden, M. Gramlich, A. X. Böhm, C. Sattler, B. Nickel, T. Lohmüller, A. S. Urban, *Nano Lett.* **2019**, *19*, 4928.

[86] Y. Wei, Z. Cheng, J. Lin, *Chem. Soc. Rev.* **2019**, *48*, 310.

[87] Y. Wang, J. He, H. Chen, J. Chen, R. Zhu, P. Ma, A. Towers, Y. Lin, A. J. Gesquiere, S. T. Wu, Y. Dong, *Adv. Mater.* **2016**, *28*, 10710.

[88] A. Alberti, I. Deretzis, G. Mannino, E. Smecca, F. Giannazzo, A. Listorti, S. Colella, S. Masi, A. La Magna, *Adv. Energy Mater.* **2019**, *9*, 1803450.

[89] J. Peng, J. I. Khan, W. Liu, E. Ugur, T. Duong, Y. Wu, H. Shen, K. Wang, H. Dang, E. Aydin, X. Yang, Y. Wan, K. J. Weber, K. R. Catchpole, F. Laquai, S. De Wolf, T. P. White, *Adv. Energy Mater.* **2018**, *8*, 1801208.

[90] Y. Li, M. Dailey, P. J. Lohr, A. D. Printz, *J. Mater. Chem. A* **2021**, *9*, 16281.

[91] M. Li, X. Yan, Z. Kang, Y. Huan, Y. Li, R. Zhang, Y. Zhang, *ACS Appl. Mater. Interfaces* **2018**, *10*, 18787.

[92] J. Chen, X. Huang, Z. Xu, Y. Chi, *ACS Appl. Mater. Interfaces* **2022**, *14*, 33703.

[93] Y. Peng, Q. Sun, J. Liu, H. Cheng, Y. Mou, *J. Alloys Compd.* **2021**, *850*, 156811.

[94] Z. Lin, H. Lin, J. Xu, F. Huang, H. Chen, B. Wang, Y. Wang, *J. Alloys Compd.* **2015**, *649*, 661.

[95] H. W. Choi, K. N. Hui, P. T. Lai, X. H. Wang, Z. L. Li, *Opt. Express* **2009**, *17*, 9873.

[96] ITU, *Parameter values for ultra-high definition television systems for production and international program exchange*, **2015**.

[97] M. Sugawara, S. Y. Choi, D. Wood, *IEEE Signal Process. Mag.* **2014**, *31*, 170.

[98] D. Yang, D. Ma, *Adv. Opt. Mater.* **2019**, *7*, 1800522.

[99] L. Li, S. Ye, J. Qu, F. Zhou, J. Song, G. Shen, *Small* **2021**, *17*, 2005606.

[100] Z. Zhao, C. Xu, L. Niu, X. Zhang, F. Zhang, *Laser Photonics Rev.* **2020**, *14*, 2000262.

[101] L. Li, S. Ye, J. Qu, F. Zhou, J. Song, G. Shen, *Small* **2021**, *17*, 2005606.

[102] C. Xie, C. K. Liu, H. L. Loi, F. Yan, *Adv. Funct. Mater.* **2020**, *30*, 1903907.

[103] Y. Dan, X. Zhao, K. Chen, A. Mesli, *ACS Photonics* **2018**, *5*, 4111.

[104] D. Zhang, C. Liu, K. Li, W. Guo, F. Gao, J. Zhou, X. Zhang, S. Ruan, *Adv. Opt. Mater.* **2018**, *6*, 1701189.

[105] S. O. Kasap, *Photoconductivity : Fundamental Concepts*, Vol. 1, **2022**.

[106] D. Wu, Y. Zhang, C. Liu, Z. Sun, Z. Wang, Z. Lin, M. Qiu, D. Fu, K. Wang, *Adv. Devices Instrum.* **2023**, *4*, 0006.

[107] D. Silvano, *Photodetectors: Devices, Circuits, and Applications*, 2nd ed., **2001**.

[108] C. C. Stoumpos, M. G. Kanatzidis, *Acc. Chem. Res.* **2015**, *48*, 2791.

[109] S. D. Stranks, H. J. Snaith, *Nat. Nanotechnol.* **2015**, *10*, 391.

[110] J. S. Manser, M. I. Saidaminov, J. A. Christians, O. M. Bakr, P. V Kamat, *Acc. Chem. Res.* **2016**, *49*, 330.

[111] F. Wang, X. Zou, M. Xu, H. Wang, H. Wang, H. Guo, J. Guo, P. Wang, M. Peng, Z. Wang, Y. Wang, J. Miao, F. Chen, J. Wang, X. Chen, A. Pan, C. Shan, L. Liao, W. Hu, *Adv. Sci.* **2021**, *8*, 2100569.

[112] Y. Zhang, Y. Ma, Y. Wang, X. Zhang, C. Zuo, L. Shen, L. Ding, *Adv. Mater.* **2021**, *33*, 2006691.

[113] J. Miao, F. Zhang, *J. Mater. Chem. C* **2019**, *7*, 1741.

[114] M. Ahmadi, T. Wu, B. Hu, *Adv. Mater.* **2017**, *29*, 1605242.

[115] F. Palazon, Y. El Ajjouri, P. Sebastia-Luna, S. Lauciello, L. Manna, H. J. Bolink, *J. Mater. Chem. C* **2019**, *7*, 11406.

[116] C. Li, Z. Zang, C. Han, Z. Hu, X. Tang, J. Du, Y. Leng, K. Sun, *Nano Energy* **2017**, *40*, 195.

[117] M. Rodová, J. Brožek, K. Knížek, K. Nitsch, *J. Therm. Anal. Calorim.* **2003**, *71*, 667.

[118] D. Yang, D. Huo, *J. Mater. Chem. C* **2020**, *8*, 6640.

[119] Y. Zhang, J. Du, X. Wu, G. Zhang, Y. Chu, D. Liu, Y. Zhao, Z. Liang, J. Huang, *ACS Appl. Mater. Interfaces* **2015**, *7*, 21634.

[120] C. C. Stoumpos, C. D. Malliakas, J. A. Peters, Z. Liu, M. Sebastian, J. Im, T. C. Chasapis, A. C. Wibowo, D. Y. Chung, A. J. Freeman, B. W. Wessels, M. G. Kanatzidis, *Cryst. Growth Des.* **2013**, *13*, 2722.

[121] R. Dong, Y. Fang, J. Chae, J. Dai, Z. Xiao, Q. Dong, Y. Yuan, A. Centrone, X. C. Zeng, J. Huang, *Adv. Mater.* **2015**, *27*, 1912.

[122] X. Hu, X. Zhang, L. Liang, J. Bao, S. Li, W. Yang, Y. Xie, X. Hu, X. Zhang, L. Liang, J. Bao, S. Li, W. Yang, Y. Xie, *Adv. Funct. Mater.* **2014**, *24*, 7373.

[123] A. A. Khan, Z. Yu, U. Khan, L. Dong, *Nanoscale Res. Lett.* **2018**, *13*, 399.

[124] Y. Li, Z. F. Shi, S. Li, L. Z. Lei, H. F. Ji, D. Wu, T. T. Xu, Y. T. Tian, X. J. Li, *J. Mater. Chem. C* **2017**, *5*, 8355.

[125] X. Zhang, F. Li, R. Bai, Q. Sun, Y. Hao, S. Xi, M. Zhu, S. Jiang, W. Jie, Y. Xu, *J. Mater. Chem. C* **2022**, *10*, 6017.

[126] M. I. Saidaminov, M. A. Haque, M. Savoie, A. L. Abdelhady, N. Cho, I. Dursun, U. Buttner, E. Alarousu, T. Wu, O. M. Bakr, *Adv. Mater.* **2016**, *28*, 8144.

[127] Y. Fang, Q. Dong, Y. Shao, Y. Yuan, J. Huang, *Nat. Photonics* **2015**, *9*, 679.

[128] H. Wu, Y. Ge, G. Niu, J. Tang, *Matter* **2021**, *4*, 144.

[129] E. B. Podgoršak, *Energy Transfer and Energy Absorption in Photon Interactions with Matter*, **2016**.

[130] L. for T. (Italy) Nuclear, *Interaction of γ-rays with matter*, **2023**.

[131] S. K. Mathanker, P. R. Weckler, T. J. Bowser, *Trans. ASABE* **2013**, *56*, 1227.

[132] M. Spahn, *Nucl. Instruments Methods Phys. Res. Sect. A Accel. Spectrometers, Detect. Assoc. Equip.* **2013**, *731*, 57.

[133] M. J. Yaffe, J. A. Rowlands, *Phys. Med. Biol.* **1997**, *42*, 1.

[134] T. Martin, A. Koch, M. Nikl, *MRS Bull.* **2017**, *42*, 451.

[135] C. A. Klein, *J. Appl. Phys.* **1968**, *39*, 2029.

[136] D. S. McGregor, H. Hermon, *Nucl. Instruments Methods Phys. Res. Sect. A Accel. Spectrometers, Detect. Assoc. Equip.* **1997**, *395*, 101.

[137] M. Thompson, S. L. R. Ellison, R. Wood, *Pure Appl. Chem.* **2002**, *74*, 835.

[138] L. Basiricò, A. Ciavatti, B. Fraboni, *Adv. Mater. Technol.* **2021**, *6*, 2000475.

[139] Y. Wu, J. Feng, Z. Yang, Y. Liu, S. Liu, *Adv. Sci.* **2023**, *10*, 2205536.

[140] Z. Li, F. Zhou, H. H. Yao, Z. Ci, Z. Yang, Z. Jin, *Mater. Today* **2021**, *48*, 155.

[141] A. Datta, Z. Zhong, S. Motakef, *Sci. Rep.* **2020**, *10*, 20097.

[142] N. Leupold, F. Panzer, N. Leupold, F. Panzer, *Adv. Funct. Mater.* **2021**, *31*, 2007350.

Appendix A

Gain mechanism photoconductors

Considering a photoconductor in a rectangular shape contacted with electrodes at both opposite sides as depicted in **Figure A1**. The conductivity in dark conditions can be expressed in the following way:

$$\sigma = q\mu_e n + q\mu_h p \qquad \text{Equation A.1.}$$

where q is the elemental charge, $\mu_{e,h}$ the electron, hole mobility, and n and p are the carrier concentrations for respectively electrons and holes.

When a field is applied at the electrodes the dark current density can be described by:

$$J_{dark} = \sigma E \qquad \text{Equation A.2.}$$

where J is the current density, and E is the electric field.

Now if the absorber material is illuminated with an incident photon flux (φ) with photons greater than the bandgap energy, excess electrons, and holes are generated which can be simply written as:

$$n = n_0 + \Delta n, \qquad p = p_0 + \Delta p \qquad \text{Equation A.3.}$$

where n_0, p_0 are the initial carrier concentrations and Δn and Δp are the excess carrier concentrations produced by illumination of the semiconductor. Since electron-hole pairs are formed by illumination, the excess carriers are equal to each other so $\Delta n = \Delta p$ and the photocurrent can be expressed as:

$$J_{photo} = \Delta\sigma E = (q\mu_e \Delta n + q\mu_h \Delta p)E = (\mu_e + \mu_h)\Delta n q E \qquad \text{Equation A.4.}$$

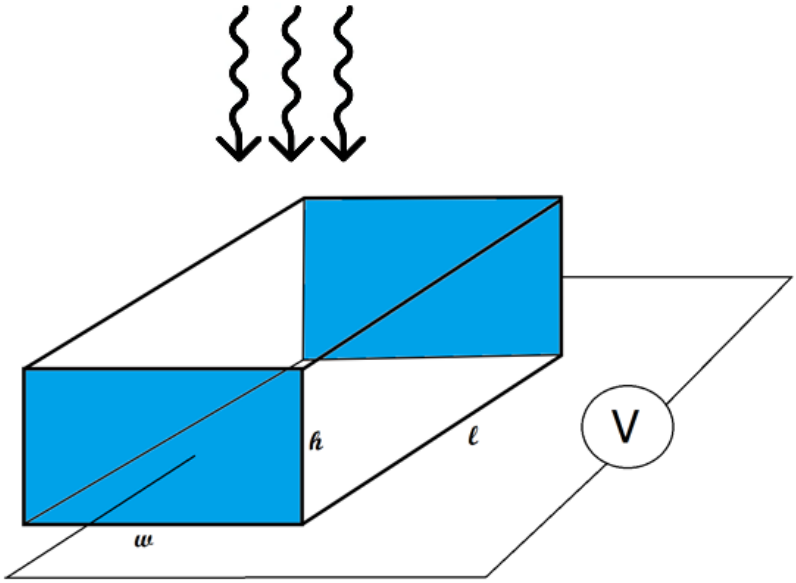

Figure A1. Schematic of a photoconductor, where the blue sides represent the contacts connected to an applied bias, the rectangular represents the absorber material, and the arrows the flux of photons.

The rate of generation of excess carriers per unit volume can be described by **equation A.5**.

$$G_g = \frac{\eta\varphi}{whl} \qquad \text{Equation A.5.}$$

where η is the quantum efficiency which is the ratio of the number of excited electron–hole pairs extracted by the photoconductor to the number of incident photons, φ the incident photon flux, and w, h, l are the dimensions of the absorber material.

Besides the generation rate, the rate of recombination of carriers can be expressed as:

$$G_r = \frac{\Delta n}{\tau} \qquad \text{Equation A.6.}$$

where τ is the excess carrier recombination lifetime, which is the average time at which an electron is recombining somewhere in the lattice, and Δn the excess carrier concentration.

Considering a steady state, then the generation rate and the recombination rate are equal to each other, so:

$$\Delta n = \frac{\eta\varphi\tau}{whl} \qquad \text{Equation A.7.}$$

And therefore,

$$J_{photo} = (\mu_e + \mu_h)\frac{\eta\varphi\tau}{whl}qE$$ Equation A.8.

$$i_{photo} = whJ_{photo} = (\mu_e + \mu_h)\frac{\eta\varphi\tau}{l}qE$$ Equation A.9.

Since the mobility of a carrier multiplied by the electric field results in the carrier velocity:

$$i_{photo} = whJ_{photo} = (\mu_e + \mu_h)\frac{\eta\varphi\tau}{l}qE$$ Equation A.10.

$$v_e = \mu_e E \; and \; v_h = \mu_h E$$ Equation A.11.

And the distance between contacts (l) is formulated, the transit time of the carrier can be given by:

$$t_e = \frac{l}{v_e} and \; t_h = \frac{l}{v_h}$$ Equation A.12.

Therefore, the photocurrent can be rewritten as:

$$i_{photo} = \eta\varphi\tau q \left(\frac{1}{t_e} + \frac{1}{t_h}\right)$$ Equation A.13.

simplified as,

$$i_{photo} = \eta\varphi\tau q \left(\frac{1}{t}\right)$$ Equation A.14.

Now since the photon flux can be described by the incident power (P_0) divided by the photon energy so:

$$\varphi = \frac{P_0}{h\frac{c}{\lambda}}$$ Equation A.15.

where λ is the wavelength, h is the Planck constant, and c is the speed of light therefore,

$$i_{photo} = \frac{\eta q\lambda}{hc}\left(\frac{\tau}{t}\right)P_0$$ Equation A.16.

The response of a device is defined as the induced photocurrent per incident unit of optical power. Assuming that the dark current is very small the response of a device can be written as:

$$R = \frac{i_{photo}}{P_0} = \frac{\eta q\lambda}{hc}\left(\frac{\tau}{t}\right)$$ Equation A.17.

In this relationship, the gain factor is visualized which is described as:

$$G = \left(\frac{\tau}{t}\right)\eta = \left(\frac{\tau}{t_e + t_h}\right)\eta$$ Equation A.18.

Assuming that the mobility of one of the charge carriers is far greater than the mobility of the other charge carrier, for example, if $\mu_e \gg \mu_h$, therefore, $t_e \ll t_h$ the gain can be expressed as:

$$G = \eta \left(\frac{\tau}{t_e}\right) \qquad \text{Equation A.19.}$$

Now a gain mechanism can take place, if $\tau \gg t_e$. So in the case that the recombination time is far greater than (in this case) the transit time of the electrons, electrons can circulate many times before recombination with a much slower moving hole takes place and therefore an EQE higher than 100% can be achieved.

List of constants and abbreviations

Constants

Symbol	*Meaning*	*Value [units]*
c	Speed of light	299792458 [m/s]
h	Planck constant	$6.626\ 070\ 15 \times 10^{-34}$ [J·Hz^{-1}]
$\hbar$	Reduced Planck constant	$1.054571596 \times 10^{-34}$ [J·Hz^{-1}]
m_e	Electron mass	9.109×10^{-31} [kg]
q	Elementary electron charge	$1.602176634 \times 10^{-19}$ [C]

Abbreviations

μ	Atomic mass
μ/ρ	Mass attenuation coefficient
μ_e	Electron mobility
μ_h	Hole mobility
ρ	Density material
σ_{tot}	Total cross-section
τ	Excess carrier recombination time
3D	Three-dimensional
A	Active area
AlOx	Aluminum oxide
A_m	Relative atomic mass
AmCl	Amantadine hydrochloride
Br	Bromine
BX_6	Octahedral
$CaTiO_3$	Calcium titanium oxide
CIE	International Commission on Illumination
Cl	Chlorine
COD ID	Crystallography Open Database identity
Cs	Cesium
Cu	Copper

D^*	Specific detectivity
DR	Dose rate
E	Energy
E_G	Bandgap energy
EQE	External quantum efficiency
$E_{X\text{-}ray}$	X-ray energy
FA	Formadinium
FWHM	Full width at half maximum
G	Gain
Ge	Germanium
I	Iodine
I	Attenuated beam intensity
I_0	Incident beam intensity
ICSD	Inorganic Crystal Structure Database
I_{dark}	Dark current
ITO	Indium tin-doped oxide
IV	Current-voltage
J	Current density
k	Momentum
LED	Light-emitting diode
m*	Effective mass of charge carriers
MA	Methylammonium
N_2	Nitrogen
Pb	Lead
PBMA	Poly(butyl) methacrylate
PEO	Polyethylene oxide
PET	Polyethylene terephthalate
PL	Photoluminescence
PLQY	Photoluminescence quantum yield
PS	Polystyrene
PV	Photovoltaic
Q	Generated carriers
QLED	Quantum Dot Light Emitting Diode

R	Responsivity
r_A, r_B, r_X	Ionic radii
SEM	Scanning electron microscope
Sn	Tin
SNR	Signal-to-noise ratio
t	Goldschmidt tolerance factor
t_e	Transit time electron
t_h	Transit time hole
TV	Television
UV	Ultraviolet
$W_{\pm}$	Ionization energy
wt.%	Weight percentage
x	Absorber thickness
XRD	X-ray diffraction

Publications

B.A.H. Huisman, F. Palazon, H.J. Bolink, *Zero-dimensional hybrid organic-inorganic lead halides and their post-synthesis reversible transformation into three-dimensional perovskites.* Inorganic Chemistry, **2021**, 60 (7), 5212-5216.

P. Sebastia-Luna, U. Pokharel, **B.A.H. Huisman**, L.J.A. Koster, F. Palazon, H.J Bolink, *Vacuum-Deposited Cesium Tin Iodide Thin Films with Tunable Thermoelectric Properties.* ACS Applied Energy Materials, **2022**, 5 (8), 10216-10223.

O. Stroyuk, O. Raievska, P. Sebastia-Luna, **B.A.H. Huisman**, C. Kupfer, A. Barabash, J. Hauch, H.J Bolink, C.J. Brabec, *Highly Luminescent Transparent* $Cs_2Ag_xNa_{1-x}Bi_yIn_{1-y}Cl_6$ *Perovskite Films Produced by Single-Source Vacuum Deposition.* ACS Materials Letters, **2023**, 5 (2), 596-602.

B.A.H. Huisman, H.J. Bolink, *Polymer-Encapsulated Halide Perovskite Color Converters*. Advanced Optical Materials, **2023**, 2202921.

B.A.H. Huisman, C. Bordoni, A. Ciavatti, M. Sessolo, B. Fraboni, H.J. Bolink, *Laminated Polymer-Encapsulated Halide Perovskite Photoconductors*, Advanced Functional Materials, **2023**, 2308844.

L. León-Alcaide, J. López-Cabrelles, M. Esteve-Rochina, E. Ortí, J. Calbo, **B.A.H. Huisman**, M. Sessolo, J.C. Waerenborgh, B.J.C. Vieira, and G.M. Espallargas, *Implementing Mesoporosity in Zeolitic Imidazolate Frameworks through Clip-Off Chemistry in Heterometallic Iron–Zinc ZIF-8,* Journal of the American Chemical Society, **2023**, 145, 42, 23249–23256.

Acknowledgments

I want to express my utmost gratitude to Henk as my professor, supervisor, and group leader during my PhD journey. I am really happy to have conducted my research in your group and I look back to a very nice period. Your innovative thinking and not being scared to think outside the box are really qualities I admire. I think my thesis topic is a good example of this mindset. Moreover, I appreciate the personal aspect of your approach to me and my fellow group members. I always enjoyed our research discussions where I always ended up with new ideas and being excited to perform new experiments, but I also enjoyed the opportunity to share a casual drink and engage in informal conversations with you. Thank you for making my time as a PhD student enriching and enjoyable. Your guidance has been invaluable, and I have learned a great deal from our experiences together. I also like to extend my gratitude to my other supervisor, Michele. Your advice when working on photodetectors was very helpful to me. Your extensive knowledge and constructive feedback have been amazing, and I like your ability to provide guidance while allowing space for individual direction. I am always amazed at how calm you can stay in every situation and I think this reflects positively on the group dynamics, and I am truly thankful for all the input you gave me that has undoubtedly enhanced my research skills.

While Henk and Michele were my supervisors, I also like to thank several individuals who played crucial roles during my years here. Firstly, a special thanks to Paco, who revealed to me the importance of remaining attentive to nuances in research results that could be relevant to other areas. It was through your influence and approach that we successfully published my first paper. Next, I want to express my appreciation to Jorge. In addition to ensuring the lab's smooth operation, you provided invaluable assistance in the initial implementation of unconventional tools I liked to implement in the evaporation systems and to measure the low electronic signals of my devices. Lastly, I want to acknowledge Maria who, despite my occasional struggles with administrative tasks, always kept friendly and calm and made it somehow work. Your contribution is truly appreciated.

I want to thank all my other group members which, due to the great efforts of the team, are too many to highlight per person. Thanks to you guys I was always happy to go to work. I really appreciate this group where the ambiance is always great and everyone is helpful to each other. While I really appreciate every group member, there are some members that I wanted to

highlight. First, I want to thank Isidora. During our PhDs, we really grew a fantastic friendship that I deeply treasure. You always bring a lot of joy and energy and are not for nothing the party organizer. Secondly, I want to highlight Chris not only for being a stellar physicist but also for being a great companion and friend. There was always a good laugh, from the trip to Salamanca to being stuck in multiple escape rooms. Kassio, a good friend for his honesty and "humor", which I think is one of the important persons for making the group dynamic so great. Javi, we weren´t for long colleagues, but with your great energy and spirit, we became friends quickly. Isabella, as you would say the second-best colleague in the group. Paz, my quartz update companion and besides for a long time my shared author buddy. Abhi, a great smart friendly person with dance moves that words couldn´t describe. Federico my Argentinian friend who always missed me at lunch and we could share our love for Spanish desserts. Lorenzo, the perfect companion for a good chat and always up for activities. The photodetector team Lucia and Serhii. Lidon, who is basically the know-how of our group, but besides the most patient and helpful person I know. Nathan, for sharing the struggles with our flash evaporation system. Sang, a brief mention to keep it short, knowing you'll appreciate it. Inma, who always brings a laugh even when things do not go as desired (and also my administrative wonder). I would like to thank Sofia for the good spirit she always brings and for the check of my Spanish summary. Finally, I would like to thank Professor Senku, for the great times during his stay here. Then of course I would like to mention and thank all the other group members I worked with: Argha, Max, Michelino, Joost, Manu, Lennart, Cristina, Dani T., Dani P., Ana, Laura, Maria Grazia, Azin, Jorge A., Beom-Soo Kim, Vladimir, Vincent.

Verder wil ik mijn Nederlandse vrienden in Valencia, Joost en Rick bedanken. Jullie maakten mijn tijd in Valencia geweldig en we houden 100% contact. In het bijzonder wil ik Joost nog bedanken. We ontmoetten elkaar al in de eerste week toen ik hier in Valencia aankwam en sindsdien hebben we vele avonturen meegemaakt en is er een hechte vriendschap ontstaan die mij erg veel waard is. También me gustaría expresar mi gratitud a mis amigos españoles y en particular a Andrés, que siempre me incluyó en todo, incluso desde el principio cuando no podía hablar ni una palabra de español. Gracias a vosotros me sentí realmente incluido en la comunidad española. Of course, I also want to thank my other friends I met in Valencia, like my old roommate and friend Davide, my favorite Venezuelan Carlos, and of course the gang from Altea Thomas and Ted.

Vaak werd mij gevraagd of ik Nederland mis, maar mijn antwoord daarop is dat ik eigenlijk alleen mijn vrienden en familie in Nederland mis. Door jullie vele bezoeken, contact en

betrokkenheid werd dit gemis een stuk minder en ik voel mij gezegend met zo'n vriendengroep en familie.

Ik wil mijn waardering uitspreken aan mijn vrienden van de Bracque, met wie ik ontelbare avonturen heb beleefd en van wie ik veel waardevol advies heb ontvangen. Ook wil ik mijn dank uitspreken aan mijn vrienden en voormalige huisgenoten van het HOI voor de mooie tijden. Ik realiseer me maar al te goed dat vriendschappen na een tijd in het buitenland kunnen vervagen, maar jullie hebben me altijd overal bij betrokken, mij opgezocht in Valencia en tijd voor me vrijgemaakt als ik in Nederland was. Dank hiervoor. Graag zou ik ook nog Hugo, Paul, Caspar, Maurice, KC, Joep, Hendrik, Niels en Jeroen willen uitlichten, die naast geweldige vrienden voor mij zijn, altijd hele programma's voor me klaar maakten als ik even in Nederland was en waar altijd het huis voor openstond als het net iets te laat was geworden.

Graag wil ik mijn familie benoemen die erg waardevol voor mij is. Er zijn vele familieleden hier langsgekomen in Valencia en ik weet dat dit niet vanzelfsprekend is. Ook in Nederland heb ik altijd geprobeerd jullie zo veel mogelijk op te zoeken, en ik voel mij gezegend met zo'n familie. Verder wil ik Oma Huisman nog graag benoemen, die naast de vreugde en liefde die ze me geeft, er ook voor zorgt dat ik altijd met beide benen op de grond sta. Ook wil ik opa en oma Bolster en opa Huisman graag benoemen. Jullie waren allemaal voorbeelden voor mij en hebben mij veel liefde gegeven maar ook zeker bijgedragen aan de persoon die ik nu ben.

Koen en Luc, ik ben zo gelukkig met jullie als mijn broers. Het is fijn om zo'n band te hebben waarbij we altijd op elkaar kunnen rekenen. Jullie zijn er altijd om mij te ondersteunen, en ik ben trots dat jullie mijn broers zijn. Daniek, ondertussen voel je als een zus voor me, en ik ben altijd blij met je energie en betrokkenheid. Pap en mam, ik kon geen betere ouders wensen. Jullie hebben mij opgevoed tot de persoon die ik ben, en ik weet hoeveel jullie voor ons drie hebben gedaan. Ik denk nog vaak terug aan mooie momenten waarop pap bijvoorbeeld mijn voetbalcoach was of dat mam ons meenam naar werk voor de vele leuke activiteiten. Ook nu blijven jullie altijd super betrokken en ondersteunen jullie mij altijd de volle honderd procent. Hierdoor is een groot deel van deze thesis eigenlijk te danken aan jullie, en draag ik deze thesis dan ook graag op aan jullie. Ik hou van jullie.